

Mapping Saltwater Intrusion using Transient ElectroMagnetic Data in
Maopa, Central Province, Papua New Guinea

Ronald Togo VERA VE

A thesis submitted to Victoria University of Wellington in partial
fulfillment of requirements for the Degree of Master of Science in
Geophysics

School of Geography, Environment and Earth Sciences

JULY 2, 2019
VICTORIA UNIVERSITY OF WELLINGTON

Dedication

To my late father, Taera VERAVERA

“Pono vai gaua” (persevere)

These were your dying words that motivated me when times were tough.

Acknowledgement

The successful completion of this thesis would not have been possible without the remarkable people I would like to mention here.

Foremost, I wish to extend my endless gratitude to my supervisor Dr Malcolm Ingham from the School of Chemical and Physical Sciences at Victoria University of Wellington (VUW). Your valuable support, patience, useful critique sessions, and guidance are reflected in the successful completion of this thesis.

A very special thanks to Assoc. Prof. Gillian Turner also from the School of Chemical and Physical Sciences, for your help and guidance from the beginning of my journey at VUW. Particularly, your words of encouragement and comfort during the lowest point of my life - the passing of my late father - gave me hope and strength to return and finish my studies.

I am also grateful to my employer the Mineral Resources Authority for not only allowing me to take up studies with consistent support but also for partially funding this study. Special mention to the Geological Survey Division team, Nathan Mosusu, Maxine Lahan, Philip Irarua, and Mike Ken for your undivided help and support. Thanks also to the Acting Executive Manager of Cooperate Services Division, Edward Lasisi.

I would like to also extend my thanks to all the clans and tribes of Keakalo Bay, particularly the people of the mother village Maopa, for your support and permission to access your land.

Special thanks to the field team from Maopa for their commitment, patience and positive energy demonstrated during field expeditions, which quite often led into otherwise unexplored areas that were difficult to access (Leka Puka, Pikana Mega, Verave Verave, Andrew Henao, Rigolo Lua, John Kapi Rau, Mega Ishmael, Mackay Varage, Verave Rolu, Kapi Kana, Ulea Vagi, Vagi Vanua, Vai Koula, Ian Titi, and Leka Lagani).

Finally, and most importantly I must express my very profound gratitude to my parents and my wife Tule for providing me with unfailing support and continuous encouragement throughout my years of study and through the process of researching, field work and writing this thesis. This accomplishment would not have been possible without them. Thank you.

Abstract

Saltwater intrusion studies in coastal Papua New Guinea (PNG) are a rarity despite recognized vulnerabilities to salination of coastal groundwater resources. For many seaside communities such as Maopa the threat of salination is exacerbated by high extraction rates by a growing population and the likelihood of the effects of climate change. Saltwater intrusion can be addressed using various methods, including direct water sampling from wells and electrical resistivity measurements. This study advances knowledge of a previous assessment of saltwater intrusion and groundwater in this region that used DC Schlumberger resistivity soundings, through an extensive and cost-effective Transient ElectroMagnetic (TEM) survey. The study aims to map the lateral and vertical extent of salination and the characterization of groundwater in the landward direction over seven lines of TEM soundings along Keakalo Bay. The TEM method proved successful in identifying four main geoelectric layers. The top layer has a highly variable resistivity (range of 5 to 355 Ωm) inferred as the vadose zone. Beneath this layer is a layer of intermediate resistivity ($100 \Omega\text{m} > \rho \geq 20 \Omega\text{m}$) characterizing a perched freshwater aquifer with a thickness range of 3.2 to 15 m. An intermediate layer of low resistivity ($20 \Omega\text{m} > \rho \geq 3 \Omega\text{m}$) was detected at the boundary separating the freshwater aquifer from the inferred saltwater intrusion. This layer is typically thicker than the freshwater aquifer and is referred to as the mixing zone. The deepest layer constituting the salination zone has a very low resistivity ($3 \Omega\text{m} > \rho \geq 0.4 \Omega\text{m}$), occurring at depths of up to 42 m. The depth to the salination zone varied from deep in the middle of the survey area to shallow in the fringes of the survey. This pattern is reflective of surface seawater infiltration marked by mangrove forest in the interior and subsurface infiltration from the coast. Similar depth trends but at shallower depths were also observed for the mixing zone, and the freshwater region. In some cases the mixing area overwhelms the freshwater regions. Layering confirmed groundwater resource and salination patterns as those of basic models reflective of small island hydrology, except that salination and the freshwater boundary were less distinctive due to the relatively high thickness of the dispersion zone. The use of different sounding parameters in line 7 provided useful information about the nature of the deep basement unit and thickness of the overlying unconsolidated quaternary sediment.

Table of contents

Dedication	ii
Acknowledgement	iii
Abstract.....	iv
Chapter 1 Introduction.....	1
1.1 The area of research	1
1.2 Previous study	2
1.3 Research problem	3
1.4 Research questions	3
1.5 Research method in brief.....	4
1.6 Structure of the thesis.....	4
Chapter 2 Theoretical background.....	5
2.1 Theory of TEM.....	6
2.2 Maxwell's equations	6
2.3 Simplification and conversion of Maxwell's equations.....	7
2.4 Application of the Schelkunoff potentials.....	7
2.5 Establishing the step response using the transient Magnetic dipole	9
2.6 Analytical solution for the transient response.....	10
Chapter 3 Description of the study area	13
3.1 Regional.....	13
3.2 Local settings.....	14
3.3 Physiography.....	15
3.4 Climate	16
3.4.1 Rainfall	16
3.4.2 Evaporation.....	17
3.5 Geology	18
3.6 Hydrology	20
3.7 Previous study	20
Chapter 4 TEM survey and data processing.....	24
4.1 TEM survey area.....	24
4.2 Sounding locations and lines.....	26
4.3 Field setup and measurements.....	27

4.4 Data processing and inversion	29
Chapter 5 Results, discussion and interpretation	34
5.1 Resistivity cross-sections.....	34
5.1.1 Profile 1.....	35
5.1.2 Profile 2.....	36
5.1.3 Profile 3.....	37
5.1.4 Profile 4.....	38
5.1.5 Profile 5.....	39
5.1.6 Profile 6.....	41
5.1.7 Profile 7.....	42
5.2 Spatial interpretive iso-maps.....	44
5.2.1 Freshwater layer	45
5.2.2 Mixing zone.....	46
5.2.3 Saline zone	48
Chapter 6 Summary	50
References	52
Appendix 1	55
6.1 Line 1.....	55
6.2 Line 2.....	59
6.3 Line 3.....	64
6.4 Line 4.....	68
6.5 Line 5.....	72
6.6 Line 6.....	76
6.7 Line 7.....	83
6.8 Random soundings.....	88
Appendix 2	89
6.9 Master file.....	89

List of Tables

Table 4-1 Sounding coordinates referenced to WGS84 UTM zone 55S.	26
Table 4-2 Survey Instrument configuration.	29

List of figures

Figure 1.1	Location of VES soundings from Verave (2018). Map courtesy of Google Earth.....	2
Figure 2.1	Layout of Transmitter loop and receiver coil and the subsequent induction both the Magnetic field and the circular currents (Modified from Bucker et al. 2017).....	5
Figure 3.1	Map of South Eastern mainland PNG outlining the Central province and various significant locations including the survey area (insert map courtesy of Wikipedia).	13
Figure 3.2	Simple physiographic map of the study area showing four main physiographic regions. Red dashed lines denote the two Highlands region whereas, the red dotted lines denote the boundary separating the Inland Lowland Plains from the Coastal Lowland Plains.....	14
Figure 3.3	Annual rainfall classification of PNG (After MacAlpine et al. 1983).....	17
Figure 3.4	Annual rainfall of survey area (https://climateknowledgeportal.worldbank.org/watershed/378/climate-data-historical).	17
Figure 3.6	Simplified map of the geology of the survey area (After Pieters, 1978).....	19
Figure 3.8	Zone A and Zone B cross-section showing inferred interpretations of layers and their modelled resistivity. For each section the layer thickness (in m) is shown on the left and the layer resistivity (in Ωm) is shown on the right. The brown, green, and blue lines denote the surface elevation, freshwater table, and top of saline zone respectively. The inference of shallow layering are based on surface observation and inspections of diggings from hand dug wells.	22
Figure 4.1	Map of TEM survey showing 88 TEM measurements and the locations of previous VES measurements.	25
Figure 4.2	Examples of environmental conditions in the field set up. a) Laying out Transmitter loop and the central loop coil based on the central loop configuration. Yellow arrows denote the four corners of the transmitter loop while the central red circle shows the setting up of the High Frequency (HF) receiver coil; b) display of the main components of the TEM survey labelled as (1) PROTEM CM console; (2) 35 × 35 m transmitter current loop spool; (3) HF receiver coil; (4) Low frequency (LF) receiver coil; c) setting up survey parameters on PROTEM CM console with red arrow indicating HF receiver coil in background, which usually starts recording after the parameters have been set; d) showing measurements taken for the LF offset receiver coil which follow measurements at the central loop HF coil. The red arrow indicates the LF receiver coil connected to the PROTEM CM console; e) & f) examples of conditions encountered in the interior parts of the survey area, e) being a snapshot of mangrove swamp crossing during measurements at line 7 while f) shows navigating through thick grassland.	27
Figure 4.3	Survey loop configurations.....	28

Figure 4.4	Maopa TEM data flow diagram with numbers indicating the four main stages of the process flow.....	29
Figure 4.5	Graphical display of processing of a raw GX7 file in PROTEMW. On the y axis is the recorded voltage in nano Volts (nV) while the x axis shows time in milliseconds (ms) both scaled logarithmically. The panel to the right displays sounding information such as station number and frequency type. (a) display of the date stamp raw GX7 file (OCT2518A.GX7) showing the records of soundings taken on a particular day; (b) example of separation of sounding data per location showing improper amplification HF signal component with respect to the LF signal; (c) example of attempted correction of HF signals through manual gain normalization and averaging of the data from (b); (d) example of relatively clean and aligned signal components with signs of early time signal saturation presumable due to improper gain selection. (e) Corrected and averaged final data curve of (d) ready for extraction.....	30
Figure 4.6	Examples of Inverted data. On the left is a graph of apparent resistivity (Ωm) vs time (ms) with red and blue squares indicating measured high frequency and low-frequency data, respectively. The red and brown Lines on the graph denote calculated and Occam's estimated smooth models, respectively. At the centre is the depth model showing depth vs calculated resistivity (red line) and the estimated smooth model (brown line).	33
Figure 5.1	TEM survey map showing locations of lines/profiles with their respective TEM soundings.....	34
Figure 5.2	Resistivity Cross-Section Profile 1 shows the Interpolation of 1D resistivity models of 11 TDEM soundings from Line 1 located on the western flank of the study area (Figure 5.1). Red lines denote the inferred top of the modelled layers.	35
Figure 5.3	Resistivity Cross-section Profile 2 shows Interpolation of 12 Soundings from Line 2. ...	36
Figure 5.4	Resistivity Cross-section Profile 3, shows Interpolation of 9 Soundings from line 3.	37
Figure 5.5	Resistivity Cross-section Profile 4 shows Interpolation of 11 Soundings from line 4.	38
Figure 5.6	Resistivity Cross-section Profile 5 shows Interpolation of 10 Soundings of line 5.....	39
Figure 5.7	Resistivity Cross-section Profile 6 shows interpolation of 11 soundings along line 6 stretching more than 2 km. The gap between SND065 and SND066 is an area occupied by one of the largest water bodies in the area.....	41
Figure 5.8	Resistivity Cross-section Profile 7 is made up of interpolation of 11 soundings from line 7 making up the longest line of the survey stretching 3.4 km inland. This line runs right through the mangrove swamp indicated by the void in sounding stations and terminates in the Coastal Highlands region.	42
Figure 5.9	Resistivity inversion of TDEM data from sounding SND085 and SND086, showing the apparent resistivity curve inverted into actual resistivity by depth. On the left is a graph of apparent resistivity (Ωm) vs time (ms) with red and blue squares indicating measured high frequency and low-frequency data, respectively. The red and brown lines on the	

graph denote calculated and Occam's estimated smooth models, respectively. At the centre is the depth model showing depth vs calculated resistivity (red line) and the estimated smooth model (brown line). The right box shows the modelled geoelectric layers and their corresponding resistivity, thickness, and depth. 44

Figure 5.10 Freshwater layer interpretive iso-maps (a) depth to aquifer; (b) aquifer resistivity; and (c) aquifer thickness..... 45

Figure 5.11 Mixing Zone interpretive iso-maps (a) depth to mixing zone; (b) mixing zone resistivity; (c) mixing zone thickness. 47

Figure 5.12 Salination interpretive iso-maps (a) depth to salination; (b) salination resistivity. 48

Chapter 1 Introduction

1.1 The area of research

Coastal groundwater resources potentially support a little over a third of the world's population currently living within 100 km of the coast (Post et al., 2018) where population densities are generally high and increasing. In Papua New Guinea (PNG), although little can be said about facts in this regard, a number of coastal communities exist and depend heavily on coastal groundwater resources for freshwater supply. Maopa village epitomises such communities. Because of its close proximity to the coast and its rising population Maopa's fresh water supplies are increasingly becoming threatened by saltwater intrusion invoked primarily by high extraction rates and, due to its near sea level elevation, potentially by climate change effects such as sea level rise. Historically, the provision of fresh water from communal wells and rain water storage in Maopa was sufficient, but augmented demand by a growing population and unaffordability of rainwater tanks meant that the communal wells became overused, thus further exacerbating salinization of its groundwater resource. This is a problem widely faced by coastal communities globally and still remains a poorly understood phenomenon – its nature and dynamics and its responses to changes caused by natural and anthropogenic effects – although coastal groundwater resources are globally considered an important sources of fresh water (Ingham et al., 2006; Jakeman et al., 2016).

Mapping saltwater intrusion can be achieved using various methods such as direct measurements from wells (Melloul & Goldenberg, 1997; Murgulet & Tick, 2007) and geophysical techniques in the form of direct current (DC) and electromagnetic (EM) (Goldman et al., 1991; Nielsen et al., 2006) resistivity measurements. However, the method of choice is usually determined by the applicability of these methods and the specific objectives. Despite the ability of direct measurement of salination from wells, its discreteness may pose issues regarding the accuracy of locating and assessing the degree of salination in a typically complex coastal hydrology. The very conductive nature of seawater makes it an ideal target for the geophysical resistivity methods, which are used to differentiate contrasting subsurface resistivity that can pertain to varying conductive fluids (e.g. saltwater). The subtle change in the electrical conductivity between freshwater and saltwater therefore makes resistivity methods ideal for saltwater intrusion studies. While DC resistivity methods, particularly the Schlumberger technique, are widely used for groundwater and saltwater intrusion studies, the inability to consistently define varying resistivity progressively in the landward direction, coupled with applicability and accessibility issues greatly reduces its reliability. These are typical of the method and were among issues encountered by Verave (2018) from which the current study

advances with the application of Time Domain or Transient ElectroMagnetic resistivity method (TDEM or TEM). TEM is a relatively new method but fast becoming popular (El-Kaliouby & Abdalla, 2015; Shaaban et al., 2016; Ezersky & Frumkim, 2017; Leite et al., 2018) not only because of its ability to overcome issues faced by the DC method but primary because of sampling accuracy and its high spatial density.

1.2 Previous study

The need to access the salination of Moapa's groundwater resource has been exacerbated by the growing demand for freshwater after contamination of the hand dug communal wells. Verave (2018) in an unpublished study used 16 DC Schlumberger Vertical Electrical Soundings (VES) aimed at delineating the extent of the saline zone and identifying areas of sufficient fresh water in Maopa. The study covered a small area of about 0.24 km² with soundings mostly situated within the most developed regions of Maopa village (Figure 1.1). The 1D inversion of VES soundings demonstrated the presence of the saline zone in all soundings at increasing depth (up to 30 m) in the landward direction.



Figure 1.1 Location of VES soundings from Verave (2018). Map courtesy of Google Earth.

Models also identified a freshwater layer as overlying the saline zone with a thickness of about 20 m mainly further from the coast. While the results suggest that groundwater resources of Maopa are vulnerable to saltwater intrusion, the inadequate coverage and poor modelling of the geoelectric layers could not explain adequately the characteristics of groundwater and salination.

1.3 Research problem

In the current study three main limitations of the previous study are addressed: first is the broad detection of the saltwater interface across all soundings, which will identify if groundwater could be either connected to the main land or is a freshwater lens. Because of the fact that a small area was covered with only a maximum distance of up to 800 m from the coast and located in the mainland, there are two possibilities. These uncertainties are aggravated by the inability to find the inland limit of the saline zone. The second limitation is the lack of inference as to whether or not the groundwater resources are linked to the inland highlands regions, something which could not be verified. Thirdly, the use of the DC Schlumberger method proved limiting because of the challenging environment and thus measurements only clustered around the established parts of Maopa village.

More specifically the following research questions need to be addressed:

1. Where is the extreme limit of saltwater intrusion (if any)?
2. Is the groundwater resource linked to the inland highland region?
3. Is it possible to characterise groundwater and saltwater intrusion with a capable resistivity method?

Resolving these limitations would help conceptualise the conductivity model of the groundwater resources and the influence of the saltwater, allowing the areas of sufficient freshwater supply and those areas vulnerable to salination to be identified.

1.4 Research questions

The long term goal is to provide geoscientific information about the groundwater resources of Maopa to better inform future groundwater development. The objective of the current study is to advance the previous study using the Transient electromagnetic (TEM) resistivity method to conceptualize the conductivity model of Moapa's groundwater resource in order to identify regions of ample volumetric capacity and areas of vulnerability to saltwater intrusion. Particularly the study has the following sub-objectives:

1. To refine known geo-electric layers determined by the previous study
2. To improve resistivity profiles
3. To extend the area of coverage to give increased information

1.5 Research method in brief

The approach used in this study involves an extensive coverage of central loop TEM soundings along a series of lines that reach the bounding interior mangrove swamps. The method is non-invasive and easy to set up allowing maximum coverage of the areas otherwise considered physiographically demanding. The TEM, in contrast to the lengthy spread lines of DC Schlumberger method, uses a square current loop to initiate induction in both loop and the subsurface in a transient fashion. The resulting secondary responses of induction from the subsurface is recorded as a voltage signal as a function of time by an inductor coil placed strategically on the surface. It is the inversion of this data that allows imaging and analysis of the subsurface resistivity along designated lines.

1.6 Structure of the thesis

The thesis covers six chapters. A brief theoretical background of the theory of TEM is given in Chapter 2. Chapter 3 provides a description of the study area. In Chapter 4 the TEM survey and the processing of TEM data are described. The presentation of results and their Interpretation are in Chapter 5, with a summary in Chapter 6.

Chapter 2 Theoretical background

The earliest use of the TEM method was in mining exploration (deep exploration). Kaufman and Keller (1983) and McNeil (1990) are the most cited authors in that regard, contributing immensely to the TEM method at that time. Since then the application of TEM evolved to be more diverse, expanding from deep exploration to shallow exploration such as for groundwater and environmental applications (Fitterman, 2017). In general advancement in TEM owes credit to the improvement of computer technology and advancement of instrument electronics.

Fitterman and Stewart (1986) and Christiansen et al. (2006) described in detail the basic principles of the TEM field technique, while Fitterman (2017) provides a good summary. A typical TEM sounding involves transmitting current into a square loop. The current flow in the loop induces a static primary magnetic field. When current is abruptly turned off the disappearing primary magnetic field causes induction of circular currents beneath the loop according to Faraday's law. These circular currents over time diffuse outward and downward at a rate determined by the ground conductivity structure through which it passes (Figure 2.1).

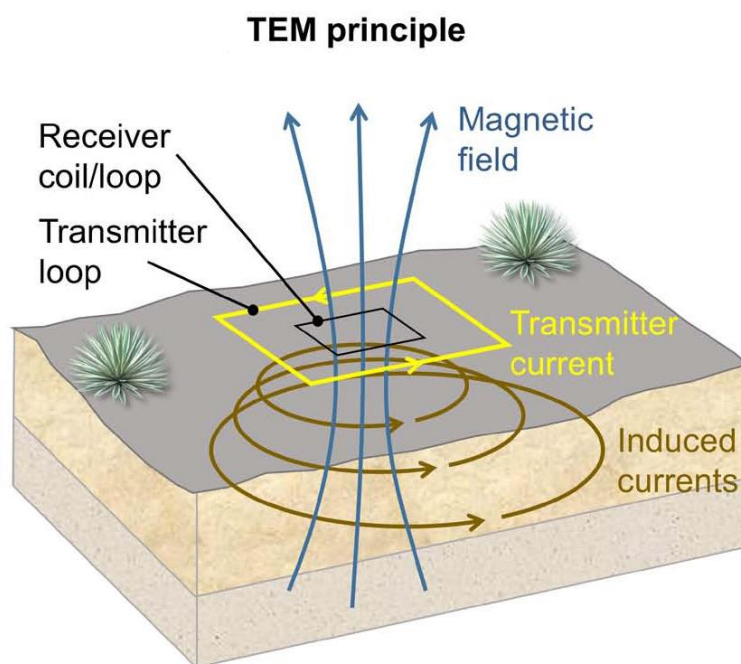


Figure 2.1 Layout of Transmitter loop and receiver coil and the subsequent induction both the Magnetic field and the circular currents (Modified from Bucker et al. 2017).

Low resistivity or conductive regions slow down current attenuation whereas in resistive (low conductivity) regions the propagation of the decaying current is much faster. The circular currents generate a changing secondary magnetic field whose magnitude mimics the decaying circular current system and is recorded by the receiver coil at the centre of the transmitting loop. At the

initial stage of current removal from the transmitter loop, the circular currents are concentrated near the surface of the ground, thus signals recorded by the receiver coil represent conductivity of the near surface layers. Conversely, at later times currents reach deeper layers thus recorded signals are representative of the conductivity of deeper layers. Since this phenomenon is governed by the relationships of ground electrical conductivity, current diffusion, and the secondary magnetic field, measurement of voltage as the function of time at the receiver coil can be used to extract information about the conductivity structure as a function of depth.

2.1 Theory of TEM

The phenomenon of electromagnetism is governed by Maxwell's equations. In the TEM geophysics method the most relevant quantity is the time-varying magnetic field, which induces electric currents in the ground which, in turn, produces a time-varying secondary magnetic field.

This section discusses the most basic essential parts of TEM geophysics and describes the theory behind electromagnetism and the formulation of the transient response expression. Up to the application of Schkelkunoff potentials, the electromagnetic derivations are general but become more specific to TEM geophysics method when source fields are characterized. The development below follows that of Christiansen et al. (2006).

2.2 Maxwell's equations

It is well established that the quantities of E (electric field intensity), B (magnetic induction), D (dielectric displacement), H (magnetic field intensity) and j (electric current density) all describe an electromagnetic field and that their interaction is encapsulated and controlled by Maxwell's equations.

$$\underline{\nabla} \times \underline{E} = -\frac{\partial \underline{B}}{\partial t} \quad (1)$$

$$\underline{\nabla} \times \underline{H} = \underline{j} + \varepsilon \frac{\partial \underline{E}}{\partial t} \quad (2)$$

$$\underline{\nabla} \cdot \underline{B} = 0 \quad (3)$$

$$\underline{\nabla} \cdot \underline{E} = \frac{\rho}{\varepsilon_0} \quad (4)$$

where ρ is the volume charge density.

Equations (1) – (4) are disconnected and are in the first order differential form in the time domain and are subject to boundary conditions.

2.3 Simplification and conversion of Maxwell's equations

Maxwell's equations are in time domain form and deal with multiple variables. A simplification of this form is achieved through Fourier transformation of equations (1) and (2) and applying the frequency constitutive relationship given by:

$$D = [\varepsilon'(\omega) - i\varepsilon''(\omega)]E = \varepsilon E \quad (5)$$

$$J = [\sigma'(\omega) - i\sigma''(\omega)]E = \sigma E \quad (6)$$

$$B = \mu_0 H \quad (7)$$

where $\varepsilon = \varepsilon' - i\varepsilon''$ is the complex permittivity, $\sigma = \sigma' - i\sigma''$ the complex conductivity and μ_0 the permeability of free space.

With assumptions made of \underline{E} and \underline{B} existing with a single angular frequency ω , $\underline{E} = \underline{E}_0 e^{i\omega t}$ and $\underline{B} = \underline{B}_0 e^{i\omega t}$ with \underline{E} related to current density via a conductivity σ , equations (1) and (2) become:

$$\underline{\nabla} \times \underline{E} + i\omega \underline{B} = 0 \quad (8)$$

$$\underline{\nabla} \times \underline{H} - (\sigma + i\omega\varepsilon)\underline{E} = 0 \quad (9)$$

Equations (8) and (9) are homogeneous and in frequency domain form and only apply to source-free regions - regions of no electric or magnetic source field. If a region exhibits a magnetic field source the relationship to \underline{H} is through $\underline{B} = \mu \underline{H} + \underline{J}_m$, whereas for an electric source field \underline{j} is related to \underline{E} by $\underline{j} = \sigma \underline{E} + \underline{J}_e$. These two terms, \underline{J}_m and \underline{J}_e , constitute the source terms which convert equations (8) and (9) into inhomogeneous equations:

$$\underline{\nabla} \times \underline{E} + i\omega\mu_0 \underline{H} = -\underline{J}_m \quad (10)$$

$$\underline{\nabla} \times \underline{H} - (\sigma + i\omega\varepsilon)\underline{E} = \underline{J}_e \quad (11)$$

\underline{J}_m is a magnetic source current, and \underline{J}_e is an electric source current.

2.4 Application of the Schelkunoff potentials

The application of Schelkunoff potentials facilitates the easy transition of E and H derivatives by differentiation because they are parallel to the source fields compared with individual fields themselves.

In the TEM geophysics method a current loop is used as the source. Therefore the TEM source is a magnetic dipole and the electric source term is zero. Thus the electromagnetic field, in general, is entirely described by the governing equations:

$$\underline{\nabla} \times \underline{E} + i\omega\mu_0\underline{H} = -\underline{J}_m \quad (12)$$

$$\underline{\nabla} \times \underline{H} - (\sigma + i\omega\epsilon)\underline{E} = 0 \quad (13)$$

With this simplification, the expression of electric field in terms of a Schelkunoff potential \underline{F} is derived by taking the divergence of (13) giving:

$$\underline{\nabla} \cdot (\underline{\nabla} \times \underline{H}) - (\sigma + i\omega\epsilon)\underline{\nabla} \cdot \underline{E} = 0$$

The divergence of a curl of a vector constituting zero simplifies this to $\underline{\nabla} \cdot \underline{E} = 0$. This means the electric field \underline{E} can be expressed as the curl of a vector in terms of Schelkunoff potential \underline{F} :

$$\underline{E} = -\underline{\nabla} \times \underline{F} \quad (14)$$

Substituting:

$$\underline{H} = -(\sigma + i\omega\epsilon)\underline{F} + \frac{1}{i\mu_0\omega}\underline{\nabla}(\underline{\nabla} \cdot \underline{F})$$

and taking the curl gives:

$$\underline{\nabla} \times \underline{H} = -(\sigma + i\omega\epsilon)\underline{\nabla} \times \underline{F} + \frac{1}{i\mu_0\omega}\underline{\nabla} \times [\underline{\nabla}(\underline{\nabla} \cdot \underline{F})]$$

Or:

$$\underline{\nabla} \times \underline{H} = (\sigma + i\omega\epsilon)\underline{E} + \frac{1}{i\mu_0\omega}\underline{\nabla} \times [\underline{\nabla}(\underline{\nabla} \cdot \underline{F})]$$

As the gradient of the divergence of any vector is zero this equation reduces to (13). This implies that:

$$\underline{H} = -(\sigma + i\omega\epsilon)\underline{F} + \frac{1}{i\mu_0\omega}\underline{\nabla}(\underline{\nabla} \cdot \underline{F}) \quad (15)$$

is indeed a suitable solution of (13) in which the magnetic field \underline{H} is expressed in terms of Schelkunoff potential \underline{F} .

Putting (14) and (15) in equation (12) gives:

$$\underline{\nabla} \times (-\underline{\nabla} \times \underline{F}) - i\mu_0\omega(\sigma + i\omega\epsilon)\underline{F} + \underline{\nabla}(\underline{\nabla} \cdot \underline{F}) = -\underline{J}_m \quad (16)$$

Using the vector identity $\underline{\nabla} \times (\underline{\nabla} \times \underline{F}) = \underline{\nabla}(\underline{\nabla} \cdot \underline{F}) - \nabla^2 \underline{F}$ equation (16) reduces to:

$$\nabla^2 \underline{F} - i\mu_0\omega(\sigma + i\omega\varepsilon)\underline{F} = -\underline{J}_m \quad (17)$$

This is the inhomogeneous Helmholtz equation which, when simplified by the wave number k , becomes:

$$\nabla^2 \underline{F} + k^2 \underline{F} = -\underline{J}_m \quad (18)$$

where k is defined as:

$$k^2 = \mu_0\varepsilon\omega^2 - i\mu_0\sigma\omega \quad (19)$$

In which $\mu_0\varepsilon\omega^2$ is the displacement current and $-i\mu_0\sigma\omega$ is the conduction current.

2.5 Establishing the step response using the transient Magnetic dipole

Following the approach outlined by Ward and Hohmann (1987), in the application of TEM the current I in the loop of area A is the magnetic source at the surface of the earth. The source dipole moment is $\underline{m} = IA\hat{x}$ with the vertical direction defined as the x -direction. The provision of the source stems from the time variance of this dipole moment. The source term is thus a vector in the x -direction. The Greens Function for (18) is:

$$G(r) = \frac{1}{4\pi r} e^{-ikr} \quad (20)$$

which results in the vector potential for an arbitrary magnetic source being given by:

$$\underline{F}(r) = \int_{V'} \frac{e^{ik|\underline{r}-\underline{r}'|}}{4\pi|\underline{r}-\underline{r}'|} \underline{J}_m(\underline{r}') dV' \quad (21)$$

In this expression \underline{r}' represents the magnetic source location contained in the volume of space V' over which the integral is evaluated, and r is the location at which \underline{F} is to be calculated. In TEM, for a single dipole source the source term \underline{J}_m is related to the rate of change of the dipole moment i.e. for fixed area A , to the rate of change of the current I . The source term can be written as:

$$\underline{J}_m = i\omega\mu_0 IA\delta(x)\delta(y)\delta(z)\hat{x} \quad (22)$$

where the $i\omega$ denotes the time derivation of the current and the three delta functions denote the spatial location of the source. Substituting (21) into (22) and evaluating the integral yields the solution for \underline{F} of:

$$\underline{F} = \frac{i\omega\mu_0}{4\pi r} e^{-ikr} \hat{x} \quad (23)$$

Equation (23) can be used to extract the electric field (\underline{E}) and the magnetic field (\underline{H}). When inserted into (14) and (15) the resulting expressions for (\underline{E}) and (\underline{H}) are:

$$\underline{E} = \frac{i\omega\mu_0 m}{4\pi r} (ikr + 1)e^{-ikr} \left(\frac{z}{r} \underline{\hat{y}} - \frac{y}{r} \underline{\hat{z}} \right) \quad (24)$$

$$\underline{H} = \frac{m}{4\pi r^3} e^{-ikr} \left\{ \left(\frac{x^2}{r^2} \underline{\hat{x}} + \frac{xy}{r^2} \underline{\hat{y}} + \frac{xz}{r^2} \underline{\hat{z}} \right) (-k^2 r^2 + 3ikr + 3) \right. \\ \left. + (k^2 r^2 - ikr - 1) \underline{\hat{x}} \right\} \quad (25)$$

Here $\underline{\hat{F}}$, $\underline{\hat{E}}$, and $\underline{\hat{H}}$ are expressed as functions of the angular frequency (ω), while the Fourier Transformed impulse response function $f(t)$, denoted by \underline{F} , contains descriptions of how the input impulse magnetic field is modified by the earth.

Practically, the essence of TEM geophysics method is the switching off of a steady current in a source loop causing the collapse of the induced magnetic field in the ground. The subsequent sudden rise in current is encapsulated by a unit step-response represented by $u(t)$ where the current is zero until time t and becomes one for times $> t$. The behaviour of a system in response to this characteristic input is described by:

$$g_+(t) = \int_{-\infty}^{\infty} f(\tau)u(t - \tau)d\tau = \int_0^t f(\tau)d\tau \quad \text{for } t \geq 0 \quad (26)$$

The convolution of the impulse response of the system with the unit step response function is represented by the first integration. The second integral depends on the transient nature of the input which dictates the system's response example for $\tau < 0$ is $u = 0$. In an instance where a system experiences an initial input current turn off the behaviour is determined by:

$$g_-(t) = \int_{-\infty}^{+\infty} f(\tau)[1 - u(t - \tau)]d\tau = \int_0^{+\infty} f(\tau)d\tau - \int_0^t f(\tau)d\tau$$

which can be described as the step off response:

$$g_-(t) = g_+(\infty) - g_+(t) \quad \text{for } t \geq 0 \quad (27)$$

where $g_+(\infty)$ is the step-response at infinitely long periods (time).

2.6 Analytical solution for the transient response

The relationship between step-response and F is exploited through a Laplace Transform:

$$g_+(t) = L^{-1} \left[\frac{f(s)}{s} \right] \quad (28)$$

L^{-1} indicates the inverse Laplace Transform. $F(s)$ refers to \underline{F} as in (24) but swapping $i\omega$ for s . The resulting nomenclature of (23), (24), and (25) taking in to account:

$$ikr = \sqrt{i^2 k^2 r^2} = \sqrt{i\mu_0 \omega \sigma r^2} = \sqrt{s\mu_0 \sigma r^2}$$

and:

$$(ikr + 1) = s \left(\frac{ikr}{s} + \frac{1}{s} \right) = s \left(\frac{\sqrt{i^2 k^2 r^2}}{s} + \frac{1}{s} \right) = s \left(\sqrt{\frac{\mu_0 \sigma}{s}} + \frac{1}{s} \right)$$

gives:

$$\frac{F(s)}{s} = \frac{\mu_0 m}{4\pi r} e^{-\sqrt{s\mu_0 \sigma r^2}} \hat{x} \quad (29)$$

$$\frac{E(s)}{s} = s \frac{\mu_0 m}{4\pi r^3} \left(\sqrt{\frac{\mu_0 \sigma}{s}} + \frac{1}{s} \right) e^{-\sqrt{s\mu_0 \sigma r^2}} (z\hat{y} - y\hat{z}) \quad (30)$$

$$\frac{H(s)}{s} = \frac{m}{4\pi r^3} e^{-ikr} \left\{ \begin{aligned} & \left(\frac{x^2}{r^2} \hat{x} + \frac{xy}{r^2} \hat{y} + \frac{xz}{r^2} \hat{z} \right) \left(\mu_0 \sigma r^2 + 3 \sqrt{\frac{\mu_0 \sigma}{s}} r + \frac{3}{s} \right) \\ & + \left(-\mu_0 \sigma r^2 - \sqrt{\frac{\mu_0 \sigma}{s}} r - \frac{1}{s} \right) \hat{x} \end{aligned} \right\} \quad (31)$$

The conversion of \underline{F} , \underline{H} , and \underline{E} to time variation form can now be done on (29), (30), and (31) through some of the inverse Laplace Transform standard identities:

$$L^{-1} = [sF(s)] = \frac{d}{dt} f(t)$$

$$L^{-1} = [e^{-\alpha\sqrt{s}}] = \frac{\alpha}{2\sqrt{\pi t^3}} e^{-\alpha^2/4t} \quad \text{for } \alpha > 0$$

$$L^{-1} = \left[\frac{1}{\sqrt{s}} e^{-\alpha\sqrt{s}} \right] = \frac{1}{\sqrt{\pi t}} e^{-\alpha^2/4t} \quad \text{for } \alpha \geq 0$$

$$L^{-1} = \left[\frac{1}{s} e^{-\alpha\sqrt{s}} \right] = \text{erfc} \left(\frac{\alpha}{2\sqrt{t}} \right) \quad \text{for } \alpha \geq 0$$

where erfc is the complementary error function and $\alpha = \sqrt{\mu_0 \sigma r^2}$. Hence taking the expression for $\frac{F(s)}{s}$ and:

$$L^{-1} \left[\frac{F(s)}{s} \right] = \frac{\mu_0 m}{4\pi r} L^{-1} [e^{-\alpha\sqrt{s}}] \hat{x} = \frac{\mu_0 m}{4\pi r} \frac{\alpha}{2\sqrt{\pi t^3}} e^{-\alpha^2/4t} \hat{x}$$

which reduces to:

$$L^{-1} \left[\frac{F(s)}{s} \right] = \frac{m\theta^3}{\pi^{3/2}} e^{-\theta^2 r^2} \hat{x} \quad (32)$$

with:

$$\theta = \left(\frac{\mu_0 \sigma}{4t} \right)^{1/2} \quad (33)$$

Similarly:

$$L^{-1} \left[\frac{E(s)}{s} \right] = \frac{2m\theta^5}{\pi^{3/2}\sigma} e^{-\theta^2 r^2} (z\hat{y} - y\hat{z}) \quad (34)$$

and:

$$L^{-1} \left[\frac{H(s)}{s} \right] = \frac{m}{4\pi r^3} \left[\left(\frac{x^2}{r^2} \hat{x} + \frac{xy}{r^2} \hat{y} + \frac{xz}{r^2} \hat{z} \right) \left(\left(\frac{4}{\sqrt{\pi}} \theta^3 r^3 + \frac{6}{\sqrt{\pi}} \theta r \right) e^{-\theta^2 r^2} + 3 \operatorname{erfc}(\theta r) \right) - \left(\left(\frac{4}{\sqrt{\pi}} \theta^3 r^3 + \frac{2}{\sqrt{\pi}} \theta r \right) e^{-\theta^2 r^2} + \operatorname{erfc}(\theta r) \right) \hat{x} \right] \quad (35)$$

Thus far (32), (34), and (35) can be used to extract the Schelkunoff vector potential (\underline{F}), electric field (\underline{E}), and magnetic field (\underline{H}) based on the provision of the relevant $g_+(t)$. However in the TEM geophysics method the abrupt switching off of current requires $g_-(t) = g_+(\infty) - g_+(t)$, assuming that the infinite time after switch off has no response this means that $g_-(t) = -g_+(t)$. In this case the time variations in the field are:

$$f(t) = -\frac{m\theta^3}{\pi^{3/2}\sigma} e^{-\theta^2 r^2} \hat{x} \quad (36)$$

for the Schelkunoff vector transient response:

$$e(t) = \frac{2m\theta^3}{\pi^{3/2}\sigma} e^{-\theta^2 r^2} (-z\hat{y} + y\hat{z}) \quad (37)$$

for the electric field transient response and:

$$h(t) = \frac{m}{4\pi r^3} \left[\left(\frac{x^2}{r^2} \hat{x} + \frac{xy}{r^2} \hat{y} + \frac{xz}{r^2} \hat{z} \right) \left(3 \operatorname{erfc}(\theta r) - \left(\frac{4}{\sqrt{\pi}} \theta^3 r^3 + \frac{6}{\sqrt{\pi}} \theta r \right) e^{-\theta^2 r^2} \right) - \left(\operatorname{erfc}(\theta r) - \left(\frac{4}{\sqrt{\pi}} \theta^3 r^3 + \frac{2}{\sqrt{\pi}} \theta r \right) e^{-\theta^2 r^2} \right) \hat{x} \right] \quad (38)$$

for the magnetic field transient response.

In practice, the quantity measured is the induced voltage in the receiver coil and as a result the essential quantity necessary for the voltage induced is the time derivative of the magnetic field.

Taking the derivative of equation (38) gives the equation:

$$\frac{\partial h(t)}{\partial t} = \frac{4m\theta^5}{\pi^{3/2}\mu_0\sigma} e^{-\theta^2 r^2} \left[\left(\frac{x^2}{r^2} \hat{x} + \frac{xy}{r^2} \hat{y} + \frac{xz}{r^2} \hat{z} \right) \theta^2 r^2 + (1 - \theta^2 r^2) \hat{x} \right] \quad (39)$$

Equation (39) provides the means to calculate the voltage induced in the receiver. The dependence of $h(t)$ on θ (as defined in equation (33)) allows this to be related to the subsurface conductivity.

Chapter 3 Description of the study area

3.1 Regional

Papua New Guinea (PNG) is situated north of Australia, occupying the eastern side of New Guinea Island and bounded by latitudes 0° and 12°S, and longitudes 140° and 160°E. It shares the only land border with the Indonesian province of West Papua to the west and 3 maritime boundaries with Australia to the south, the Solomon Islands to the east, and the Federal State of Micronesia to the north. Having 22 provinces spanning across a total area of 462,840 km², PNG is the largest of all Pacific nations. The country can be divided into four regions: Southern (Pink), Highlands (Orange), Momase (Purple), and the New Guinea Island (Light Green) as indicated by the insert of Figure 3.1. PNG's distinct features are its rugged and densely forested terrains forming the spine of the country, surrounded by lowland rainforest, flood plains, and swamps, and its volcanic and coral atoll islands. Although PNG has a huge land area only 13% of the land area is occupied by human settlement, mostly in the Highlands region and the eastern coastline of mainland PNG. Port Moresby is the capital city and is located in the Southern region, contained within the Central Province (Figure 3.1).

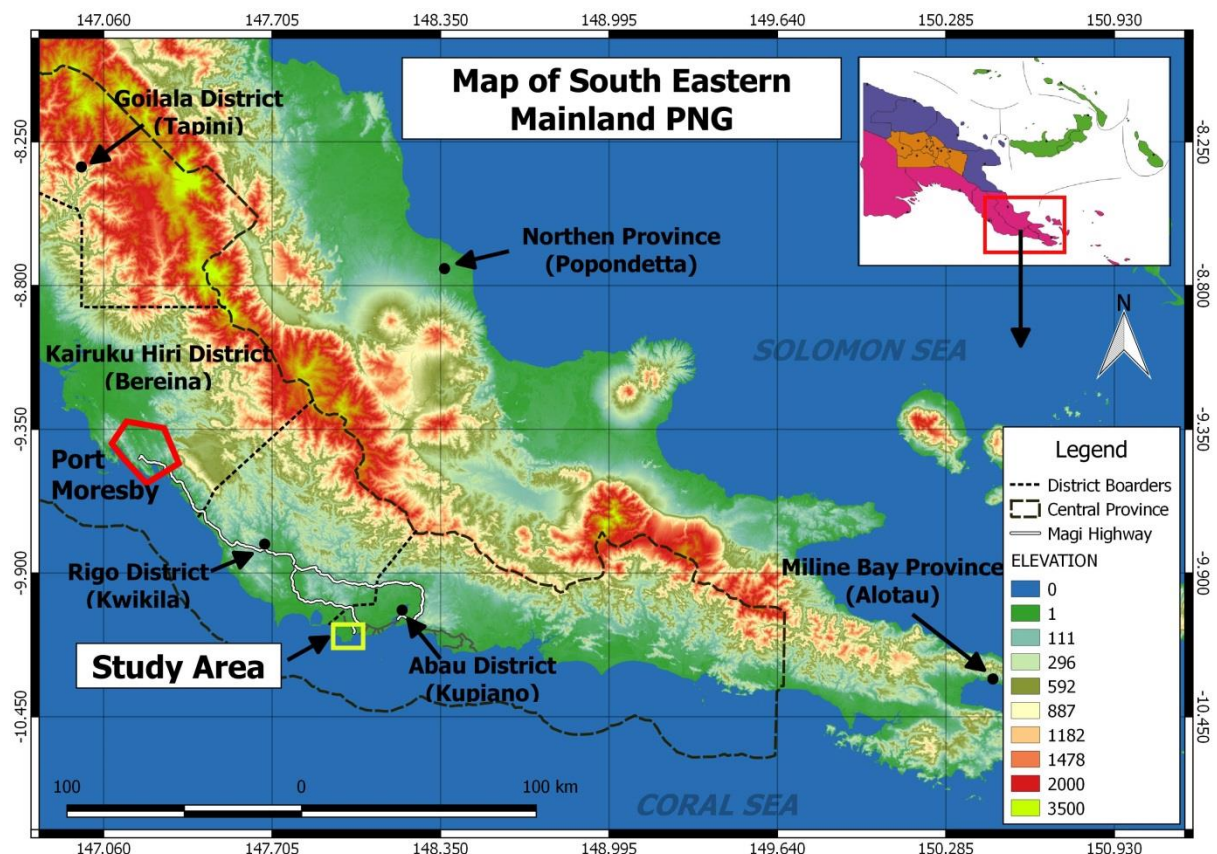


Figure 3.1 Map of South Eastern mainland PNG outlining the Central province and various significant locations including the survey area (insert map courtesy of Wikipedia).

3.2 Local settings

The extent of the study area mainly covers customary land belonging to tribes of the mother village Maopa. Situated in the Keakalo bay of the westernmost local-level Government or district subdivision Aroma, Maopa is the most populated area of the district of Abau which occupies the easternmost part of the Central province (Figure 3.1). Kupiano is its district headquarters or town, 15 km east of the survey area - a distance made up of a 40-minute truck ride and a short dinghy ride (6 min) over the Marshall Lagoon. The district headquarters provide vital services such as hospitals, banks, and high schools to vastly disconnected and remote parts. The district shares a provincial border in the north and east with the Northern and Milne Bay provinces respectively. Access to Maopa from the capital Port Moresby is by road covering an estimated distance of 155 km and duration of 3-5 hours by truck across the district of Rigo. The landform, topography and meteorological factors play a key role in the accessibility of outward stations, a predicament not uncommon throughout PNG.

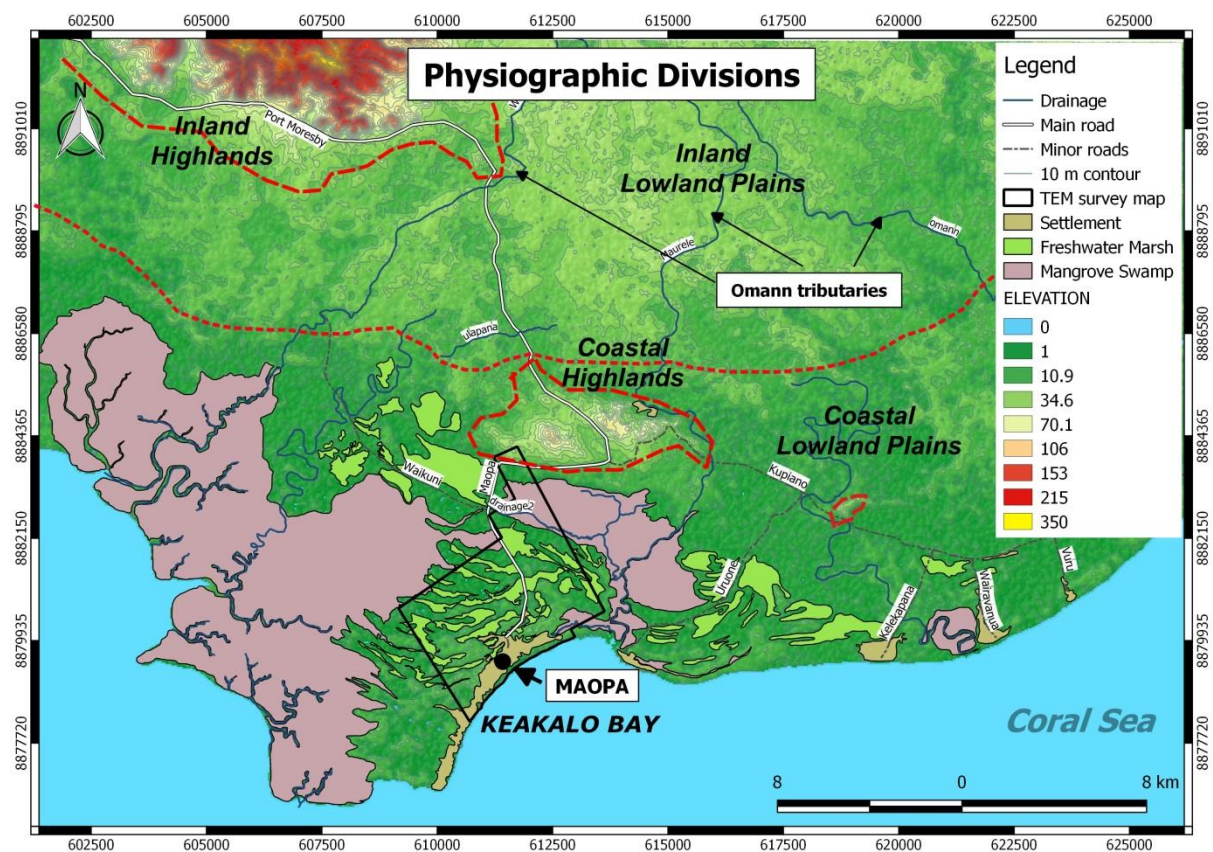


Figure 3.2 Simple physiographic map of the study area showing four main physiographic regions. Red dashed lines denote the two Highlands region whereas, the red dotted lines denote the boundary separating the Inland Lowland Plains from the Coastal Lowland Plains.

Keakalo Bay hosts numerous villages along the full stretch of the sandy beach front with Maopa being at the centre of these establishments (Figure 3.2). Villages are mostly built on the elevated

sand deposits because of easy access to clean freshwater from the shallow sandy aquifer and also in response to high vulnerability of the interior to inundation. Economic activity is small scale, largely because people are subsistence farmers who practice shifting cultivation and small scale fishing for their own sustenance. On top of gardening and fishing there are a range of important activities including: hunting, fetching firewood, fetching water, canoe racing, church, and sport. However, the most critical of the activities is fetching water from wells as freshwater supplies become more contaminated.

3.3 Physiography

Based on Nevin Fenneman's 1916 three-tier classification approach (Fenneman, 1916) a sufficient extension of the study area was broadly divided into 4 physiographic regions (Figure 3.2). The Inland Highlands in the northwest, the Coastal Highlands in the central region, and two dominant regions of the Lowland Plains that divide the whole region in half. The northern half is occupied by the Inland Lowland Plains whereas to the south are the Coastal Lowland Plains.

The Lowland Plains regions dominate. Such regions are quite common in mainland PNG because of the heavy runoff from the mountain ranges in the interior of mainland PNG. Specifically, in this region, Lowland Plains are recent deposits of sediments primarily from the Owen Stanley mountain ranges deposited by the Omond River and its main tributaries Wariwa, Maurele and Kelerakwa. While the low gradient relief of the lowland plains is widely observed, the main factor dividing the northern and the southern regions is their relative proximity to mountain ranges and the coastline respectively. The Inland Lowland Plains are distinctive because of vast coverage of lowland rainforest with patches of human-induced grassland. On the other hand, in the Coastal Lowland Plains, the influence seawater is extensive, aided by the low topographical gradients which result in the presence of mangrove swamps and mangrove forest hugging the main estuaries, freshwater wetland marsh, and beach sand. Areas free of mangrove swamps and freshwater wetlands are characterised by alluvium and are covered by fertile grasslands.

Features formed earlier, like the two Highland regions, are mostly covered by lowland deposits. They are a result of raised older marine sediments during the collision of the Oceanic Plate and the continent of Australia. They are a source for limestone and vegetation is mostly savannah grassland mixed with eucalyptus trees. Perhaps the most important resource of these regions is their limestone karst groundwater.

3.4 Climate

McAlpine et al. (1983) provide a detailed discussion of the climate of PNG from which localized climatic details for the study area can be either inferred or estimated. Hall (1984) gave a good summary of McAlpine et al. (1983) incorporating Northern Australia's climate. The World Bank climate change knowledge portal (<https://climateknowledgeportal.worldbank.org/watershed/378/climate-data-historical>) also provides information about current average annual rainfall and temperatures. PNG is situated in a region known as the intertropical convergence zone (ITCZ). The region is not only central to latent heat release and the vertical transportation of that heat energy but also central to the accumulation of convective disturbance and convective cloud cover. The massive topography of the Island of New Guinea, which extends westward through Indonesia to Malaysia together with the broad warm ocean surface temperatures greatly enhances convection in moist equatorial airstreams on the one hand, and on the other creates low surface pressure along with warm air temperatures and moisture content. The mobility and distribution of these disturbances are largely controlled by two main seasonal airstreams of Southeast Trade winds and the Northwest Monsoon, which are controlled by the alternating ITCZ. The Southeast Trade winds are dominant from May to October, bringing heavy rains to areas subject to windward slopes. The North westerly Monsoonal winds are active from December to March with contrasting variable air flows emanating from many directions causing episodic heavy rainfalls and sporadic dry conditions. Rainfalls during this period are largely localized and heavy for the most parts of PNG except for the Highland regions.

3.4.1 Rainfall

Rainfall rates in PNG are generally high (2000 to 3500 mm annually) but are largely variable due to the direction and speed of the air stream and the topography (Figure 3.3).

The study area is situated in the region marked as having the second least amount of rainfall (2000-4000 mm/yr) but its close proximity to the south-eastern region of the least amount of rainfall (0-2000 mm/yr) to the west is important to note. Local rainfall estimates from the World Bank Climate Change Knowledge Portal show average annual rainfall and temperature minima and maxima are in the order of 100 and 300 mm and 25 and 27.5 °C respectively (Figure 3.4). This average rainfall is significantly less than that given by McAlpine et al. (1983). However, the total amount of rainfall received in this area for the years averaged was 2425 mm which is consistent with the McAlpine et al. (1983) classifications.

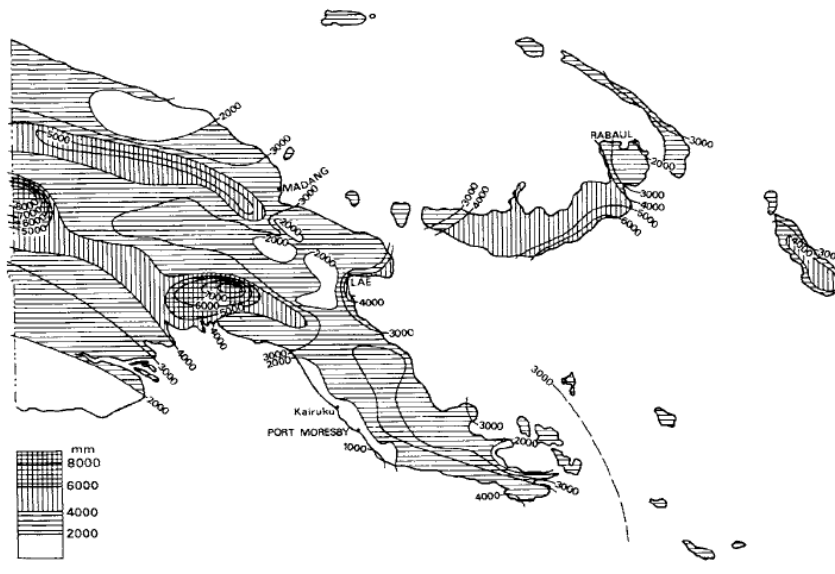


Figure 3.3 Annual rainfall classification of PNG (After MacAlpine et al. 1983).

The seasonal variability is mainly dictated by the South East Trade winds and the North Westerly Monsoon winds described earlier with the latter bringing the wettest season compared with the former. The strategic placement of the study area relative to its position in PNG and latitude primarily dictates the type of climate it is exposed to.

Average Monthly Temperature and Rainfall of Watershed #378 for 1991-2016 at Location (148.04,-10.10)

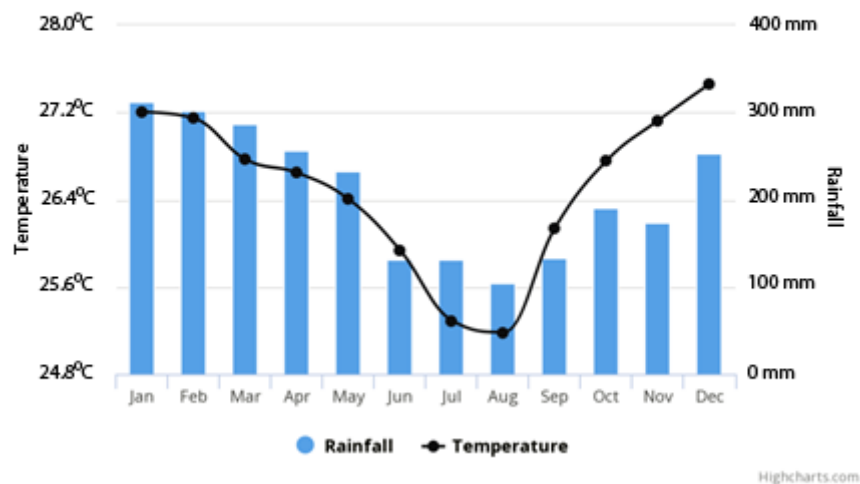


Figure 3.4 Annual rainfall of survey area (<https://climateknowledgeportal.worldbank.org/watershed/378/climate-data-historical>).

3.4.2 Evaporation

Evaporation is the transfer of water from surfaces of water bodies, land, and vegetation to the atmosphere. This process is named differently in the case of transfers occurring in plants where it is referred to as transpiration. Because it is the main driver for the hydrological cycle it is important to

considered particularly when hydrological studies are concerned.. In this case, the study area, in accordance with the McAlpine et al. (1983) findings, experiences very high annual evaporative rates recording values ranging between 2000-2250 mm (Figure 3.5). This implies that recharge of the groundwater system from the high annual rainfall is limited.

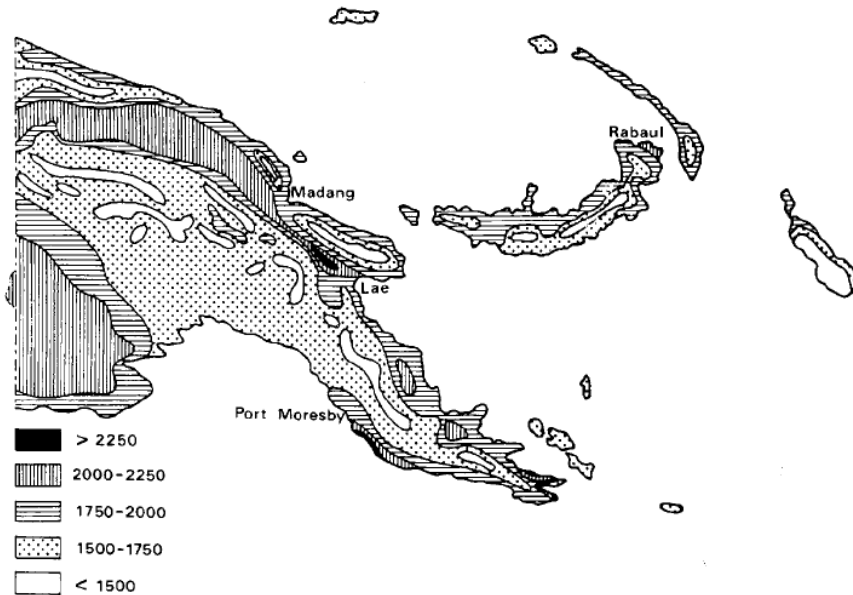


Figure 3.5 Evaporation rate of PNG (after MacAlpine et al. 1983).

3.5 Geology

The geology of the study area (Figure 3.6) follows after Pieters (1978) which is predominantly sedimentary of varying lithology and age, superimposed in some instances by minor intrusive and extrusive volcanism. Late to middle Eocene and Eocene accretionary sediments of the Port Moresby beds and the Bomuguina beds respectively make up the bedrock units. The contact between these beds is not known. However, it is speculated that it may be in the vicinity of the study area. This is strongly supported by a major fault mapped at the exposure of the contact between the Port Moresby Beds and the Early Miocene to Late Pliocene Kupiano Beds in the northwest (Figure 3.6). The Port Moresby beds are the dominant of the two formations in this region with a thickness of up to 2000m. They underlie the southernmost lowlands as a curvilinear belt of hills trending northwest to the west-northwest and have main constituents of undivided siliceous argillite, shale, calcilutite, minor chert, and calcarenite. The Bomuguina beds, on the other hand, are about 500 m thick, occurring on the surface in small scale further to the east out of the survey area and are mainly composed of well-bedded calcilutite, siltstone, sandstone, and minor chert. Both basement units

typically occur at an inferred depth of 200 - 500 m, particularly in areas overlain either by the Kupiano beds or the recent Pleistocene to Holocene Alluvium deposits.

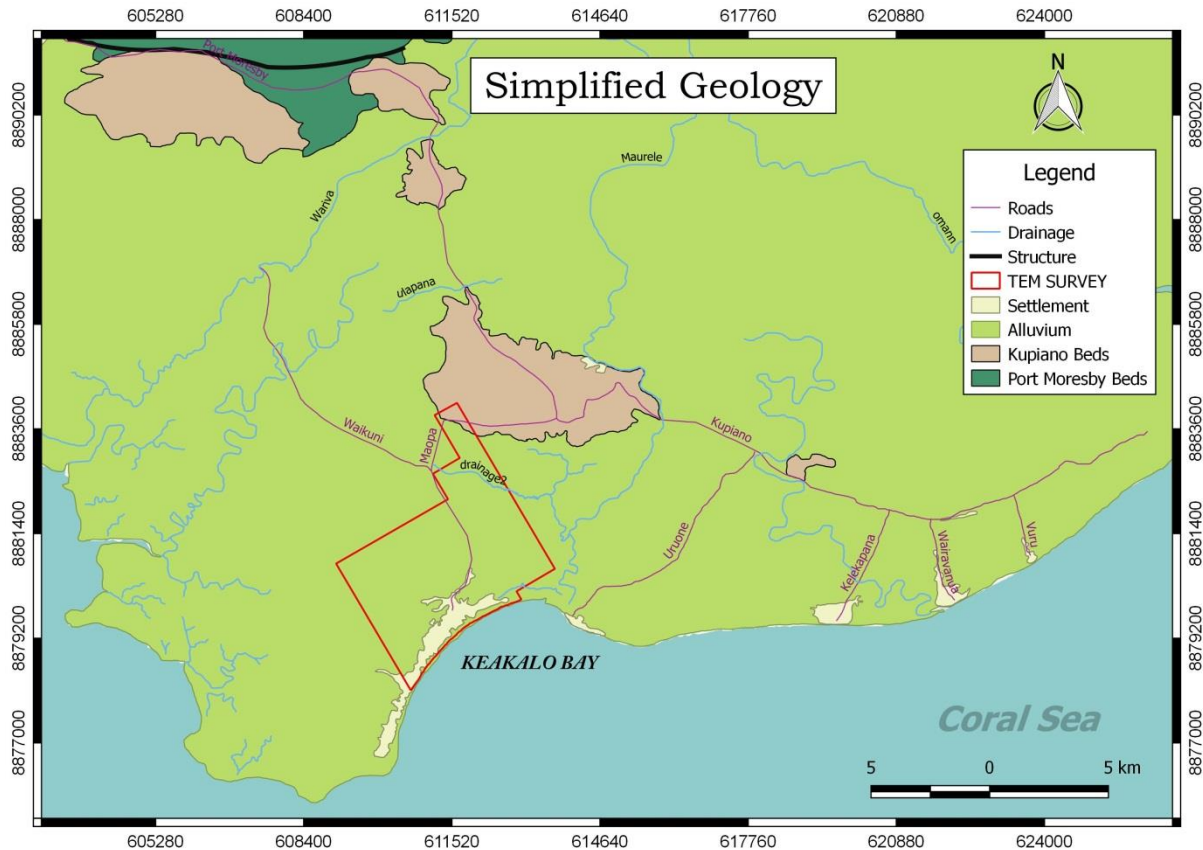


Figure 3.6 Simplified map of the geology of the survey area (After Pieters, 1978).

While observations of recent alluvium deposits overlay the Port Moresby beds to the west, the broad occurrence of the older Kupiano beds strongly supports its predominance as the main cover of the basement unit in the study area. The Kupiano beds are made up of sandstone, shelly sandstone, siltstone, mudstone, and minor conglomerate limestone. Their low, undulating and dendritic drainage and limestone strike ridges form the two primary landscape units that rise above the lowlands (alluvium plains) (Pieters, 1978). The Pleistocene and Holocene sediment constituents are deposits of gravel, sand, and silt, intermixed littoral deposits and raised coral reefs that may be up to 500 m thick. These alluvium deposits are the main surficial geological facies covering 90% of the lowlands extending landward from the coastline to the foothills of Owen Stanley mountain range. Their mechanism of deposition varies between fluvial and littoral with some instance of raised coral reefs. Although little can be inferred about the dominant mechanism of deposition and its frequency, at least in the vicinity of the survey area, 800 m landward from the Keakalo Bay coastline evidence of marine deposition overlain by silt and loam provides an insight to the sequential order in this area. While it is still subject to debate, it can be inferred particularly in parts of the lowlands within a distance of 1000 m from the coastline that coastal marine sediments have been deposited

earlier than the Holocene fluvial alluvium and can be expected to be overlain by the fluvial deposits. In contrast, further away from the coastline, lowland deposits further inland may be predominantly fluvial. Beach fronts in the study area are mainly iron sands but are mixed with fine marine sediments and organic matter around the mangrove habitats.

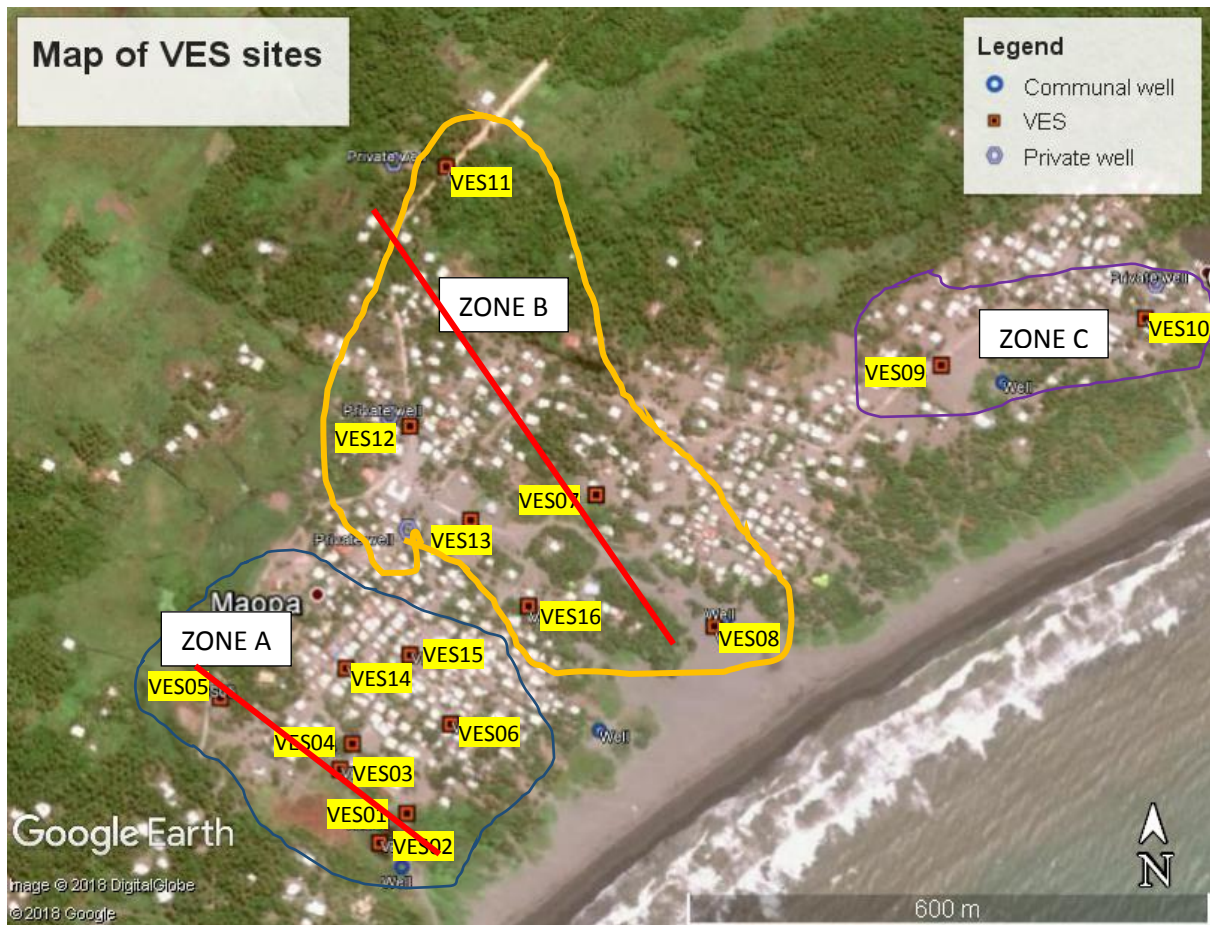
3.6 Hydrology

The study area has a good mix of lowland tropical coastal hydrology. Apart from the ocean, the main hydrological features on land are the mangrove swamps, a buffer zone of marshy freshwater wetland and low gradient flow rivers that dissect the alluvium deposits (Figure 3.2). Three main low gradient flow rivers contribute to the collective physiography of the area. Wariva and Ulapana are the most prominent drainage systems in the western part, forming two major estuaries in that region although extensive occurrences of minor estuaries exist. To the east, Maurele is the main river that drains the surface flows from the highlands forming a large sandy bank estuary popular among locals for picnic outings. These river systems and their estuaries provide perfect ingredients for the existence of the brackish mangrove swamps and their biota, which are mostly sustained by tidal changes. The buffer zone of freshwater marsh wetlands are primarily fed directly by rainfall and runoff from the elevated and developed sand dunes near the beach front. Infiltrations from flood waters occur mainly through the Ulapana river in the north northwest of the survey area but are infrequent. Changes in water levels of the wetland are largely dictated by seasonal changes and the climate. It is also important to note limestone karst springs do exist in the Coastal Highlands region to the north and supply fresh water to villages in this region.

3.7 Previous study

An unpublished preliminary study by Verave (2018) is the sole geo-scientific study carried out in the study area where the main dependency of communities on groundwater resources is being threatened by saltwater intrusion. The study was aimed at delineating the extent of saltwater intrusion and also to locate areas of sufficient aquifer thickness in order to understand the characteristics of the groundwater and the influence of saltwater intrusion. The study was also intended to locate better yielding freshwater wells.

To achieve the goals of the survey the study used a Schlumberger DC resistivity survey which involved collecting Vertical Electrical Soundings (VES) in a spatial distribution strictly determined by accessibility and applicability of the resistivity method chosen. Ultimately, 16 VES were measured



covering an area about 0.24 km² with denser coverage over Zone A and Zone B (Figures 3.7 and 3.8). The furthest sounding is about 750 m from the coastline while the closest are distributed along the coastline varying between 100 and 200 m.

Figure 3.7 Map of VES (map courtesy of Google Earth).

The study used an ABEM Terrameter SAS 1000 instrument where the current was injected into the ground via two outer electrodes which were separated by a distance AB. The resulting earth response voltage is then measured by two additional inner electrodes whose separation is MN. At each site AB is gradually increased and the author in this study used eight separations per decade on a log scale encompassing maximum current electrode separation (AB/2) of 100 m and MN/2 of 0.1 to 15 m. The probing depth of the technique is primarily determined by the separation of the current electrodes (AB) and the subsurface resistivity. Therefore the greater the current electrode separation the deeper the current penetration. In addition, based on the conductive properties of the ground, current flows through areas of least resistance thus when it encounters a conductive medium it tends to remain in the region longer until the spread parameters are changed.

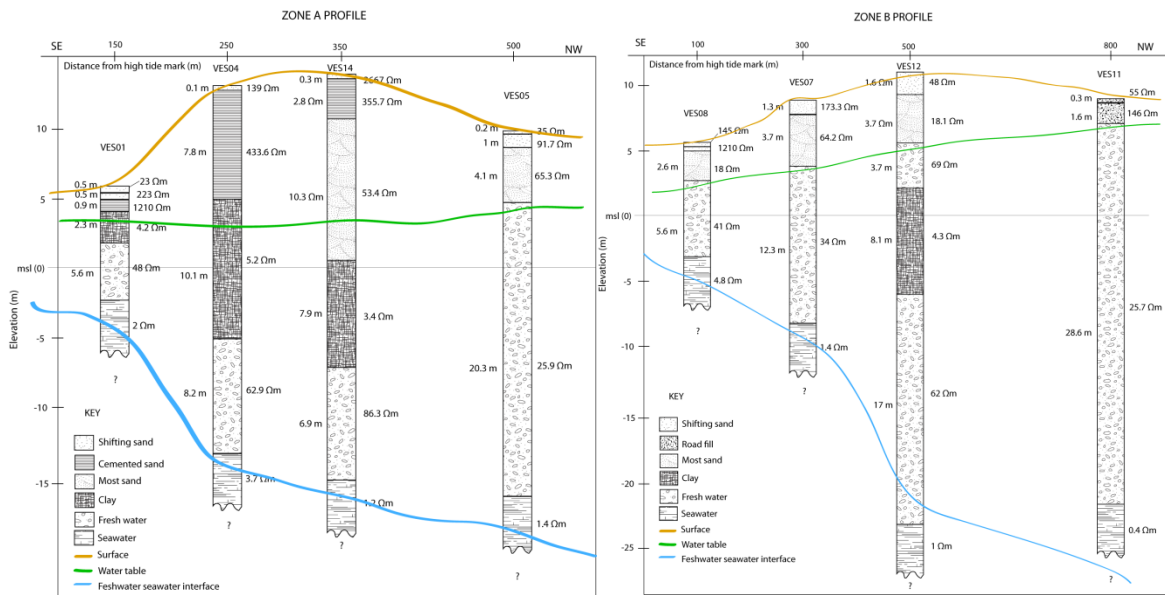


Figure 3.8 Zone A and Zone B cross-section showing inferred interpretations of layers and their modelled resistivity. For each section the layer thickness (in m) is shown on the left and the layer resistivity (in Ωm) is shown on the right. The brown, green, and blue lines denote the surface elevation, freshwater table, and top of saline zone respectively. The inference of shallow layering are based on surface observation and inspections of diggings from hand dug wells.

The major findings of the preliminary study are summarized by two geoelectric cross-sectional profiles (Figure 3.8). They incorporate selected VES taken from Zone A and Zone B and are aligned perpendicular to the coastline as denoted by red lines (Figure 3.7). The cross-sectional profiles show inferred interpretations of the various layers and the probable interface between freshwater and seawater. The profiles show four major geoelectric layers occurring at various depths and thicknesses. Beneath Zone A the profile is dominated in by a resistive layer underlain by a very conductive one. The former is interpreted as a cemented sand formation closer to the surface while the latter is a clay layer capping the groundwater table. In places where the clay is absent a medium of fine and more sorted sand, with a resistivity indicating it may be moist or damp, sits above the groundwater zone which has a resistivity of around 25-50 Ωm . Observations in diggings confirm this interpretation. Results across Zone B show a generally consistent sequence of layers although conductive clay occurs beneath VES 12. This indicates the possibility of a double aquifer situation, with the deeper being likely semi-confined and the shallower unconfined.

In this work, the main focus was more on the characterization of the groundwater resource and the saltwater influence as depicted in Figure 3.7. Firstly, the groundwater resource is characteristic of low lying coastal alluvium hydrology with sufficient aquifer thickness (12 - 20 m) observed in both profiles toward the interior about 400 - 700 m from the coastline. In most places, the water table is

at a depth of 3 - 4 m and occupies a stratum inferred as coarse sand perched aquifer. Second, it is apparent that all soundings have delineated freshwater-seawater interface at varying depths with shallowest (10 m) in sounding near the coastline while at great depths (20 -30 m) in soundings furthest from the coastline.

Although the study achieved its set goals, certain issues were noted:

- There is no indicated landward limit to saltwater intrusion. This may imply the possibility of a freshwater lens groundwater resource (as is characteristic of an atoll island). There is therefore a need to expand the study area to confirm the assumption.
- Little or no information about the possible alternative groundwater recharge apart from rainwater when the geomorphology is considered. The effect of the clay layer on recharge is similarly unknown.
- Accessibility and applicability issues associated with the DC Schlumberger resistivity method meant that extending the survey will be quite a demanding task and at times impossible.

Chapter 4 TEM survey and data processing

Verave (2018) in the previous study characterized saltwater intrusion in Maopa as progressive, revealing in all soundings the occurrence of the freshwater-saltwater interface at varying depths that increased gradually in the landward direction. The study also identified areas of potentially sufficient groundwater yields in soundings furthest from the coastline where aquifer thicknesses were observed to be greater. This assertion was based on 16 vertical electrical soundings (VES) mostly taken within the vicinity of the mother village Maopa which covered an area approximately 0.24 km² or 23.6 hectares in size (Figure 4.1).

While the findings offer an insight to the characteristics of the groundwater resource and the influence of seawater intrusion, they are, as described earlier, limited in three main ways. Firstly, the broad observance of saltwater interface across all soundings raises two questions – (i) where is the limit of the saltwater aquifer or intrusion?; (ii) is, despite the geological setting, the saltwater intrusion characteristic of small coral Islands? The second limitation arises from the necessity of identifying the sources of groundwater recharge and its possible connection with the Coastal Highlands region, an issue not addressed in the previous study. Thirdly, the DC Resistivity soundings were limited by accessibility and applicability issues commonly associated with the Schlumberger DC resistivity sounding method. This meant that acquisition of data could not be performed further inland.

The questions to be investigated can therefore be summarized as:

- 1) can the geometry of the saline water intrusion zone be mapped?
- 2) Is the wedge of saline groundwater of a form consistent with coastal plains of large islands or continents or of small coral islands?
- 3) Can the recharge zone for the coastal freshwater aquifer be connected to the coastal highlands to the north?
- 4) Is TEM more practical for imaging the resistivity structure than VES in the areas of poor accessibility.

4.1 TEM survey area

The current study addresses these limitations by conducting measurements of central loop TEM responses over an area almost 50 times the area covered by the VES survey. Figure 4.1 shows the contrast detailing the extent of the new TEM survey with respect to the VES survey and the placements of 88 TEM soundings along 7 lines. VES measurements from the previous study were

affected primarily by the difficulty of laying down lengthy spread lines in settlement and heavily vegetated areas. This resulted in the selection of sites in a random fashion for the acquisition of Schlumberger VES. By contrast, although such challenges existed, the execution of TEM soundings was carried out as planned with some notable minor alterations made particularly with regards to the repositioning of TEM soundings. A practice performed quite regularly throughout the course of the survey and is evident in the distorted line trends and irregularities of sounding intervals that are mainly attributed to the challenges of diverse physiography encountered in the study area.

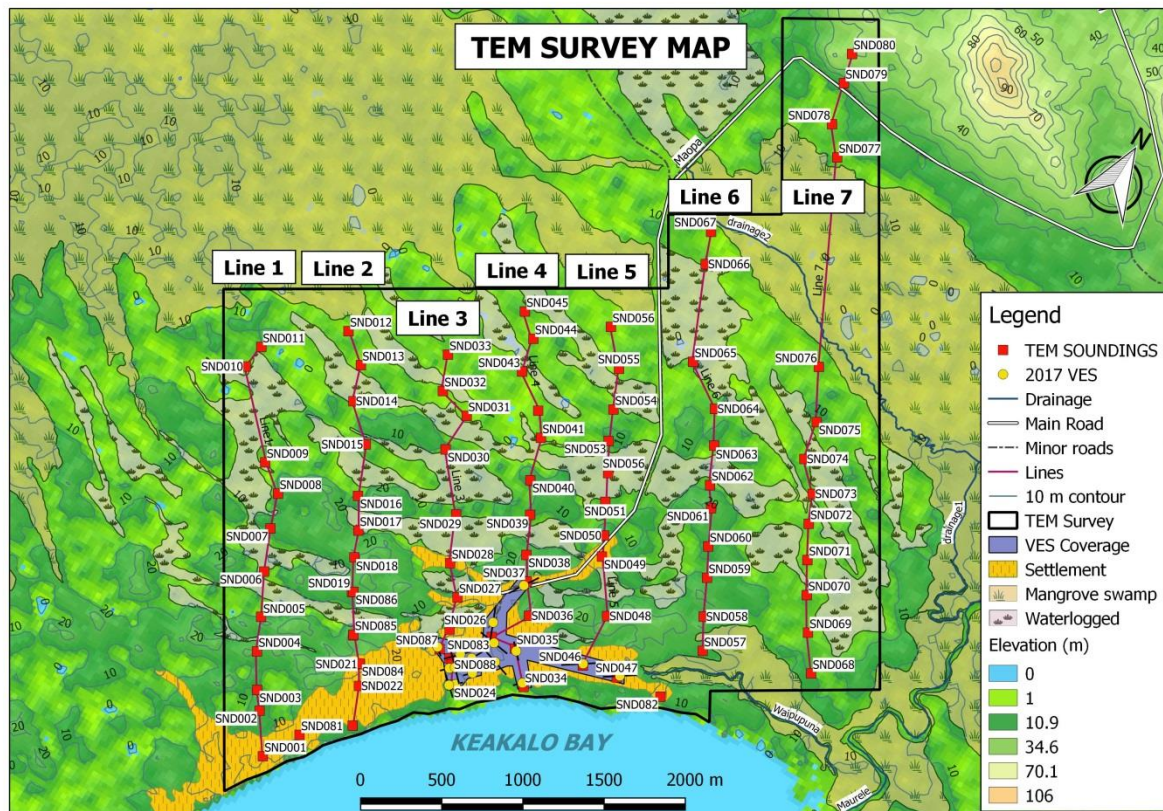


Figure 4.1 Map of TEM survey showing 88 TEM measurements and the locations of previous VES measurements.

The relatively easy setup of the TEM soundings enabled coverage of an area approximately 11.35 km² or 1135 hectares. It extended landward from Keakalo Bay in the south south-east through the marshy waterlogged interior and, for the most part, culminating right at the fringes of the mangrove swamp in the north north-west some 2 to 3 km inland. In two instances, the area extended beyond the mangrove swamps and at one point reached the western edge of the Coastal Highlands region. The width of the survey area span along the coastline is some 4 km in a north-east to south-west direction encapsulating most of the Moapa settlement and the interior marsh, which is surrounded by mangrove swamps.

Table 4-1 Sounding coordinates referenced to WGS84 UTM zone 55S.

#	L	Sounding	Easting	Northing	Elev.	Gate	#	L	Sounding	Easting	Nothing	Elev.	Gate
1	1	SND001	610749.0	8878397	2.5	20	48	5	SND048	610722.2	8881575	3	20
2	1	SND002	610586.7	8878627	2.5	20	49	5	SND049	612151.1	8879891	2.5	20
3	1	SND003	610509.1	8878729	2.5	20	50	5	SND050	612367.3	8879936	2.5	20
4	1	SND004	610385.4	8878931	2.5	20	51	5	SND051	612121.9	8880229	2.5	20
5	1	SND005	610297.4	8879128	2	20	52	5	SND052	611905.9	8880526	2.5	20
6	1	SND006	610170.3	8879376	2	20	53	5	SND053	611850.6	8880644	2	20
7	1	SND007	610066.3	8879623	2	20	54	5	SND054	611750.4	8880826	2	20
8	1	SND008	609920.6	8879831	2.5	20	55	5	SND055	611674.0	8880987	1.5	20
9	1	SND009	609829.2	8879955	2	20	56	5	SND056	611574.8	8881157	1.5	20
10	1	SND010	609422.7	8880399	1.5	20	57	5	SND057	611500.8	8881339	3	20
11	1	SND011	609442.9	8880552	1.5	20	58	5	SND058	611401.2	8881571	3	20
12	2	SND012	609853.3	8880911	1	20	59	5	SND059	611501.0	8881571	2.5	20
13	2	SND013	610026.4	8880772	1.5	20	60	6	SND060	611225.4	8881767	2	20
14	2	SND014	610101.4	8880558	1	20	61	6	SND061	612736.8	8880348	2	20
15	2	SND015	610304.0	8880369	1.5	20	62	6	SND062	612633.8	8880532	2	20
16	2	SND016	610426.1	8880072	2	20	63	6	SND063	612528.3	8880748	2.5	20
17	2	SND017	610537.5	8879891	2	20	64	6	SND064	612435.1	8880917	1.5	20
18	2	SND018	610602.2	8879738	2	30	65	6	SND065	612329.4	8881127	1	20
19	2	SND019	610698.5	8879547	2	20	66	6	SND066	612250.6	8881246	1.5	20
20	2	SND020	610843.2	8879322	3.5	20	67	6	SND067	611453.6	8882587	1.5	30
21	2	SND021	610969.8	8879191	3	20	68	7	SND068	613381.4	8880574	1.5	30
22	2	SND022	611033.0	8879073	3.5	20	69	7	SND069	613235.2	8880779	2	30
23	2	SND023	611133.1	8879073	2.5	20	70	7	SND070	613109.6	8880973	1.5	30
24	3	SND024	611126.5	8878844	1	20	71	7	SND071	613002.3	8881161	1.5	30
25	3	SND025	611521.2	8879373	5	20	72	7	SND072	612893.9	8881356	1.5	30
26	3	SND026	611521.2	8879273	2.5	20	73	7	SND073	612820.2	8881526	1.0	30
27	3	SND027	611470.0	8879506	2	20	74	7	SND074	612665.6	8881683	1.5	30
28	3	SND028	611333.5	8879658	2.5	20	75	7	SND075	612614	8881917	1.5	30
29	3	SND029	611272.9	8879853	2.5	20	76	7	SND076	612449.8	8882216	1.5	30
30	3	SND030	611126.0	8880010	2	20	77	7	SND077	611883	8883379	1.5	30
31	3	SND031	611026.0	8880010	1.5	20	78	7	SND078	611750.3	8883538	2	30
32	3	SND032	611276.0	8880010	1.5	20	79	7	SND079	611682.9	8883792	10	30
33	3	SND033	611003.9	8880286	1.5	20	80	7	SND080	611633.2	8883972	20	30
34	4	SND034	610541.0	8880895	1.5	20	81	R	SND081	610874.6	8878627	1.5	30
35	4	SND035	610453.6	8881103	3	20	82	R	SND082	612659.3	8879973	4	30
36	4	SND036	611708.6	8879983	2.5	20	83	R	SND083	611579.1	8879752	4.5	30
37	4	SND037	611738.8	8879765	2	20	84	2	SND084	610966.4	8879194	3	30
38	4	SND038	611708.6	8879983	2	20	85	2	SND085	610841.2	8879326	2.0	30
39	4	SND039	611589.0	8880156	2	20	86	2	SND086	610705.9	8879551	1.5	30
40	4	SND040	611401.9	8880295	2	20	87	R	SND087	611341.4	8879524	2.5	30
41	4	SND041	611501.9	8880295	2.5	20	88	R	SND088	611456.3	8879479	5.0	30
42	4	SND042	611394.8	8880519	2.5	20							
43	4	SND043	611286.1	8880702	1.5	20							
44	4	SND044	611207.4	8880959	2	20							
45	4	SND045	611107.1	8881094	1.5	20							
46	5	SND046	610898.0	8881249	7	20							
47	5	SND047	610853.7	8881458	6	20							

L=> lines; R=> Random measurements; Bold & Italic entries indicate soundings omitted from Inversion for various flaws

4.2 Sounding locations and lines

Soundings stations and their line groupings were numbered systematically following the chronological order of their execution. Coordinates of the soundings were determined by GPS measurements using “WGS84/UTM Zone 55S” as the coordinate referencing system which is provided in Table 4.1.

The number and position of soundings on each profile was entirely dictated by the challenging physiography. This meant the number of soundings per line as well as their measurement intervals were irregular. While smaller measurement intervals, resulting in higher measurement density per line, are ideal for better horizontal resolutions, for the purpose of this study a measurement interval of minima 100 m and maxima 500 m, with an average of 220 m and a range of 10 to 13 measurements per line, was sufficient along lines of lengths ranging between 2.1 and 3.9 km. Furthermore the objective of conceptualizing the 2D and possibly 3D lateral depth resistivity variations led to formulation of multiples lines adequately spaced (ranging between min distance of 460 m and 750 m at the max) but strategically aligned perpendicular to the coastline as outlined in Figure 4.1.

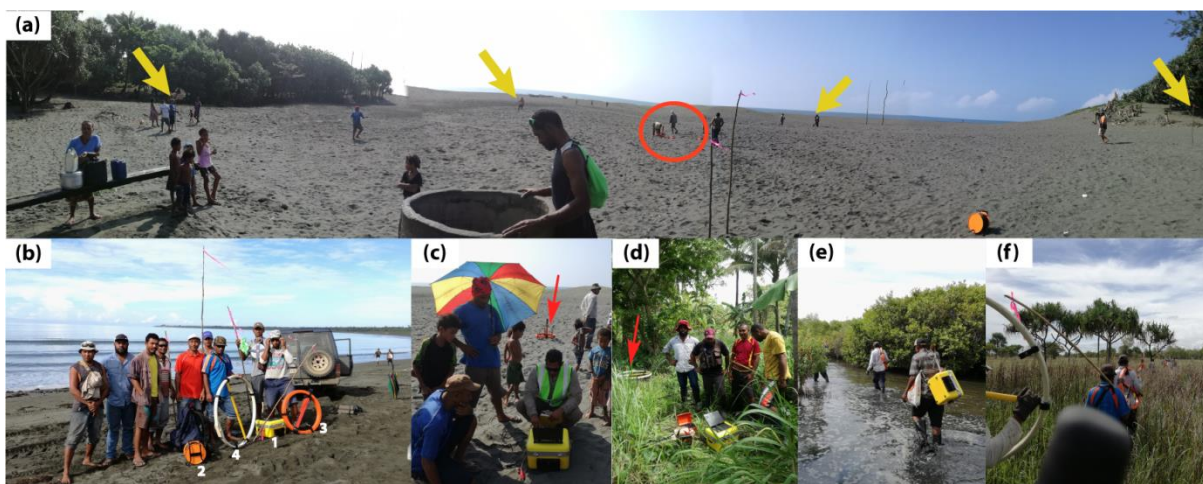


Figure 4.2 Examples of environmental conditions in the field set up. a) Laying out Transmitter loop and the central loop coil based on the central loop configuration. Yellow arrows denote the four corners of the transmitter loop while the central red circle shows the setting up of the High Frequency (HF) receiver coil; b) display of the main components of the TEM survey labelled as (1) PROTEM CM console; (2) 35 × 35 m transmitter current loop spool; (3) HF receiver coil; (4) Low frequency (LF) receiver coil; c) setting up survey parameters on PROTEM CM console with red arrow indicating HF receiver coil in background, which usually starts recording after the parameters have been set; d) showing measurements taken for the LF offset receiver coil which follow measurements at the central loop HF coil. The red arrow indicates the LF receiver coil connected to the PROTEM CM console; e) & f) examples of conditions encountered in the interior parts of the survey area, e) being a snapshot of mangrove swamp crossing during measurements at line 7 while f) shows navigating through thick grassland.

4.3 Field setup and measurements

A Geonics PROTEM CM instrument, on loan from the Mineral Resources Authority PNG, was used to conduct soundings. The instrument is a single or sequential three component (3D) time domain EM system and is one of Geonics newer models, which incorporates both the PROTEM receiver and the EM47 Transmitter all in one console. The system provides improved portability and convenience particularly suited to places like the current study area where it is environmentally demanding. Examples of environmental conditions are shown in Figure 4.2. Figure 4.3 shows the TEM sounding

setup used for the whole survey. This was based on the central loop TEM configuration. A transmitter loop dimension of 35 × 35 metres was laid out to target a current attenuation depth of approximately 150 m. Typical for the central loop configuration, two measurements or sweeps are required at a sounding station. The first is a measurement taken by the HF receiver coil at the centre of the transmitter loop, and the second one taken by the LF receiver coil outside the loop, or in this case 20 m from the transmitting loop wire, as depicted by Figure 4.3 a) and b) respectively and in the actual photo of layout in Figure 4.2 a), c), and d).

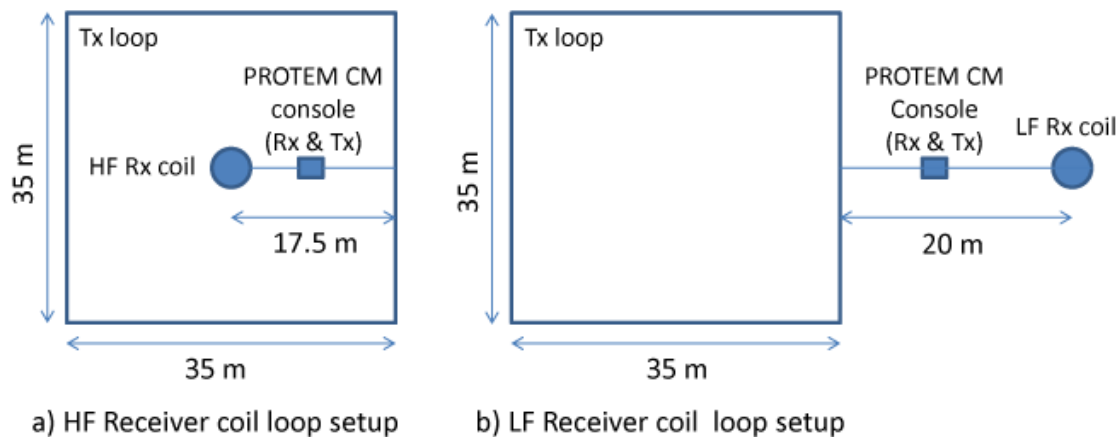


Figure 4.3 Survey loop configurations.

For the Instrument configurations, the loop current was set to 1 ampere (A) for measurements at the HF coil while 3.5 A was set for the LF coil measurements. The area of the HF coil was 31.4 m² pre-amplified and 100 m² for the LF coil. Once the proper gain levels were set, sounding for the first sweep (HF receiver coil) was carried out using a base frequency of 237.5 Hz. The second sweep (LF receiver coil) used a base frequency of 25 Hz. Turn off time was set to either 2.5 or 3 μs for the first sweep and 4 μs for the second sweep. Each measurement was made using an integration time of 4 s, which represents 8 repeats per soundings. Measurements at survey Lines 1-6 were taken using 20 gates (with a logarithmic measurement spacing) which are linked to the repetition rate or the base frequency (Fitterman & de Souza Filho, 2009). Measurements at Line 7 and additional random measurements were made using 30 gates and therefore the configuration slightly differed from earlier soundings taken with 20 gates (refer to Table 4.2 for details). Of the total of 88 sounding sites, a total of 176 measurements or soundings of both the HF (88) and LF (88) coil voltage-time curves were recorded over a period of 4 weeks (inclusive of days of delays).

Table 4-2 Survey Instrument configuration.

Survey parameters	20 gates		30 gates	
Sounding type	HF	LF	HF	LF
Repetition rate (base frequency in Hz)	237.5	25	25	2.5
Turn off time (micro second)	2.5/3	4	4	4
Integration time (second)	4	4	30	30

4.4 Data processing and inversion

The commonality of the use of Geonics TEM products among researchers meant that it is likely the data processing steps may have similarities although there are notable differences. For instance, Fitterman and de Souza Filho (2009) processed Geonics TEM data following a six-step process with a different choice of programs. In this work, processing of data involved four basic steps as outlined by

Figure 4.4: (1) data transfer; (2) qualitative analysis and averaging; (3) modelling; and (4) 1D profile generation.

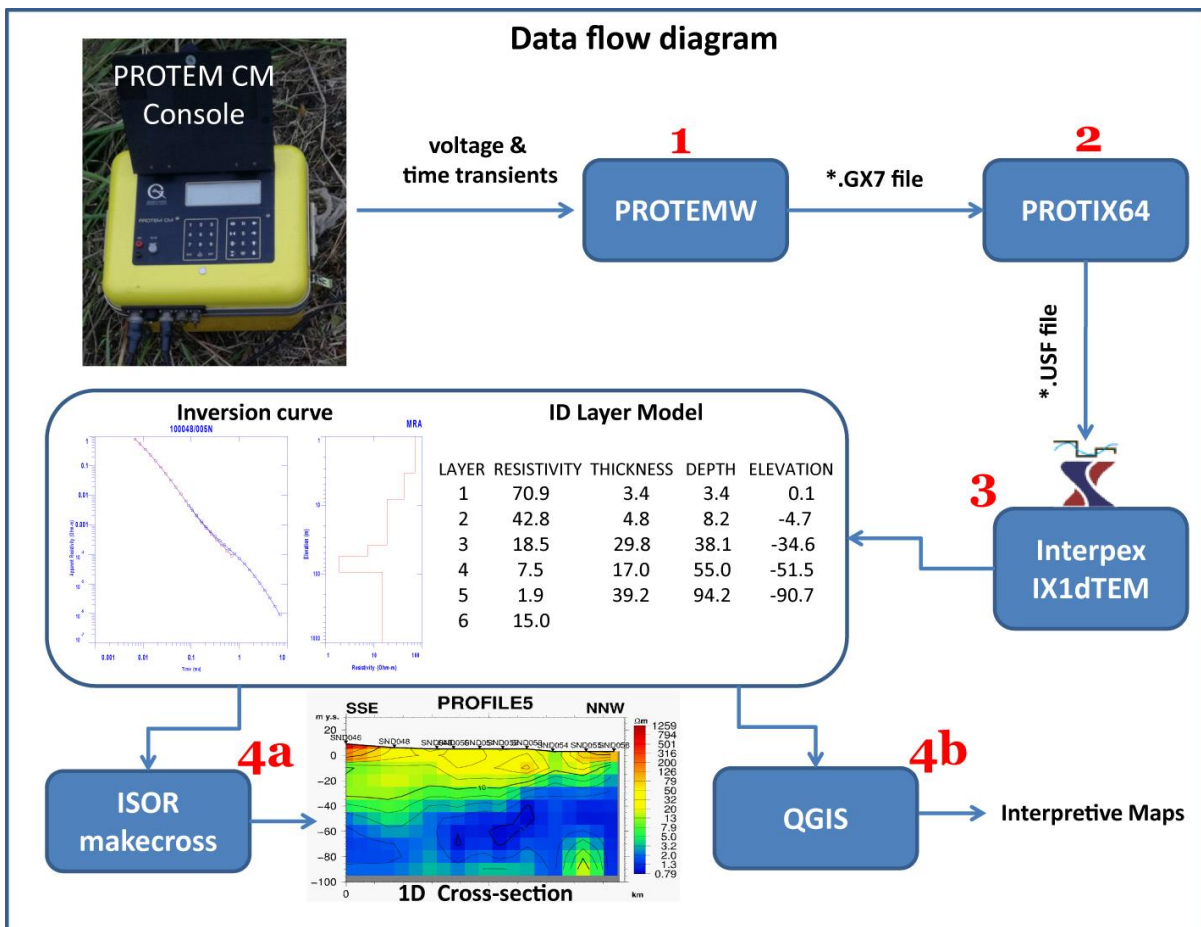


Figure 4.4 Maopa TEM data flow diagram with numbers indicating the four main stages of the process flow.

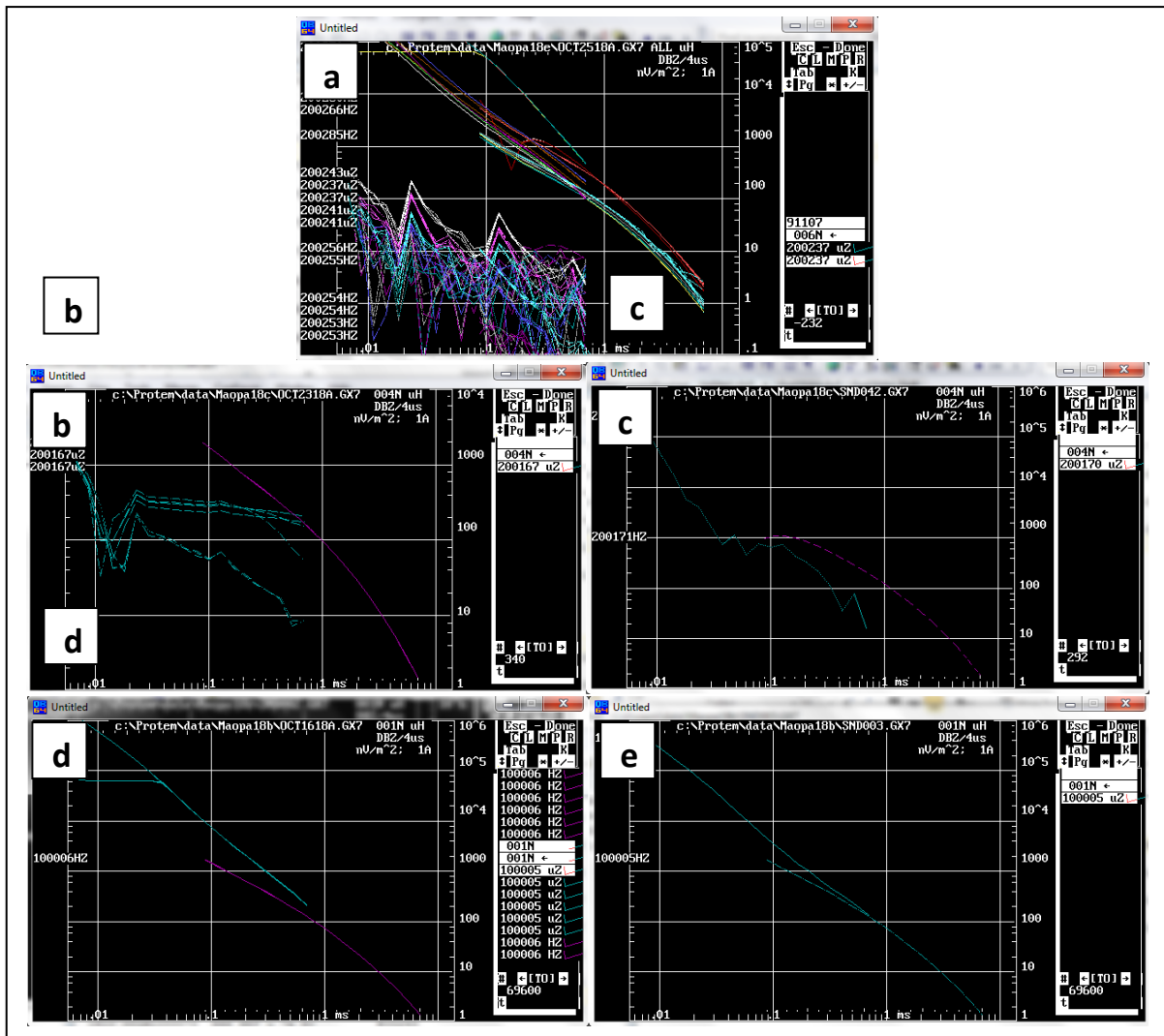


Figure 4.5 Graphical display of processing of a raw GX7 file in PROTEMW. On the y axis is the recorded voltage in nano Volts (nV) while the x axis shows time in milliseconds (ms) both scaled logarithmically. The panel to the right displays sounding information such as station number and frequency type. (a) display of the date stamp raw GX7 file (OCT2518A.GX7) showing the records of soundings taken on a particular day; (b) example of separation of sounding data per location showing improper amplification HF signal component with respect to the LF signal; (c) example of attempted correction of HF signals through manual gain normalization and averaging of the data from (b); (d) example of relatively clean and aligned signal components with signs of early time signal saturation presumable due to improper gain selection. (e) Corrected and averaged final data curve of (d) ready for extraction.

Transfer of data from the Geonics PROTEM CH receiver was made using PROTEMW one of three programs supplied by Geonics the manufacturer of the TEM instrument. The transfer of data was done each day soundings were made mainly to help ease sorting time and avoid mix-ups in grouping soundings per location or sweeps, which is a possibility in large multiple sounding surveys. Voltage

and time transients, in this case, are downloaded into a raw file named by default with date stamps by PROTEMW which is a routine for this particular Geonics model. The date stamp raw data file is in the format *.GX7 and typically contains all soundings of a particular day's measurements. Once the raw *.GX7 files are downloaded, soundings of choice, presumably those collected first, are loaded onto the PROTIX64 program for quality analysis and averaging. Because the raw GX7 file contains multiple sounding and they are usually huge and tedious to work with, mixing up individual sounding records per their location and sweep is kept minimal by matching field notebook records against sounding records of the GX7 files.

Figure 4.5 (a) shows an example of a multiple sounding record of a GX7 file. Individual sounding records are subsequently extracted from the main raw GX7 files either through the PROTIX64 program or any text editing program as a small GX7 file so that they can be analysed by sounding location. Normal workload at this stage can be straightforward with averaging and extraction of the file which depends mostly on data quality. In this case, poor data quality, which were mainly observed in HF data of the first four lines, increased workload beyond just averaging (Figure 4.5 b). Improper amplification of the HF signal together with records of signal saturation and polarity reversal were the main issues associated with the poor quality data in this study. Improper amplification of HF data was normalized by the gain factor (2^2) in an attempt to achieve a proper alignment with LF data. Signal saturation data (Figure 4.5 d) were omitted and the polarity reversal corrected using the EDIT SCREEN functionality of PROTIX64. Finally, averaging was done for both the HF and LF data, which were then combined as one sweep per sounding location and converted into a single USF file format, which can be read by the commercially available inversion program INTERPEX IX1D v3.

TEM inversion techniques are described in detail by Newman et al. (1987) and Farquharson and Oldenburg (1993), while Constable et al. (1987) specifically describe an algorithm for Occam's inversion which produces the minimally layered and smoothest model that can fit the data to a specified level. Generally, the idea of inversion is to invert apparent resistivity as a function of time into actual resistivity as a function of depth by finding a calculated model that best fits the measured data with a minimal difference or least square value. Even though this may be convincing, the issue of non-uniqueness is still relevant and requires caution and the need to consider constraints or educated guesses. To invert the USF file containing voltage time transients to 1D resistivity curves and depth models, USF files were imported into the IX1D v3 program. The IX1D v3 program performs forward and inverse modelling for 1D layer models, equivalence analysis and automated estimation of layered and smooth models or Occam's inversion (IX1D v 3.60., 2019). Examples of such

inversions are shown in Figure 4.6 with more detailed information presented in Appendix 1. Upon loading of the USF files, GPS coordinates and elevations of the sounding locations were given and then the USF files were plotted as apparent resistivity as a function of time on a log-log scale. Both forward and inverse modelling were used interchangeably by first setting up an initial smooth model parameters such as the starting number of layers, minimum and maximum depth, and the starting resistivity. Once a satisfactory initial smooth model was established the layered earth model was then introduced and configured as the smooth model and later inverted iteratively. The outcome of the initial model and the quality of the data determined the frequency of the application of the two modelling techniques used here. Forward modelling with the guidance of the smooth model, in this case, was used intensively on noisy data, particular those from the HF component of soundings in Lines 1-4, but was also used to fix unrealistic models from other soundings. During inversion, outlier and distorted data points were masked. Comparison of models from nearby soundings, and alteration of layer number and thickness helped to improve the curve fit. Unresolvable layers such as very thin layers and sequence of layers that have significantly similar resistivity were omitted from the model. The final inversion models result best describing a sounding generally had 4 to 6 layers with a relatively low resistivity/conductive bottom layer.

The final stage of processing involves two sub-steps: generating resistivity cross-sections and spatial interpretive iso-maps. In the first, 1D resistivity depth models grouped by lines are imported into “make cross” a program developed by ISOR (Iceland GeoSurvey) to produce 2D cross-sections. The program interpolates 1D resistivity depth models – specifically resistivity values and their corresponding thickness – beneath each sounding location along a line with the resistivity colour scaled and contoured. The inaccuracy of this program is illustrated by its inability to accurately interpolate resistivity layer thickness obtained in this study, which are much smaller than the program is designed for (depths of up to 20 km). The other step uses a master file containing the same 1D modelled data but arranged differently in Quantum Geographic Information System (QGIS) to create spatially interpretive iso-maps. QGIS is a free and open source software that as well as creating and exporting visualized maps, also provides analysis, editing and visualisation of geospatial data. Spatial interpretive iso-maps were produced by using the Natural Neighbour Interpolation technique. In addition, depth profiles of modelled layers superimposed on the cross-sections shown in the results section evolved from gridded spatial layer elevation data through the “Terrain Profile” plugin of QGIS. The plugin uses each survey line placed on top of the grid to draw out corresponding depth profile by layers.

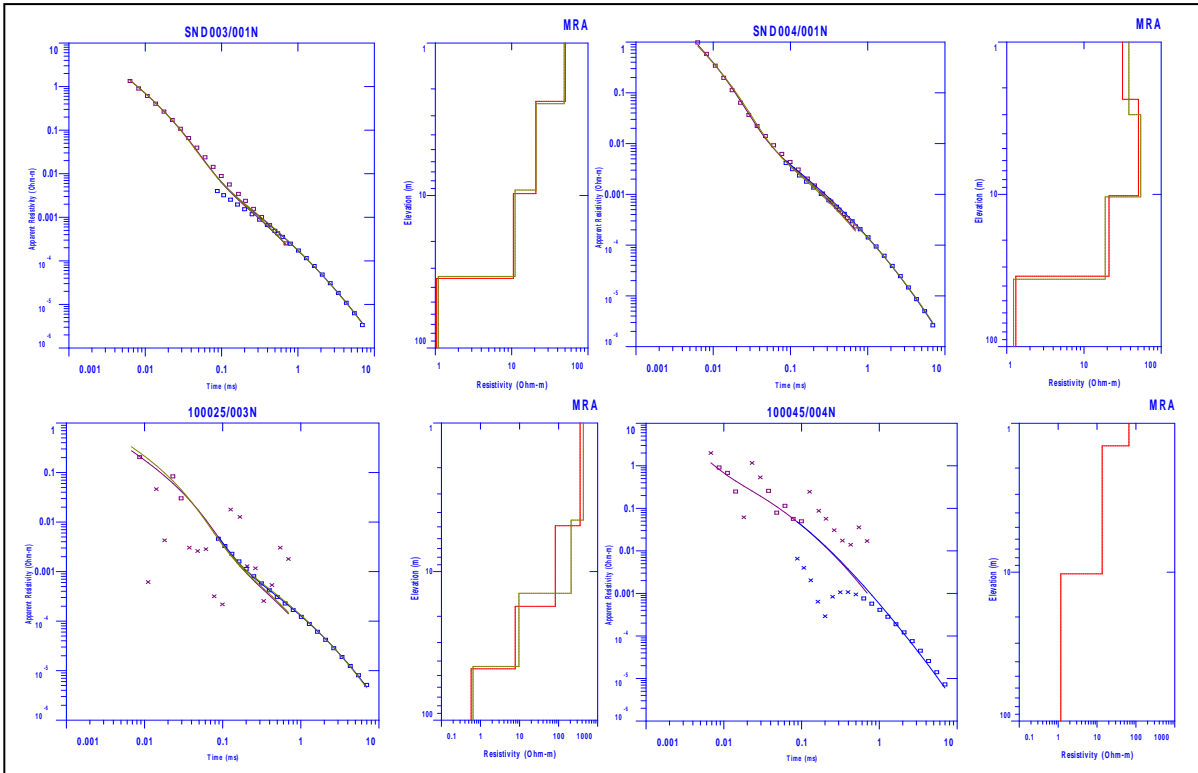


Figure 4.6 Examples of Inverted data. On the left is a graph of apparent resistivity (Ωm) vs time (ms) with red and blue squares indicating measured high frequency and low-frequency data, respectively. The red and brown Lines on the graph denote calculated and Occam's estimated smooth models, respectively. At the centre is the depth model showing depth vs calculated resistivity (red line) and the estimated smooth model (brown line).

Chapter 5 Results, discussion and interpretation

5.1 Resistivity cross-sections

In an attempt to assess the lateral and vertical extent of salination and the characterization of groundwater in the landward direction, 1D resistivity models along a series of Lines (Figure 5.1) were used to generate resistivity cross-sections. These cross-sections show a vertical and lateral view of the inferred subsurface resistivity, which is colour_scaled and contoured. Furthermore, to give a perspective of how the main modelled layers sit within the Interpolated cross-section, information obtained from the resistivity models and stored in a master file (refer to Appendix 2) was used in QGIS to generate actual layer profiles shown by the superimposed red lines. Out of the 88 TEM soundings, 76 were considered reliable and therefore used collectively to create seven cross-sections presented below. As is customary with inversion of geophysical data, results of 1D inversion of TEM data used in these cross-sections are subject to the problem of non-uniqueness of the resistivity models. Model constraints were mainly based on local knowledge of the surface geology and observation of hand dug wells, meaning the presentation of results here are merely one of many possibilities leaving room for debate. The final apparent resistivity curves and 1D models for each site are shown in Appendix 2.

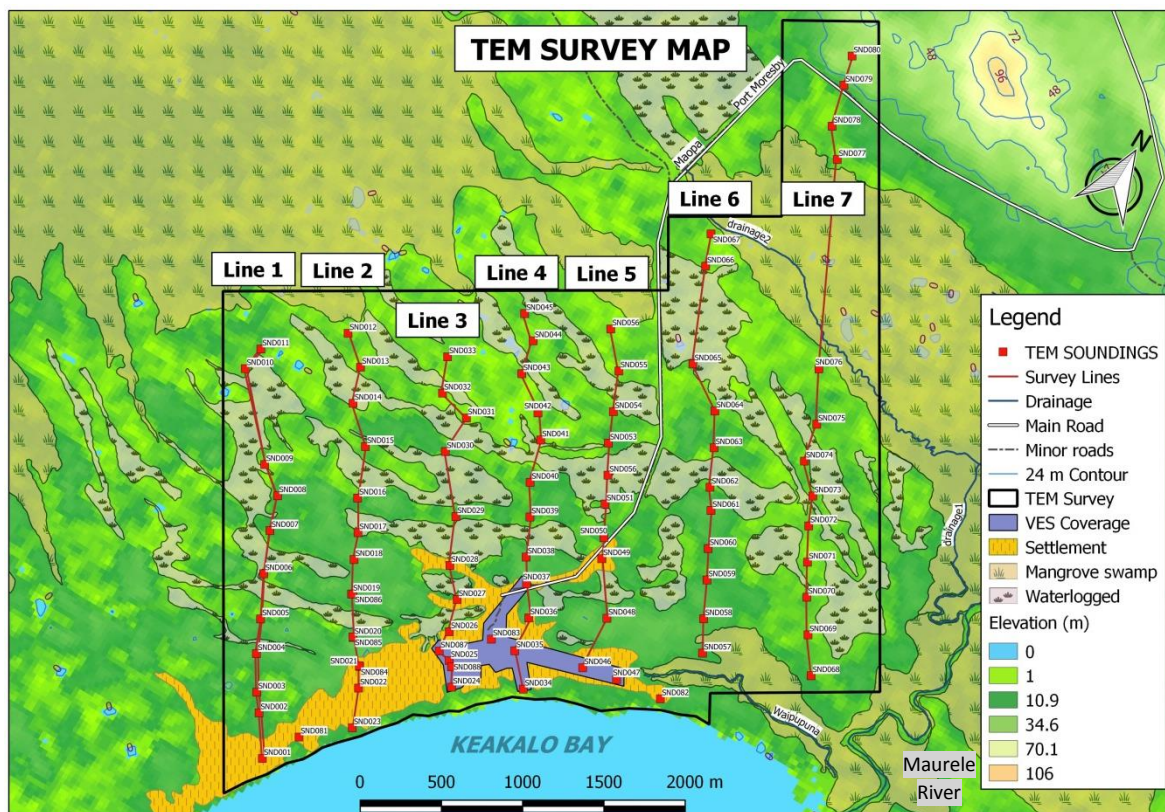


Figure 5.1 TEM survey map showing locations of lines/profiles with their respective TEM soundings.

5.1.1 Profile 1

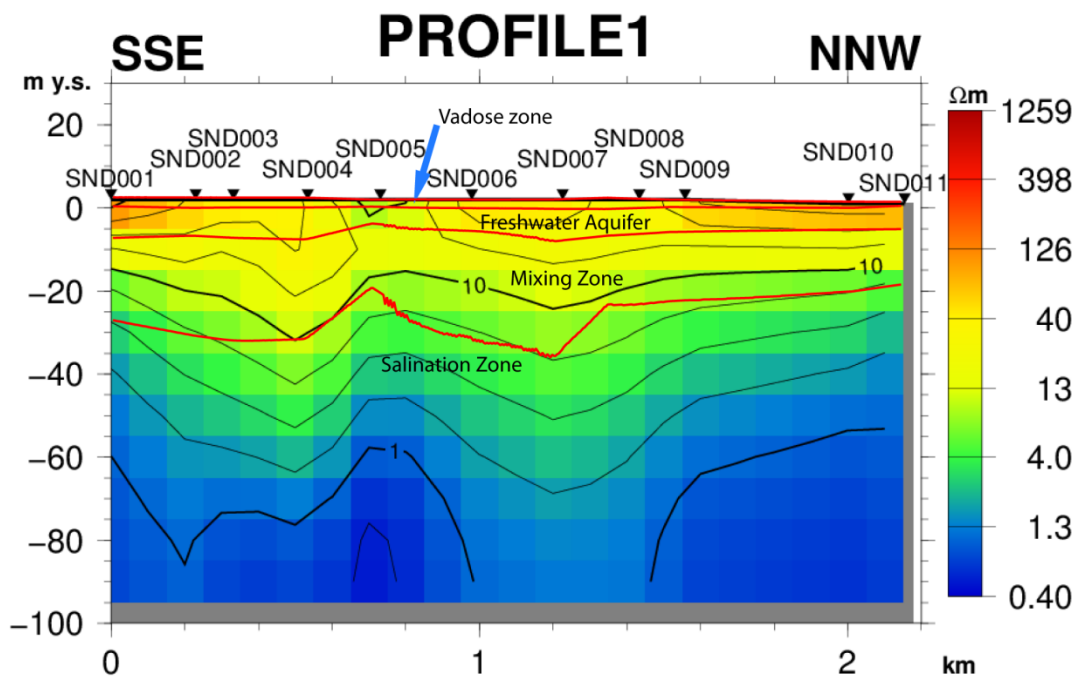


Figure 5.2 Resistivity Cross-Section Profile 1 shows the Interpolation of 1D resistivity models of 11 TDEM soundings from Line 1 located on the western flank of the study area (Figure 5.1). Red lines denote the inferred top of the modelled layers.

Soundings here were modelled by four layers as indicated by the red lines in Figure 5.2, showing an apparent gradual decrease in resistivity with depth. The discrepancy between the superimposed lines and the resistivity interpolation between adjacent soundings, particularly at depth, is a result of inaccuracy of the interpolation program (makecross) described in Chapter 4. The top layer has an average resistivity of 52 Ωm with a range from 4.6 to 130 Ωm and an average thickness of 2.1 m. The highest resistivity values, observed beneath SND001 at the SSE end of the profile, are attributed to dry ironsand dunes widely found near the coast. Lower resistivity elsewhere is reflective of the silt and loam affluent regions occupied by seasonal wetlands. This layer is the vadose layer whose thickness is dependent mainly on the surface elevation, which is mostly near sea-level. The second layer has a resistivity averaging about 40 Ωm with a range of 21 to 72 Ωm and occurs at a depth of 2.1 m that varied between 1 to 2.3 m. Its thickness is relatively constant (ranging between 4.2 to 8.2 m) and averages about 6.6 m. This layer is considered the freshwater aquifer with soil constituents of coarse sand and marine fragment mixture with some silt and loam. Below the freshwater layer is a layer which most probably represents the zone of dispersion or mixing zone. This layer has an average resistivity of 11 Ωm with a range between 6.2 and 21 Ωm . Depths to this layer ranges between 5.8 and 10.5 m with an average of 8.5 m. The layer is shallow at both ends of the line and generally extends deeper in the middle. The lowermost layer is at a depth of 29 m and has the lowest resistivity varying from 0.7 to 1.6 Ωm . The depth varies from lowest near the coast and the

NNW end of the line with an anomalously shallow depth observed in the middle of the line beneath SND005. This stratum most likely is the saline zone. The anomalously high conductivity (low resistivity) noticed beneath SND005, appearing as an upwelling of the saline zone, may be a 3D artefact of 1D inversion (Goldman et al., 1994), but a more practical explanation of this is surface seawater infiltration from advancing mangrove forest adjacent to the central part of the Line.

5.1.2 Profile 2

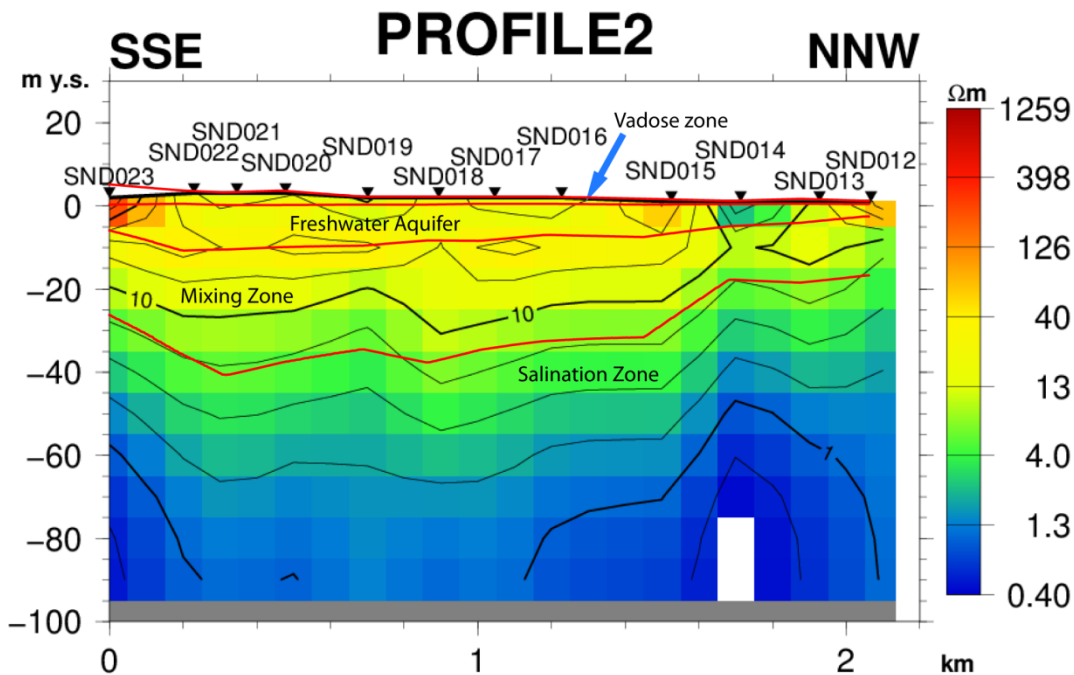


Figure 5.3 Resistivity Cross-section Profile 2 shows Interpolation of 12 Soundings from Line 2.

Figure 5.3 is similar to Figure 5.2 with soundings modelling 4 layers. Notable features are that layer resistivities are homogenous and decrease gradually with depth. There is also a 3d inversion artefact, as observed earlier, under SND0014. The sounding SND014 was taken in an area known to be inundated by meteoric waters thus the feature is likely caused by high levels of siltation with some possibility of surface infiltration of seawater from the interior during extreme tidal events. A discontinuity in the 1 Ωm contour, observed mostly under soundings located toward the coast, is a result of modelling resistivity values of the saline zone greater than 1 Ωm but less than 3 Ωm.

The vadose zone here has a maximum thickness of 3.5 m observed near the SSE end of the line. The thickness gradually decreases to a low of 0.8 m under soundings at the NNW end of the line. Resistivity for this layer averaged about 53 Ωm and varied between 1.2 and 365 Ωm. The trend of resistivity distribution is entirely consistent with observations of the previous line, where higher values were found near sandy areas. The freshwater aquifer has resistivity (average of 42 Ωm) similar to Line 1 and ranged between 18.7 and 66 Ωm. Aquifer thickness at its highest is about 11 m

generally observed beneath SND019 to SND022. A gradual decrease in thickness begins from SND018 toward the end of the line where 2.9 m is recorded under SND0012. SND023 near the coast also recorded a similar reduction in thickness. The zone of mixing has lower resistivity than the freshwater zone with values up to 13.3 Ωm while thickness reached a maximum of 30.4 m below SND021. The mixing zone is shallow at the soundings located at both ends of the line with the lowest depth of 3.7 m under SND012. Greater depths to this layer are consistent among soundings in the interior of the line mostly towards the SSE. The last layer, interpreted as the saline zone, shows some symmetry to hydrological models of small islands. Depths to this layer reach an average of 33 m with a maximum of 44 m observed beneath sounding SND022 and a minimum depth of 17.9 m at sounding SND0017 on the NNW side of the line. Resistivity ranges from 0.4 to 1.5 Ωm .

5.1.3 Profile 3

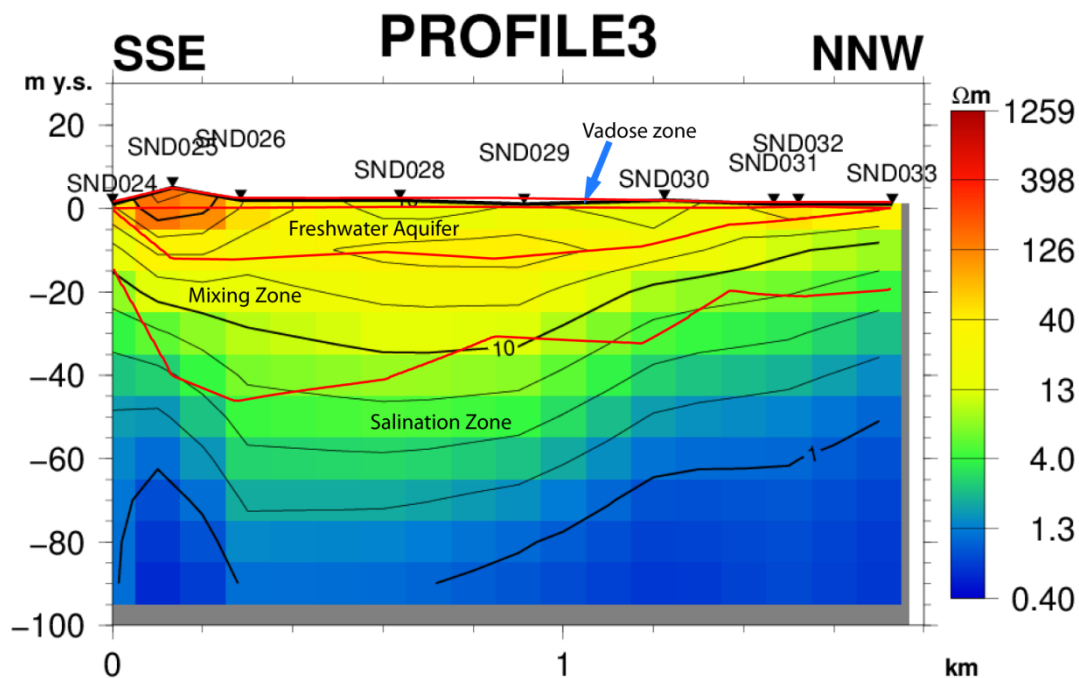


Figure 5.4 Resistivity Cross-section Profile 3, shows Interpolation of 9 Soundings from line 3.

The main feature of Figure 5.4 is the observance of the mixing zone at shallow depths, usually occupied by the freshwater aquifer, beneath SND024 and SND033 at both ends of the line. These soundings are modelled by three layers, and resistivity values of 16.3 and 7.2 Ωm , respectively, at a shallow depth. The shallow depth is primarily due to the near-surface very conductive (very low resistivity) subsurface medium. These values correlate well with a slightly saline communal well located a few metres from SND024 and with surface seawater infiltration from the inland mangrove swamps indicating the shallow outer bounds of the mixing zone. Also notable is the manner of the change in depth of this layer from its deepest points to both ends of the line. This change is gradual to the NNW end whereas it is much steeper to the SSE end. Elsewhere, as on the previous lines, the

highly variable vadose layer resistivity ranged between 6.7 and 356 Ωm . Higher resistivity values are exhibited in high sandy areas, whereas relatively lower values observed elsewhere relate to the silt-rich wetlands. The freshwater aquifer has a uniformly distributed resistivity with an average of 47 Ωm and a range from 27 to 82 Ωm . The thickness of the aquifer is greater on the SSE side of the line with modelled values of up to 12.5 m, which is notably higher than the two previous lines. The layer of dispersion is generally thicker at similar locations to the freshwater zone and occurs at depths of up to 17 m. This layer replaces the freshwater region at the fringes of the line and has an average resistivity of about 10.6 Ωm from a range of 6.5 to 13.3 Ωm . The saline zone is observed right across the profile having resistivity values ranging between 0.6 and 1.5 Ωm and a maximum depth of about 49 m.

5.1.4 Profile 4

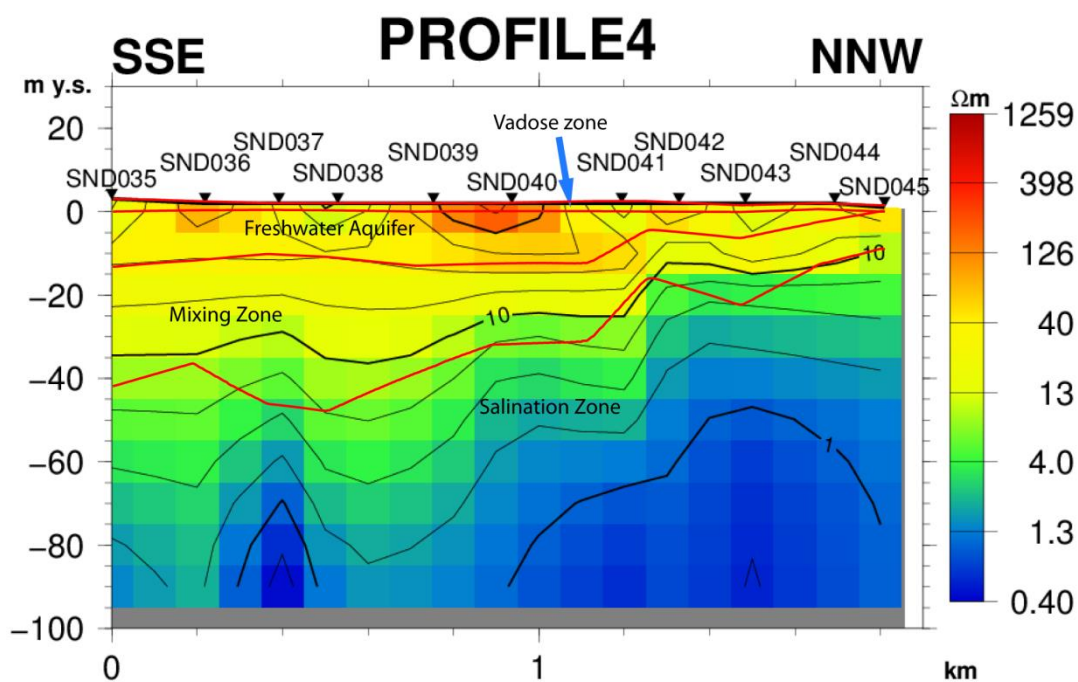


Figure 5.5 Resistivity Cross-section Profile 4 shows Interpolation of 11 Soundings from line 4.

Figure 5.5 also shows the 1 Ωm contour discontinuity in the deep saline zone mostly under the SSE (seaward) end of the line and a significant decrease in layer depths towards the NNW end of the line. The main feature of this profile is the symmetry of the three bottom layers taking a generally concave shape. Here the depths to mixing zone and the saline zone at all soundings gradually decrease towards the NNW end of the line where mangrove forests dominate allowing surface intrusion of seawater. It is observed that at sounding SND045 the mixing zone has intruded and replaced the probable freshwater zone at shallow depth. At this point three geoelectric layers were modelled compared to four modelled elsewhere on the line. There is no upward trend of the contrasting resistivity layers, especially of the dispersion zone and the saline zone, at the seaward

end of the line. This is a result of the lack of soundings close to the coast - by sounding SND034, which was aimed to capture the shallow mixing zone, but could not be used due to poor data quality. However VES model VES08 from the previous study by Verave (2018) at this location supports the shallow detection of the mixing zone at 6.8 m with a resistivity of 14 Ωm occurring beneath a freshwater zone of thickness 5.3 m and a resistivity of 30 Ωm .

Aside from this, the four major layers persist in this line, which is the last of the four Lines (1, 2, 3 and 4) plagued by noisy HF data (early time data). The poor early time data is the main cause of the highly variable resistivity values modelled for the vadose zone. In this line resistivity values for the top layer (vadose) ranged from 4.3 to 258 Ωm and averaged around 70 Ωm . High values observed on the coastal side of the line are easily inferred as caused by the typically elevated dry sandy environment while higher values elsewhere are a result of poor resolution mostly of this layer. The freshwater zone has an average resistivity of 40 Ωm varying between 32 and 69 Ωm and has a thickness of up to 13.2 m. Higher thicknesses were observed for the most part of the line except for the last four soundings on the NNW side of the line. The mixing zone has similar layer geometry except it is much thicker at thickness up to 36 m and occurs at a depth of about 16 m. The layer resistivity varies between 8.3 and 15.2 Ωm . The saline zone occurs at depths of almost 50 m beneath SND038 and has a resistivity range of 0.5 to 2.6 Ωm .

5.1.5 Profile 5

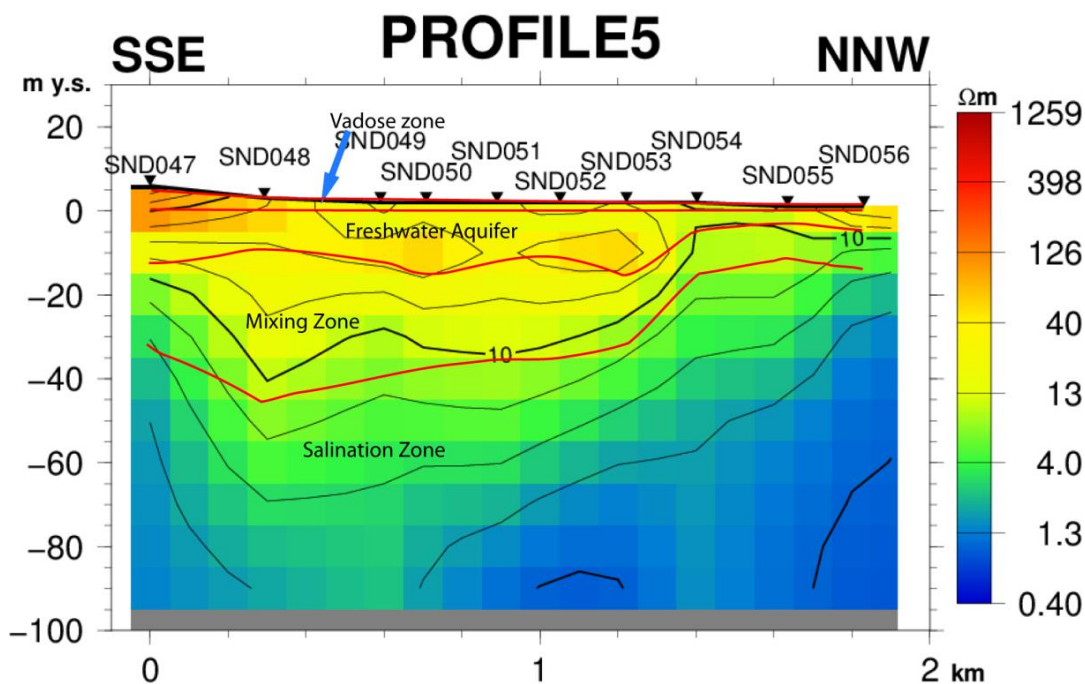


Figure 5.6 Resistivity Cross-section Profile 5 shows Interpolation of 10 Soundings of line 5.

Figure 5.6 shows some resemblance to Figure 5.5. Firstly, the discontinuity of the 1 Ωm resistivity contour that indicates modelling of resistivity values greater than 1 but less than 3 Ωm is observed, together with the continuity of the saline zone across the line taking a concave shape. Second is the subdued uptrend of the mixing zone and saline zone at the SSE end of the line, although resistivity patterns indicate a slight upward trend. Also similar is the observance of a more distinct display of symmetry of layers although less prominent on the seaward end of the line.

Four layers were modelled in this line (Profile 5), which is one of three lines dissecting the central part of the survey area. Here the top most layer interpreted as the vadose zone is observed to be thicker (6.6 m) at the start of the line (SSE) indicated by the elevated surface relief that corresponds to iron sand deposits. Lines that dissect the iron sand usually show higher resistivity values, in this line 452 Ωm is observed. Lower resistivity values of this layer are noted elsewhere on the line, especially in silt and loam deposits. The layer of freshwater occurs at an average depth of almost 3 m, which is consistent with the observation of hand-dug wells in the area. The variation of the depth to water table observed in the area is not uncommon given that topography dictates these changes. The range of depth (1.5 - 6.6 m) supports this assertion. The layer thickness averages about 10 m but can reach a maximum of 15 m in the middle of the line. Lower aquifer thickness is expected at the end of the line. Resistivity of the freshwater layer is less varied, averaging about 47 Ωm over a modest range of 33 to almost 60 Ωm . The resistivity range most probably corresponds to saturated coarse sand mixed with marine fragments (shell and coral rubbles) widely observed in digging sites. The next layer is conductive (low resistivity) and is detected at an average depth of about 12.7 m with a resistivity ranging from 4.5 to 16.9 Ωm and an average of 11.1 Ωm . The resistivity of this layer is relatively uniform along the middle section of the line, however at both ends of the line the lowest values are observed beneath SND047 and SND056. While the layer is considered the mixing zone where freshwater and seawater are dispersed, the varied resistivity values are most likely due to greater interaction with the saline zone in the near surface at these two soundings. The mixing zone appears thicker on the SSE side of the line reaching up 36.6 m and thins out toward the ends of the line. It is significantly reduced in thickness on the NNW with a minimum of 8.4 m. The lowermost layer interpreted as the saline zone persists right through the line. Its resistivity values ranged from 1 to 2.7 Ωm and averages of about 1.7 Ωm , which is relatively higher than observed on previous lines. The average depth is about 23 m and varies between 1.2 and 63 m. The depth trend is consistent with depths usually greater in the central part of the line and shallowing out at the ends, more so on the NNW side.

5.1.6 Profile 6

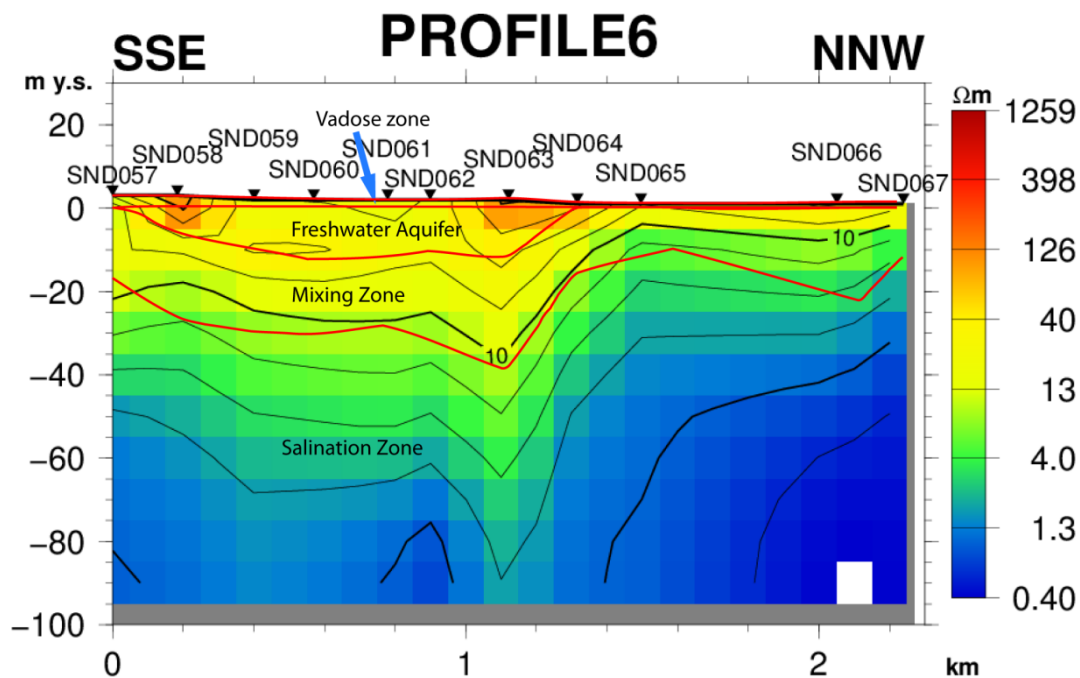


Figure 5.7 Resistivity Cross-section Profile 6 shows interpolation of 11 soundings along line 6 stretching more than 2 km. The gap between SND065 and SND066 is an area occupied by one of the largest water bodies in the area.

Profile 6 in Figure 5.7 is one of the two longer lines that run through water bodies, thus leaving a section with no information. Up to the line distance of about 1 to 1.5 km, comparable to the length of previous profiles, the resistivity distribution is consistent with other lines. Here the resistivity is uniform apart from two high resistivity patches mainly modelled in the top layer and obscuring the resistivity of the underlying layer. Resistivity values greater than 1 but less than 3 Ωm continue to be observed, creating an illusion of discontinuity of the very conductive bottom layer and some points in the freshwater layer vanish.

In this profile 3 to 4 layers were modelled based on the general observation of the topography, vegetation and location of water bodies with respect to soundings. The line runs through low and flat topography of silt and loam-rich areas with some farming patches and water bodies. The thin (range from 0.9 to 2.7 m) vadose layer, usually with the most variable resistivity, seems modest with a low average value of 45 Ωm although two anomalously high regions are noted at SND058 and SND063. The exact cause of these could not be verified but it is speculated that the high resistivity anomaly at SND058 may be caused by running the Tx loop through a metal fencing. Conversely, at SND063 high resistivity may be due to gravel deposits given that the line is close to the main Maurele River and higher values of the resistivity are obtained for the underlying layer. The underlying layer is of intermediate resistivity averaging about 38 Ωm, which is representative of the

layer of fresh water. The layer has a modest range (26 to 56 Ωm) indicating a relatively homogenous layer of coarse sand and marine fragments mixed with some silt in areas showing lower resistivity values. The fresh water exists at a relatively shallow depth (range of 1.6 - 2.4 m) with sufficient thickness (4.2 to 8.2 m) observed for most at the centre of the line toward the sea. This layer vanishes at the start of the line under SND057 and for the most part of the NNW side of the line from SND064 through to SND067. These latter three soundings modelled three layers. The next layer has a generally lower resistivity than the preceding layer, averaging about 11.6 Ωm , but notable variability with a range of 5.3 to 18.3 Ωm . Greater values concentrate under the fresh water layer, while the lowest values are apparent at shallow depth where the freshwater layer is absent. The layer is reflective of the zone of mixing and occurs at an average depth of 8.2 m and with a range between 0.9 and 14.8 m. It is deep under the freshwater layer and reaches 0.9 m at its shallowest. The saline zone is again observed right through the line reaching much shallower depths on the NNW side of the line than at the seaward end. The salination resistivity averages about 1.2 Ωm and occurs at greater depths (42.4 m) in the middle of the line. Shallow depths can be observed at the interior water-body and mangrove forest and the coast.

5.1.7 Profile 7

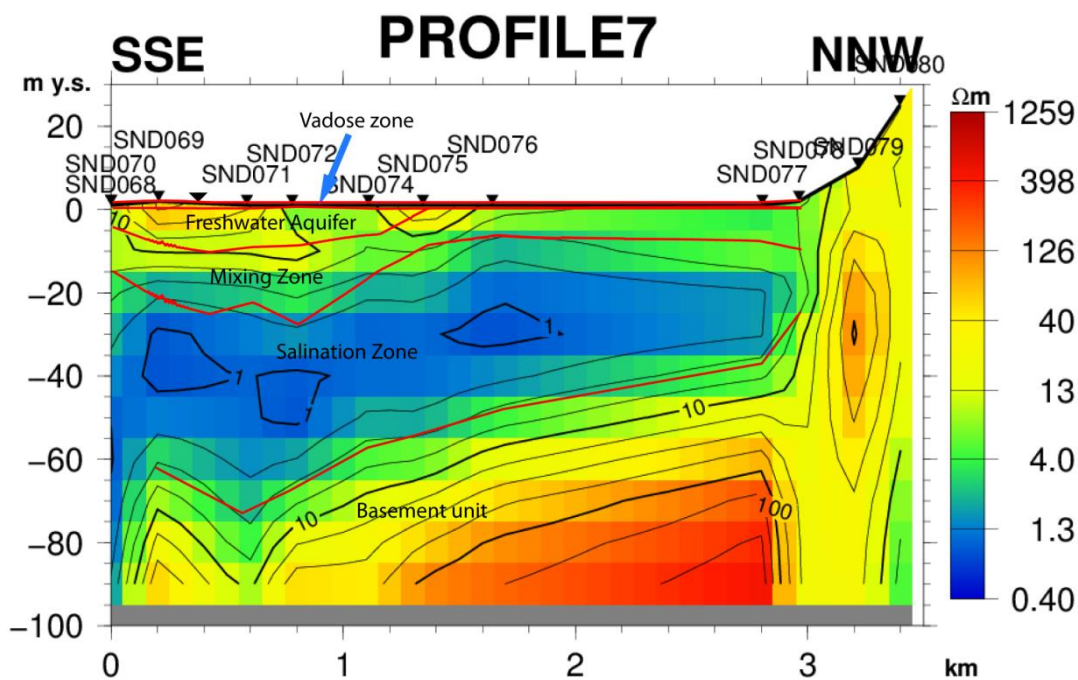


Figure 5.8 Resistivity Cross-section Profile 7 is made up of interpolation of 11 soundings from line 7 making up the longest line of the survey stretching 3.4 km inland. This line runs right through the mangrove swamp indicated by the void in sounding stations and terminates in the Coastal Highlands region.

The Figure 5.8 show Profile 7 with a very contrasting display of resistivity compared to that observed so far. The detection of a deep resistive layer is the main feature, and this is well resolved by most

soundings on this line. Soundings were measured using 30 gates (logarithmic measurement spacing) configuration, enabling diffusion of EM fields and therefore circular currents to reach depths beyond the very conductive zone.

The numbers of layers modelled for this line were between the usual 4 and 5, differentiated only by the absence of the deep layer at SND068 at the start of the line and areas, mostly observed on the NNW side of the line, void of the freshwater layer. The layer of aeration, or the vadose zone, most surprisingly has low resistivity values averaging about 20 Ωm , comparable to resistivity values of both the fresh water layer and the mixing zone. Because the line is very close to an almost encapsulating extensive mangrove swamp and the Maurele River, the likelihood of resistivity reduction for the top layer by these features is probably by the combination of high silt level deposition and surface seawater intrusion during extreme natural events. A slightly higher resistivity average (28 Ωm) than the top layer is seen for the freshwater layer. The resistivity is intermediate and has a range of 21 and 39 Ωm uniformly spread across the soundings that detected it. This layer is obviously absent from SND 075 through to SND080 and occurs at a typical depth of 1.5 m (average) consistent with observations of hand dug wells in this area. Freshwater aquifer thickness are observed to be thicker at about 10.8 m in the central portions of the line, which has similarities to Line 1 and Line 2, but is generally thinner than in most of the central lines. The mixing zone layer has a much lower resistivity average (5.9 Ωm) than the fresh water aquifer and, apart from two soundings giving resistivity values of 16.1 Ωm , most soundings recorded similar values to the average. The uniform low resistivity observation may be attributed to the relative alignment of measurements with respect to shallow conductive sources emanating from a nearby mangrove swamp. TDEM measurements aligned along with a conductive target generally yield little contrast in resistivity as in this case, confirming the layer is influenced by the surrounding mangrove swamp. The mixing layer reaches a depth of up to 12.3 m between SND070 and SND072 while at the flanks it is shallower. The saline zone is prominent right through the line terminating at the Early Miocene to Late Pliocene-raised Kupiano Beds. This layer is very conductive (range between 0.8 and 1.5 Ωm) and is found at depths of up to 30 m between the mixing zone and a deeper more resistive layer. Salination also occurs at shallow depths (min 8 m) around the mangrove swamp and near the coast. The most unique aspect of this line is the modelling of a basement layer, which provides essential information about the thickness of the overlying young unconsolidated sediment. This layer corresponds to buried parts of the Kupiano Beds which form the nearby Coastal Highlands region. It is situated at an average depth of 64 m with depths gradually decreasing from 79.5 m at the SSE end of the line to 34 m at the NNW end. The basement unit has typically high resistivity with an average of 93 Ωm and a range of 34 to 289 Ωm . Higher resistivity values may be poorly resolved at greater

depth given the high conductive shallow environment and the inherent lack of better resolution of higher resistivity by the TDEM method. However, the discovery of the basal layer by soundings SND085 and SND086 (Figure 5.9), subsequently taken on Line 2 using the same survey parameters to Line 7, supports the model. The inferred basal layer is seen detected at about 77 m on both soundings with similar resistivity of 31 and 44 Ωm , which are consistent with line 7.

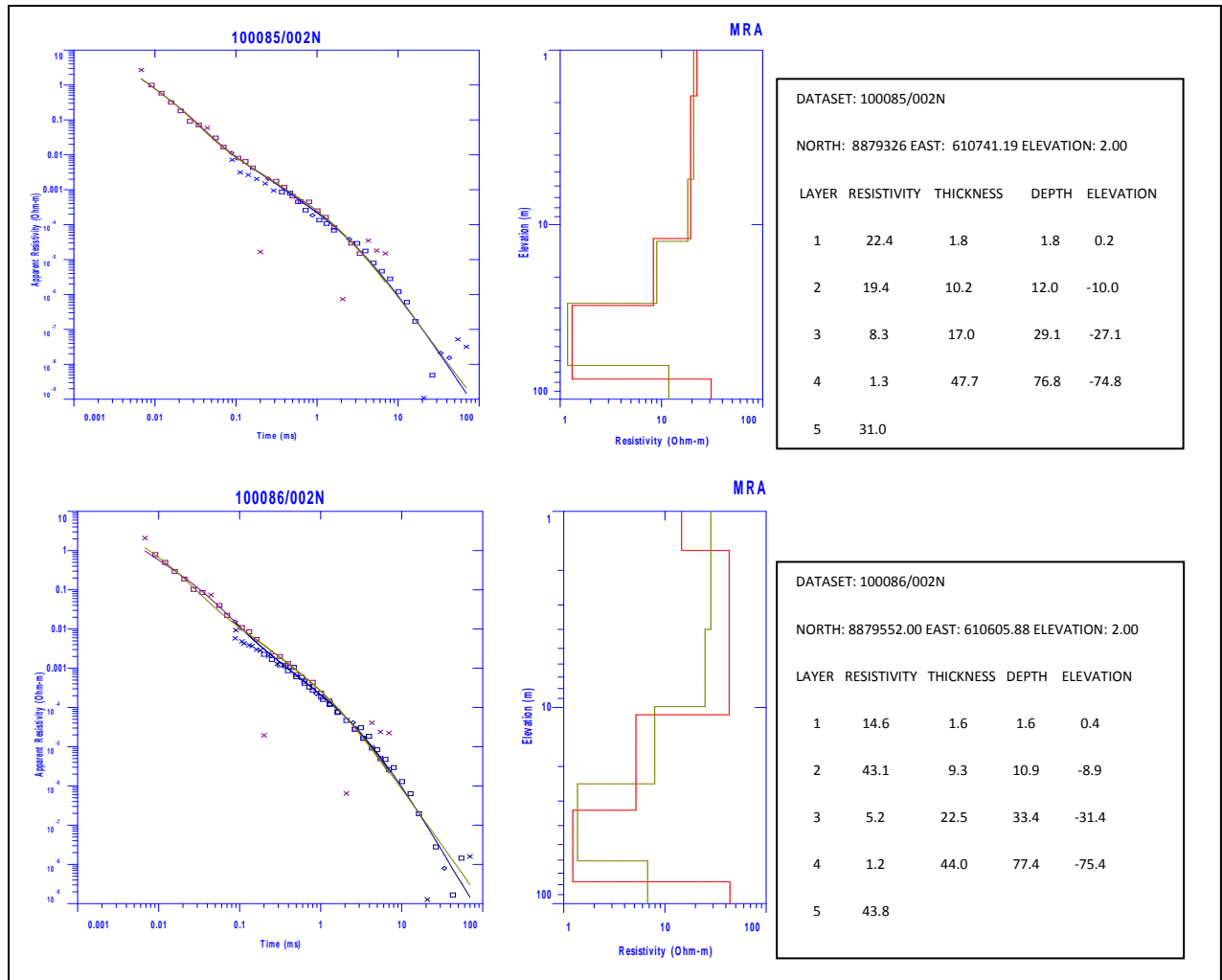


Figure 5.9 Resistivity inversion of TDEM data from sounding SND085 and SND086, showing the apparent resistivity curve inverted into actual resistivity by depth. On the left is a graph of apparent resistivity (Ωm) vs time (ms) with red and blue squares indicating measured high frequency and low-frequency data, respectively. The red and brown lines on the graph denote calculated and Occam's estimated smooth models, respectively. At the centre is the depth model showing depth vs calculated resistivity (red line) and the estimated smooth model (brown line). The right box shows the modelled geoelectric layers and their corresponding resistivity, thickness, and depth.

5.2 Spatial interpretive iso-maps

Spatial interpretive iso-maps generated by QGIS used interpolative schemes (Triangulation - Sibson) based on the master file (Appendix 2). These maps provide visualisation of the spatial distribution of resistivity, thickness, and depth to the main layers identified in this study. Examination of such data

are vital to identify not only regions of sufficient freshwater but also its volumetric capacity. It is also useful to assess areas vulnerable to saltwater intrusion through the spatial examination of the zone of dispersion and the salination. The freshwater aquifer of Maopa sits beneath a mostly thin layer of overburden and is separated from the underlying saline zone by a layer of mixing. Examination reveals the interior mangrove swamps and the Keakalo Bay to be sources of saltwater intrusion.

5.2.1 Freshwater layer

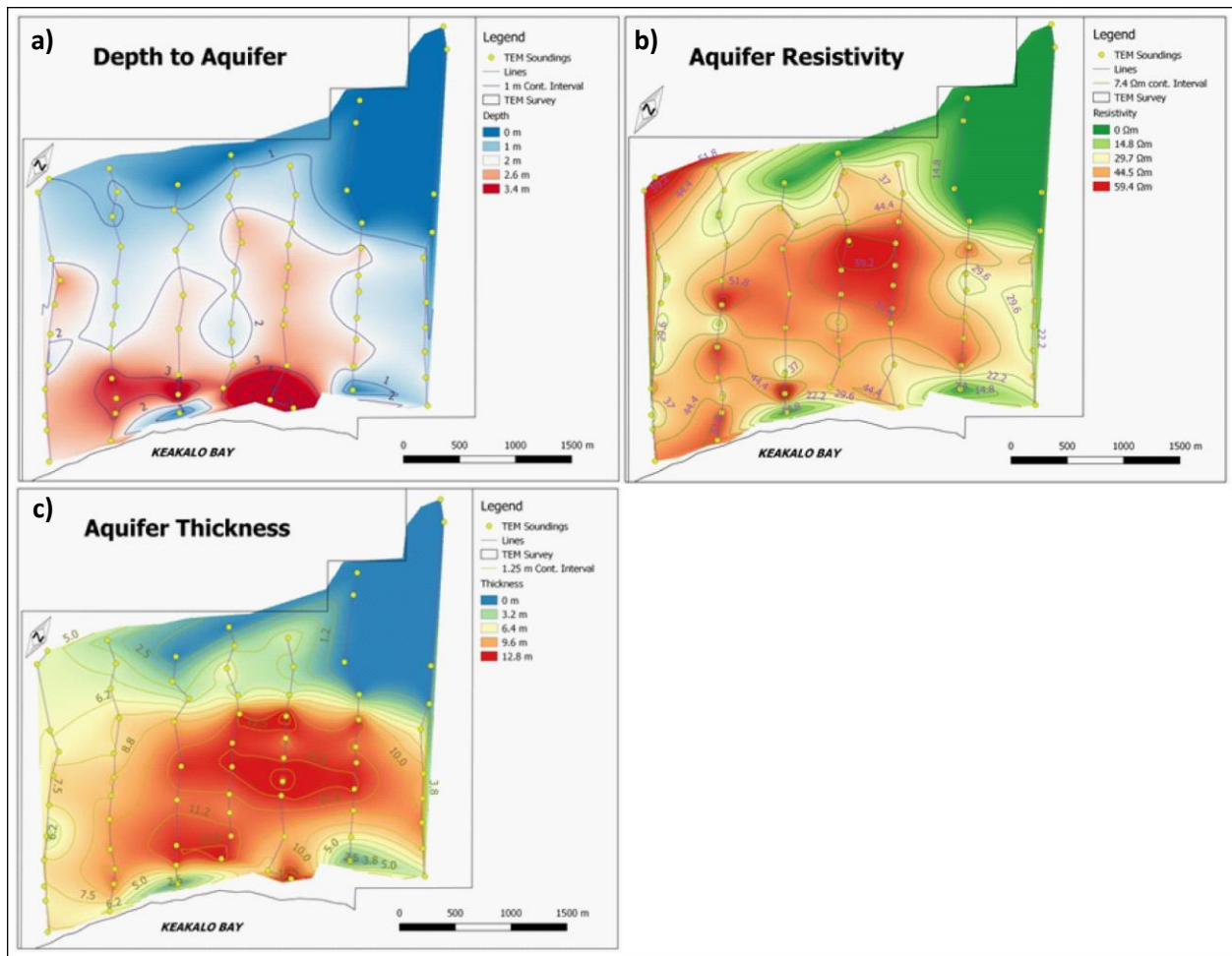


Figure 5.10 Freshwater layer interpretive iso-maps (a) depth to aquifer; (b) aquifer resistivity; and (c) aquifer thickness.

The characteristic of the freshwater aquifer attained from TDEM data is depicted in Figure 5.10 using interpolation of data from all seven lines. The depth (a) to aquifer is generally shallow only reaching greater depth mostly in the elevated sandy coast in the SSE region. A steady decrease in depth is generally concentrated more to the NNW and the NE. These regions are prone to seasonal surface water storage recharged by rain directly and indirectly (floods). The map also indicates the thickness of the top vadose layer, which with respect to the Mean Sea Level (MSL) is significant, as vulnerable areas become obvious. The map of resistivity of this layer (Figure 5.10(b)) divides into two parts: $100 \geq \rho \geq 20 \Omega\text{m}$ and $\rho \leq 20 \Omega\text{m}$. Areas below $20 \Omega\text{m}$ are in fact void of the freshwater layer which is

replaced by the zone of mixing and are more notable in the northern region and, in minor instances, near the coast. If the Quaternary alluvium sediments are largely homogenous as widely perceived, pore fluid conductivity in these regions may be higher. Regions showing resistivity values within the intermediate range take up most of the central part of the study area. The most distinctive pattern from the distribution of resistivity shows a cluster of consistent resistivity values in the most central part of the study area. While this feature is not unique, with minor occurrences to the south and west, the scale of the anomaly in an area unexploited and bounded by lower aquifer resistivity makes it significant. This feature may coincide with a more potable groundwater region whose pore fluid conductivity is likely controlled by coarser soil texture and size. Surrounding the high resistivity aquifer zone are areas subject to greater interaction with mixing zone and hence are vulnerable to salination as indicated by their low aquifer resistivity. Variations of aquifer resistivity may reflect changes in the soil texture but in some regions of elevated values that do not conform to the general trend, particularly the inland side of lines 1 and 2, variations associated with over modelling noisy HF data. The distribution of the thickness of the freshwater aquifer (Figure 5.10(c)) is in agreement with the aquifer resistivity iso-map. Regions of more appreciable aquifer thickness (up to 16 m) appear to coincide with regions of highest aquifer resistivity, although in general aquifers are thicker in the centre of the study area. Two minor areas with significant aquifer thickness (13 m) are also observed near the sandy coast and they correspond to regions known for their high yielding wells. Evidence of depletion of groundwater by excessive extraction from these regions may be indicated by a very low to non-existent aquifer thickness at the coastal end of line 3. Another depletion zone on the eastern side of the study area at the seaward end of line 6 is most probably caused by infiltration of surface seawater from Waipuna mangrove creek. The estimated total volumetric capacity of the groundwater resource of the study area is between 1.6 to 1.9 trillion litres. Calculations are based on information such as the areal extent of the survey (9908207 m²), the sum of thickness (546 m) of the modelled aquifer layer, and the estimated porosity ratio (0.30 – 0.35) for sand aquifer.

5.2.2 Mixing zone

The occurrence of the mixing zone is observed to conform to the freshwater aquifer thickness - Figure 5.11(a). More pronounced depths (14 to 16 m) to this layer are noticed in two regions identified to correspond with regions of elevated freshwater thickness. Shallow depths to the layer are observed quite prominently on the landward region of the study area but are widespread around the deeper regions in the centre of the area. Steeper depth gradients mark the landward boundary of interior saltwater intrusion on the NNW, whereas gradients elsewhere are generally gradual from the centre to the shallowest points.

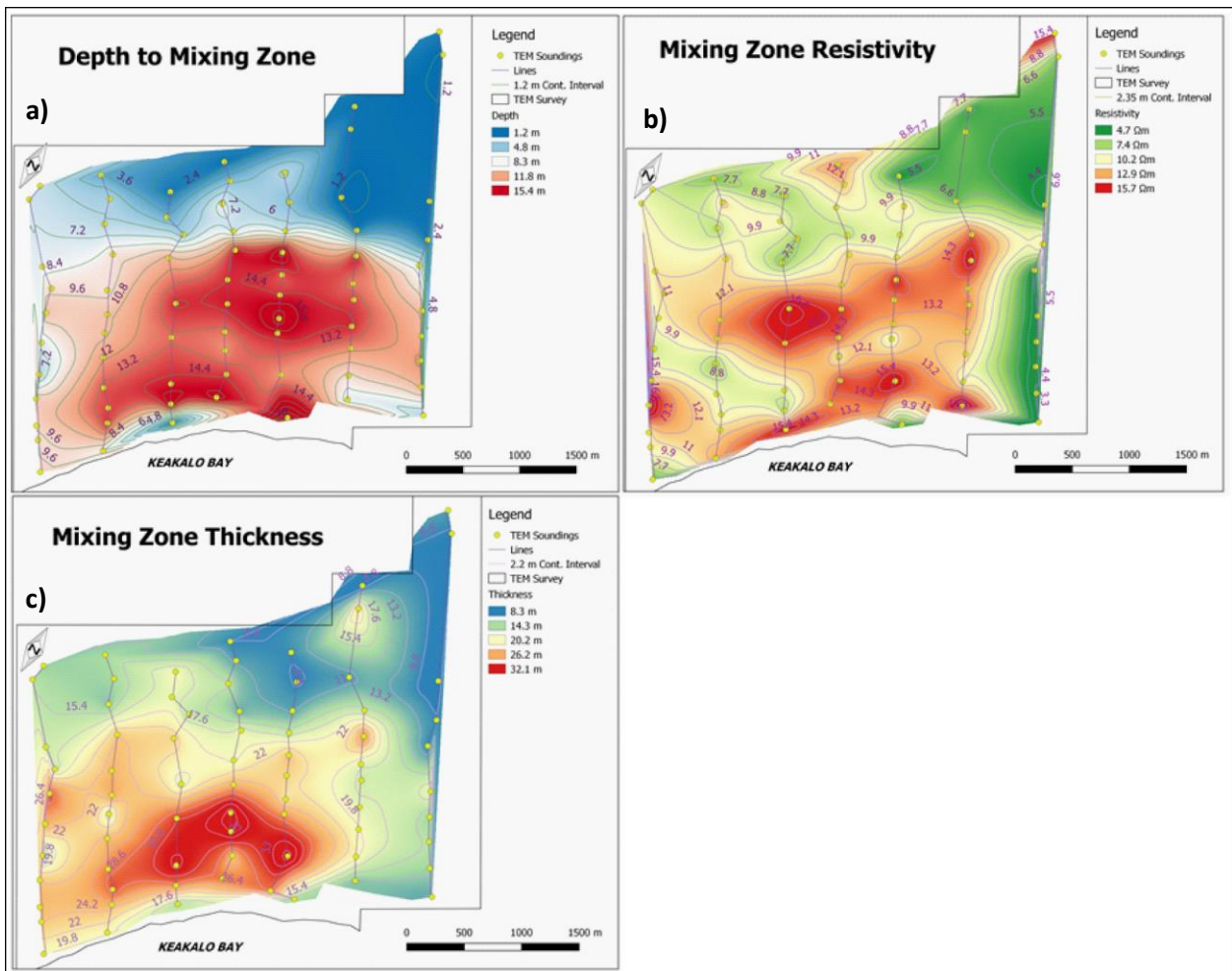


Figure 5.11 Mixing Zone interpretive iso-maps (a) depth to mixing zone; (b) mixing zone resistivity; (c) mixing zone thickness.

Regions of shallow depths to the mixing zone are potentially vulnerable to salination as indicated by the resistivity iso-map of the mixing zone. These regions typically correlate with the lowest mixing zone resistivity values observed in Figure 5.11(b) which can be grouped into low resistivity of $10 \geq \rho \geq 3 \Omega\text{m}$. The shallow mixing zone, apart from being drivers of seawater contamination at depth, can also create 3D inversion artefacts depending upon alignment to survey profiles. An intrusion of lower range mixing zone resistivity, observed on Lines 1 to 3 is an example of such a feature. More resistive regions of this layer amalgamate in the central part of the study area but similar resistivity is observed toward the sea stretching from line 1 to line 6. The nature of constituents of this layer is unknown but at observed depths and resistivity values the type of conduction is consistent with pore fluid conduction dominated by fluid concentration of saltwater. The mixing zone thickness (Figure 5.11(c)) is more prominent near the central coast bounded by lines 3 and 5 where greater depths to the layer are determined. The layer thickness decreases gradually outward from the region of high thickness but the gradient is steepest near the coast between lines 3 and 5. The observations of reduced mixing zone thickness and resistivity in section 5.1.5 strongly emphasising the influence of

salinity by the neighbouring mangrove swamp and estuary as clearly illustrated. While the study of the dynamics of saltwater-freshwater mixing is still in its infancy, studies have shown that the primary driver for movement of fresh and saltwater is the density contrast of the fluids (Reilly & Goodman, 1984). Furthermore the zone of mixing is described by Cooper et al. (1964) as cited by Reilly and Goodman (1985) to be affected by the diffusion of freshwater and saltwater and its seaward movement. This phenomenon forces saltwater to migrate toward the region of mixing, forming circulation of seawater. Thickness of the mixing can vary but apart from the fluid density it is also subject to hydraulic conductivity, porosity, hydraulic gradient (Fetter, 1993), and tidal changes (Cooper, 1959) as cited by Nielsen et al. 2005. A study by Lu (2011) that used numerical simulations asserted that widening of mixing zones is caused by the levelling out of periods between the mass transfer and the transient boundary attributed to the unstable mass transfer effects, whereas thicker mixing zones were a result of a low-permeable mixing layer overlaying a fast flow layer (most probably saltwater intrusion).

5.2.3 Saline zone

The layer of salination in Figure 5.12 is omnipresent beneath all soundings represented in the maps. This observation not only confirms that groundwater originating from inland is disconnected from the system, but also enhances the idea of a freshwater lens and its high vulnerability to salination. The presence of this layer beneath the study area is differentiated by varying depths as shown in Figure 5.12(a). Minimum depths are most extensive across all lines in the landward region of the study area while regions at the centre of the study area near the coast exhibit greater depths. The gradient on the coastal side is somewhat subdued by a small area of shallow depth, but is generally steeper compared with the landward direction where depth gradients are gradual.

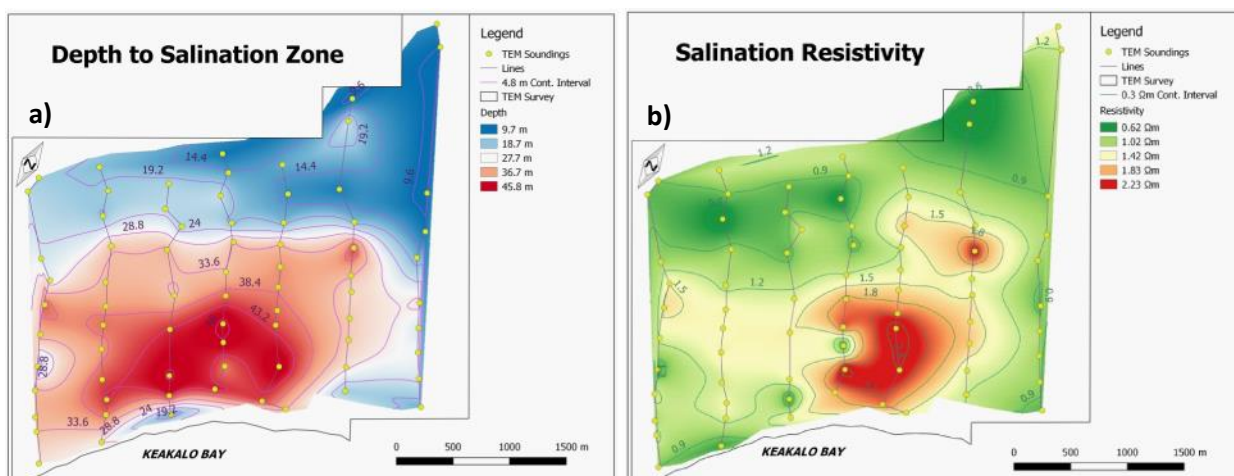


Figure 5.12 Salination interpretive iso-maps (a) depth to salination; (b) salination resistivity.

There is no doubt the saline zone has a symmetry similar to the small island model, however the symmetry may differ slightly because of the style of infiltration imposed by both the coast and the interior mangrove swamp. One explanation for the gradual depth gradient of the saline zone in the interior is the effect of surface diffusion of fluids, which generally radiate outwards thus giving a modest gradient in this region. Figure 5.12(b) shows the resistivity distribution of the saltwater intrusion layer which is classed as very low, ranging $3 \geq \rho \geq 0.4 \Omega\text{m}$. The resistivity of this layer is undoubtedly consistent with that of seawater ($0.3 \Omega\text{m}$) observed across the whole study area where conduction is through the pore fluid and is mainly in the more dense seawater. Low resistivity values correlate with shallow depths of occurrence while elevated values congregate around the deeper parts of this layer. The elevated values ($\geq 2 \Omega\text{m}$) for the saline layer is not an isolated case, as similar studies by Nielsen et al. (2006) and El-Kaliouby and Abdalla (2015) have also modelled these values but at varying depths. Their assertion of seawater being the main determinant of such resistivity is a view shared widely by these studies.

Chapter 6 Summary

Maopa groundwater resource is situated in a complex coastal hydrological system, and represents a freshwater lens floating on a layer of mixing, and a layer of salination at depth. Despite the complexity, 1D inversion of 76 central loop TEM soundings identified four primary geoelectric layers of distinctive characteristics and provided visualizations that emphasize the key implications of these characteristics. The use of central loop TEM measurements has, therefore proven vital in acquiring subsurface information in such a complex environment.

The findings show that a thin vadose layer of variable resistivity (1.2 to 452 Ωm) occupies the surface layer with thickness mimicking the surface elevation. Beneath this layer is the freshwater lens and has an intermediate resistivity of about $100 \geq \rho \geq 20 \Omega\text{m}$. The freshwater layer can reach a thickness of up to 16 m in the central parts of the survey area, whereas reduced thickness is observed in the interior mangrove swamp and the shoreline. The mixing zone is found at depths of up to 19 m in the central parts of the survey area and has a thickness range of 6.5 to 37 m. This layer occupies a region classed as low resistivity $\leq 10 \rho > 3 \Omega\text{m}$. The saline layer identified across all soundings occurs at a very low resistivity stratum of $3 \geq \rho \geq 0.4 \Omega\text{m}$. This layer is found to be highly influenced by the pore fluid conduction of the concentration of seawater and is expected at greater depth (50 m) in the centre of the study area and shallow depth (8 m) both at the interior mangrove swamps and the shoreline.

To determine the location and volume of groundwater resource, geospatial analysis of 1D inversion models was required. Regions of ample freshwater are clearly identified in the central parts of the array of lines, which are bounded by the mangrove swamp in the interior and Keakalo Bay on the seaside. More volume of freshwater, however, can be found in the middle of lines 3, 4, 5, and 6 and near the coast of lines 3 and 4. Based on the total thickness of this layer, its estimated porosity, and the areal extent of the survey, an estimation of the total volumetric capacity of the groundwater resources was found to be between 1.6 to 1.9 trillion litres.

Areas of maximum threat by salination are mostly observed near the interior mangrove swamp in the NNW end of the line, the Maurele estuary in the east, and close to the shore where the zone of mixing is thin and the saline layer is at its shallowest. Minor threats are also possible in regions near line 1 where the intrusion of mangrove swamps are adjacent. Special emphasis must be given to the mixing as it may be the indicator for the health of the groundwater resource and the encroaching saltwater.

The observation of symmetry between the freshwater layer, the mixing zone, and the saline layer and also the wide spread detection of the zone of salination at depth suggest the groundwater resources are characteristic of those of small Islands. The groundwater resource is a freshwater lens disconnected from inland recharge and floats on a layer of mixing and saltwater.

Reconfiguration of the survey parameters to 30 gates for line 7 and supplementary soundings subsequent to that enabled the detection of a deep basement unit at depths of up to 75 m near the coast. Although the actual resistivity of this unit is relatively poorly constrained it is interpreted as the Early Miocene to Late Pliocene Kupiano beds whose general dip is toward the coast. This discovery is important because it allows inferences to be made of the estimated thickness of the alluvial sedimentary deposits overlying the basement unit.

Taken together these findings have not only demonstrated the success of the central loop TEM method in identifying the extent of salination and the characterization of the groundwater resource in Maopa, but also greatly improve previous findings based on the DC Schlumberger resistivity method. The success of the TEM method is the result of improved handling, large dynamic range, improved instrumentation and its ability to acquire high spatial sounding measurements.

The limited information about the deep basement unit and lack of soundings near the coast does not allow us to extensively image the basal layer and satisfactorily model the mixing and salination zone, respectively. Such opportunities will be the subject of future studies.

References

- Bucker, M., Garcia, S. L., Guerrero, O. B., Caballero, M., Perez, L., Caballero, L., ... Garay-Jimenez, F. (2017). Geoelectrical and electromagnetic methods applied to paleolimnological studies: Two examples from desiccated lakes in the basin of Mexico. *Newsletter of the Mexican Geological Society*, 69(2), 279 – 298.
- Christiansen A.V., Auken E., & Sørensen K. (2006). The transient electromagnetic method. In: Kirsch R. (eds) *Groundwater Geophysics*. Springer, Berlin, Heidelberg, 978-3-540-29387-3.
https://doi.org/10.1007/3-540-29387-6_6
- Constable, S. C., Parker, R. L., & Constable, C. G. (1987). Occam's inversion: A practical algorithm for generating smooth models from electromagnetic sounding data. *Geophysics*, 52(3) 289-300.
- Cooper, H. H., Jr. (1959). A hypothesis concerning the dynamic balance of fresh water and salt water in a coastal aquifer. *Journal of Geophysical Research*, 64(4), 461-467.
- Cooper, H.H., Jr., Kohout, F.A., Henry, H.A. & Glover, R.E. (1964). Sea water in coastal aquifers. US Geological Survey Water-Supply Paper 1613-C.
- El-Kaliouby, H., & Abdalla, O. (2015). Application of time-domain electromagnetic method in mapping saltwater intrusion of a coastal alluvial aquifer: North Oman. *Journal of Applied Geophysics*, 115, 59 – 64.
- Ezersky, M.G., & Frumkin, A. (2017). Evaluating and mapping of Dead Sea coastal aquifer salinity using Transient Electromagnetic (TEM) resistivity measurements. *C.R. Geoscience*, 349, 1-11
- Farquharson C.G., & Oldenburg, D.W. (1993). Inversion of time-domain electromagnetic data for a horizontally layered Earth. *Geophysical Journal International*, 114, 433-442
- Fenneman, N.M. (1916). Physiographic subdivision of the United States. Department of Geology: University of Cincinnati. Retrieved from <https://www.pnas.org/content/pnas/3/1/17.full.pdf?ck=nck>
- Fetter, C.W. (1993). Contaminant Hydrogeology. New York: Macmillan.
- Fitterman, D.V., & de Sozua Filho, O.A. (2009). Transient electromagnetic soundings near Great Sand Dunes National Park and Preserve, San Luis Valley (2006 Field Season), Colorado: *U.S. Geological Survey Open-File Report 2009-1051*.
Retrieved from <https://pubs.usgs.gov/of/2009/1051/downloads/OF09-1051.pdf>
- Fitterman, D.V. & Stewart, M.T. (1986). Transient Electromagnetic Sounding for Groundwater. *Geophysics*, 51, 955-1005.

Fitterman, D.V. (2017). Transient electromagnetic soundings in the San Luis Valley, Colorado, near the Great Sand Dunes National Park and Preserve and the Alamosa National Wildlife Refuge (field seasons 2007, 2009, and 2011): *U.S. Geological Survey Data Series 1043*, 39 p.

<https://doi.org/10.3133/ds1043>. Retrieved from <https://pubs.usgs.gov/ds/1043/ds1043.pdf>

Geonics Limited. (2015). *PROTEM CH*. Retrieved from <http://www.geonics.com/html/protem-cm.html>

Goldman, M., Gilad, D., Ronen, A., & Melloul, A. (1991). Mapping of seawater intrusion into coastal aquifer of Israel by the time domain electromagnetic method. *Geoexploration*, 28, 153-174

Hall, A.J. (1984). Hydrology in tropical Australia and Papua New Guinea. *Hydrological Sciences Journal*, 29(4), 399-423, DOI: 10.1080/02626668409490959

Ingham, M., McConchie, J.A., Wilson, S.R., Cozens, N. (2006). Measurement and monitoring of saline intrusion using dc resistivity traversing. *Journal of Hydrology (NZ)*, 45 (2), 89-102

Jakeman, A., Barreteau, O., Hunt, R. et al. (2016). 'Integrated Groundwater Management: An Overview of Concepts and Challenges', in A J Jakeman, O Barreteau, R J Hunt, J-D Rinaudo, A Ross (ed.), *Integrated Groundwater Management. Concepts, Approaches and Challenges*, Springer Nature, Online, pp. 3-20.

Kaufman, A.A., & Keller, G.V. (1983). Frequency and transient sounding: Amsterdam, Elsevier, 685 p.

Leite, D.N., Bortolozzo, C.A., Porsani, J.L., Couto, Jr., M.A., Campana, J.D.R., dos Santos F.A.M., ... Stangari, M.C. (2018). Geoelectrical characterization with 1D VES/TEM joint inversion in Urpes-SP region, Parana Basin: Applications to Hydrology. *Journal of Applied Geophysics*, 151, 205-220

Lu, C. (2011). Mixing in complex coastal hydrogeological systems. Georgia Institute of Technology.

Retrieved from

https://smartech.gatech.edu/bitstream/handle/1853/39600/lu_chunhui_201105_phd.pdf

MacAlpine, J.R., Keig, G., Falls, R. (1983). Climate of Papua New Guinea. *Common wealth Scientific and industrial Research Organisation (Australia)*, 551.6995'3, 208p

McNeill, J.D. (1990). Use of electromagnetic methods for groundwater studies, in Ward, S.H., ed., Geotechnical and environmental geophysics: Tulsa, *Society of Exploration Geophysicists*, pp. 191–218.

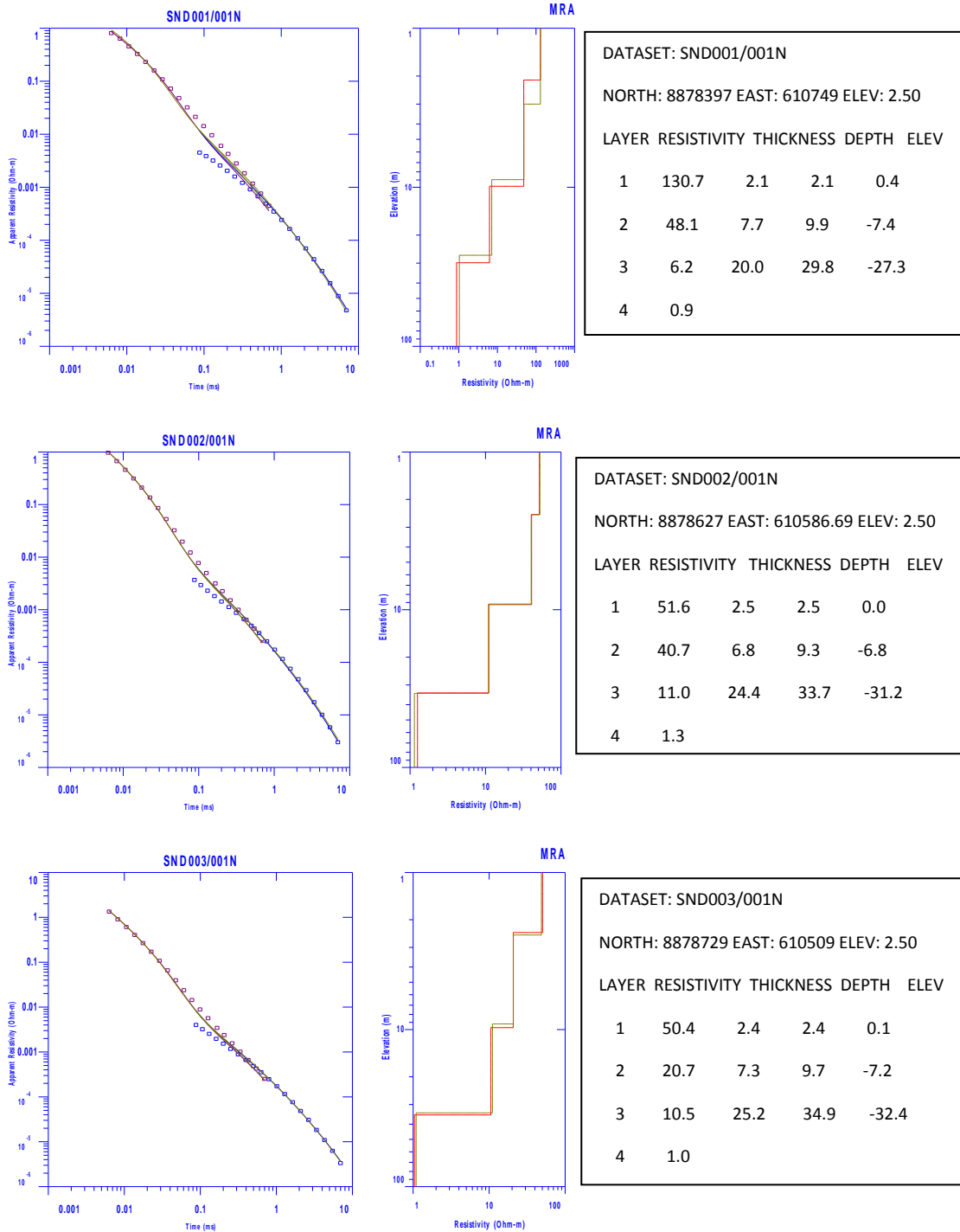
Melloul, A.J., & Goldenberg, L.C. (1997). Monitoring of Seawater intrusion in coastal aquifers: Basics and Local Concerns. *Journal of Environmental Management*, 51, 73-86

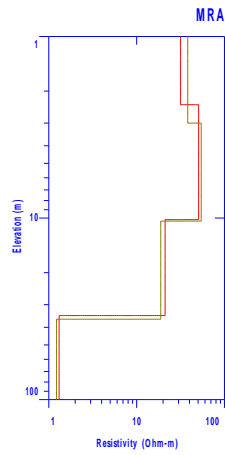
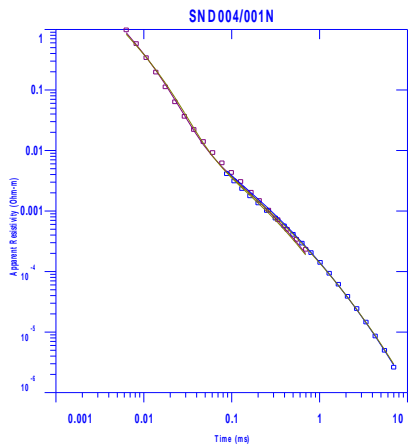
- Murgalet, D., & Tick, G. (2007). The extent of saltwater intrusion in southern Baldwin County, Alabama. *Environmental Geology*, 55, 1235-1245
- Newman, G.A., Anderson, W.L., & Hohmann, G.W. (1987). Interpretation of transient electromagnetic soundings over three-dimensional structure for the central-loop configuration. *Geophysical Journal of the Royal Astronomical Society*, 89, 889-914.
- Nielsen, N., Jorgensen, N.O., & Gelting, P. (2007). Mapping of the freshwater lens in coastal aquifer on the Keta Barrier (Ghana) by transient electromagnetic soundings. *Journal of Applied Geophysics*, 62, 1-15
- Pieters, P.E. (1978). Port Moresby-Kalo-Aroa, Papua New Guinea - 1:250 000 Geological Series, Bureau of Mineral Resources, *Geology and Geophysics, Explanatory Notes, SC/55-6,7*, 55pp.
- Post, V.E.A., Eichholz, M., & Brentführer, R. (2018). Groundwater management in coastal zones. Bundesanstalt für Geowissenschaften und Rohstoffe (BGR). Hannover, Germany, 107 pp.
- Reilly, T.E., & Goodman, A.S. (1985). Quantitation analysis of saltwater-freshwater relations in groundwater systems – a historical perspective. *Journal of Hydrology*, 80, 125-160
- Shaaban, H., El-Qady, G., Al-Sayed, E., Ghazala, H., & Taha, A.I. (2016). Shallow groundwater investigation using time-domain electromagnetic (TEM) method at Itay El-Baroud, Nile Delta, Egypt. *NRIAG Journal of Astronomy and Geophysics*, 5, 323-333
- Verave, T. R. (2018). Mapping saltwater incursion using vertical electrical resistivity sounding in the coastal village of Maopa, Papua New Guinea. Unpublished directed individual study course GPHYS 439 field report.
- Ward, S.H., & Hohmann, G.W. (1987). Electromagnetic Theory for Geophysical Applications. In: Nabighian, M.N., Ed., *Electromagnetic Methods in Applied Geophysics*, Vol. 1, Society of Exploration Geophysicists, 131-311

Appendix 1

Smooth data and 1D models for each site

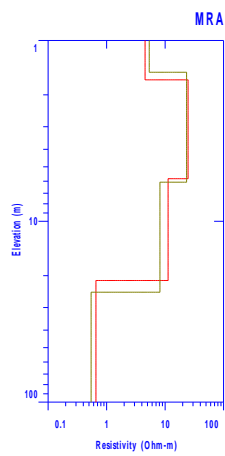
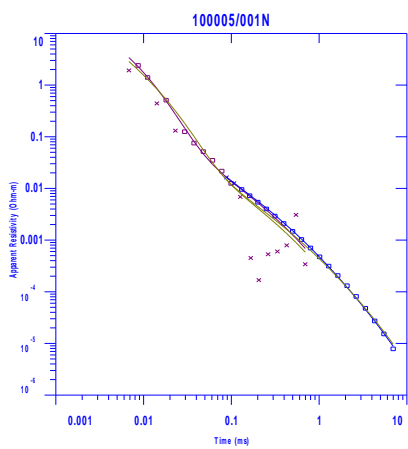
6.1 Line 1





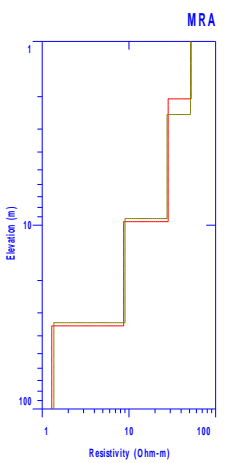
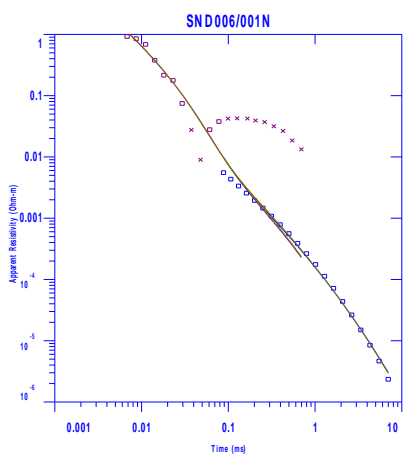
DATASET: SND004/001N
 NORTH: 8878931 EAST: 610385 ELEV: 2.50

LAYER	RESISTIVITY	THICKNESS	DEPTH	ELEV
1	31.6	2.4	2.4	0.1
2	50.8	7.8	10.2	-7.7
3	21.1	24.3	34.5	-32.0
4	1.3			



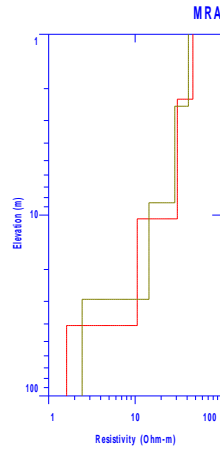
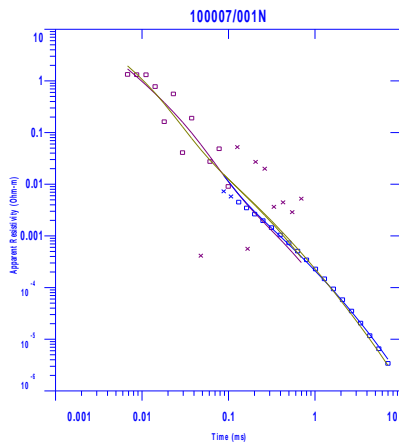
DATASET: SND005/001N
 NORTH: 8879128 EAST: 610297 ELEV: 2.00

LAYER	RESISTIVITY	THICKNESS	DEPTH	ELEV
1	4.6	1.7	1.7	0.3
2	24.7	4.2	5.8	-3.8
3	11.3	15.5	21.3	-19.3
4	0.7			



DATASET: SND006/001N
 NORTH: 8879376 EAST: 610170 ELEV: 2.00

LAYER	RESISTIVITY	THICKNESS	DEPTH	ELEV
1	52.1	2.1	2.1	-0.1
2	28.3	7.5	9.6	-7.6
3	8.7	25.7	35.3	-33.3
4	1.3			

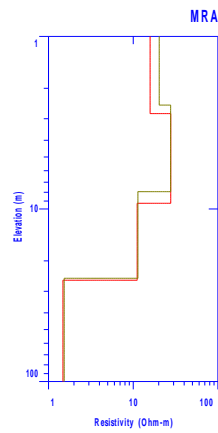
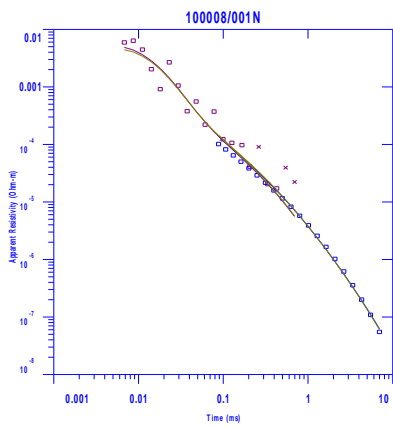


DATASET: SND007/001N

NORTH: 8879623 EAST: 610066 ELEV: 2.00

LAYER RESISTIVITY THICKNESS DEPTH ELEV

LAYER	RESISTIVITY	THICKNESS	DEPTH	ELEV
1	46.6	2.3	2.3	-0.3
2	30.8	8.2	10.5	-8.5
3	10.6	30.4	40.8	-38.8
4	1.6			

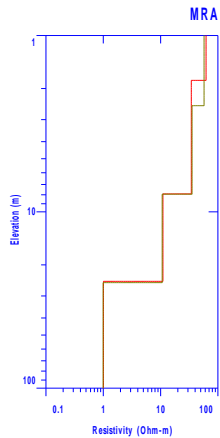
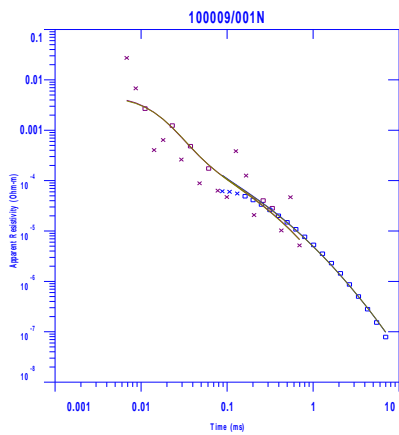


DATASET: SND008/001N

NORTH: 8879831 EAST: 609921 ELEV: 2.50

LAYER RESISTIVITY THICKNESS DEPTH ELEV

LAYER	RESISTIVITY	THICKNESS	DEPTH	ELEV
1	15.8	2.8	2.8	-0.3
2	27.7	6.5	9.3	-6.8
3	11.1	16.6	25.9	-23.4
4	1.5			

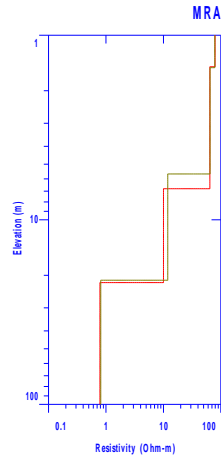
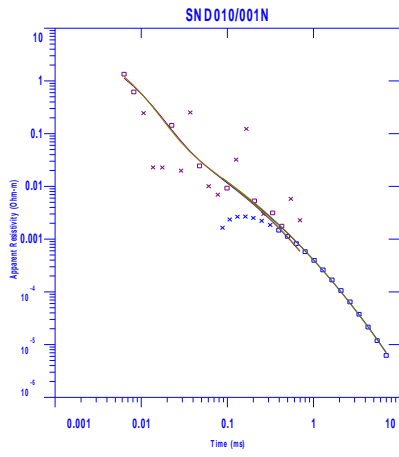


DATASET: SND009/001N

NORTH: 8879955 EAST: 609829 ELEV: 2.00

LAYER RESISTIVITY THICKNESS DEPTH ELEV

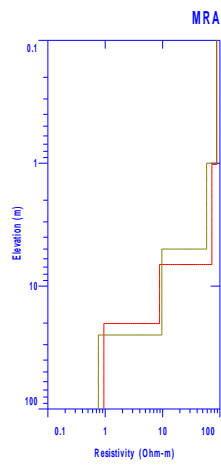
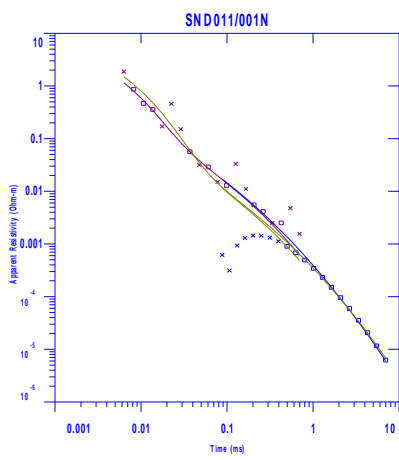
LAYER	RESISTIVITY	THICKNESS	DEPTH	ELEV
1	62.1	1.8	1.8	0.2
2	34.3	6.1	7.9	-5.9
3	11.0	16.9	24.8	-22.8
4	1.0			



DATASET: SND010/001N

NORTH: 8880399 EAST: 609423 ELEV: 1.50

LAYER	RESISTIVITY	THICKNESS	DEPTH	ELEV
1	79.2	1.5	1.5	0.0
2	64.3	5.3	6.8	-5.3
3	10.0	15.1	21.9	-20.4
4	0.8			

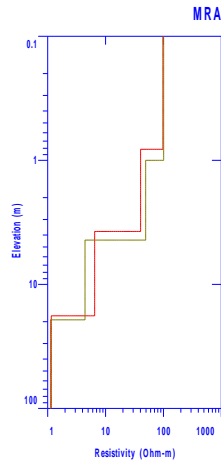
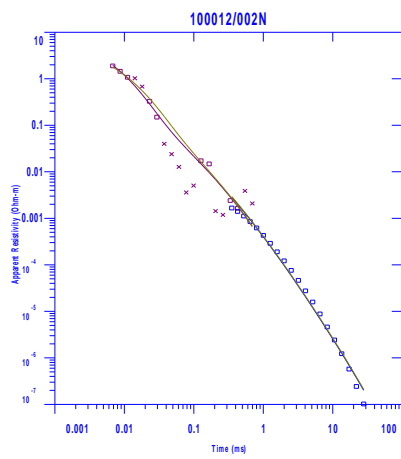


DATASET: SND011/001N

NORTH: 8880552 EAST: 609443 ELEV: 1.50

LAYER	RESISTIVITY	THICKNESS	DEPTH	ELEV
1	87.7	1.0	1.0	0.5
2	72.3	5.7	6.7	-5.2
3	8.9	13.5	20.2	-18.7
4	0.9			

6.2 Line 2

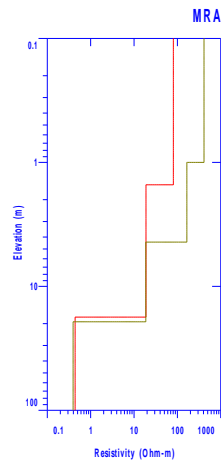
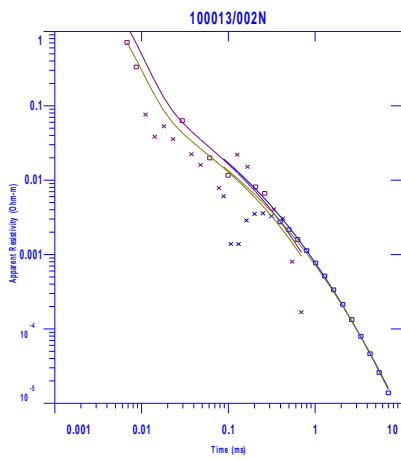


DATASET: SND012/002N

NORTH: 8880911 EAST: 609853 ELEV: 1.00

LAYER RESISTIVITY THICKNESS DEPTH ELEV

LAYER	RESISTIVITY	THICKNESS	DEPTH	ELEV
1	98.0	0.8	0.8	0.2
2	40.4	2.9	3.7	-2.7
3	6.5	14.2	17.9	-16.9
4	1.2			

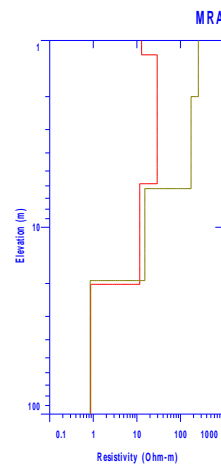
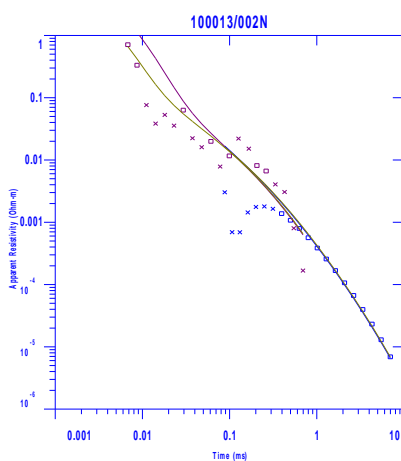


DATASET: SND013X/002N

NORTH: 8880772 EAST: 610026.4 ELEV: 1.50

LAYER RESISTIVITY THICKNESS DEPTH ELEV

LAYER	RESISTIVITY	THICKNESS	DEPTH	ELEV
1	80.5	1.5	1.5	0.0
2	18.9	16.2	17.7	-16.2
3	0.4			

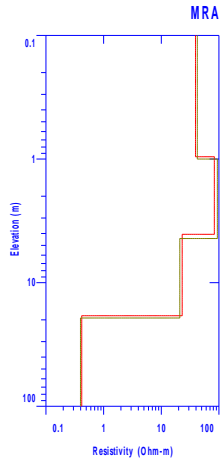
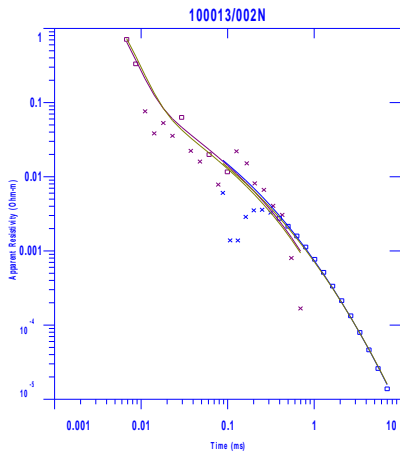


DATASET: SND013XA/002N

NORTH: 8880772 EAST: 610026.4 ELEV: 1.50

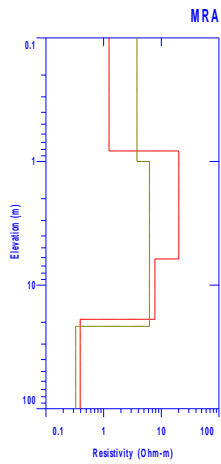
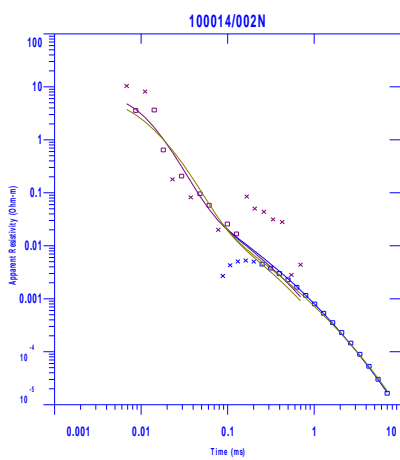
LAYER RESISTIVITY THICKNESS DEPTH ELEV

LAYER	RESISTIVITY	THICKNESS	DEPTH	ELEV
1	12.9	1.2	1.2	0.3
2	29.3	4.7	5.8	-4.3
3	11.7	14.3	20.2	-18.7
4	0.9			



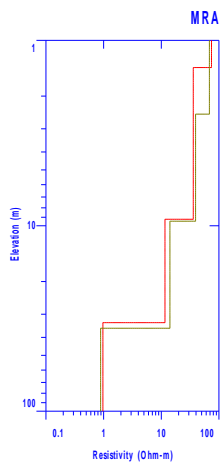
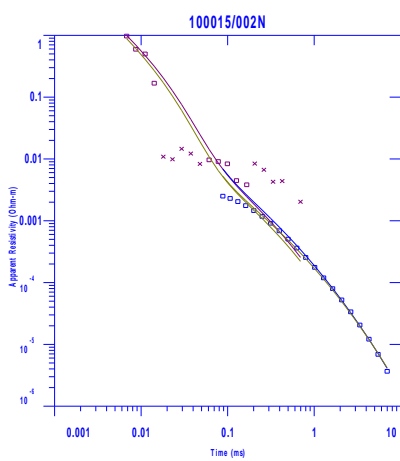
DATASET: SND013XX/002N
 NORTH: 8880772 EAST: 610026.4 ELEV: 1.00

LAYER	RESISTIVITY	THICKNESS	DEPTH	ELEV
1	39.2	1.0	1.0	0.0
2	83.3	3.1	4.1	-3.1
3	23.1	14.5	18.5	-17.5
4	0.4			



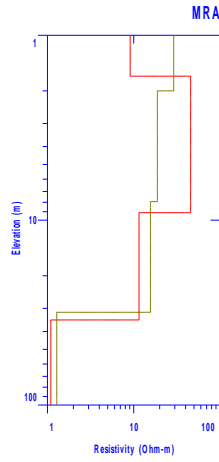
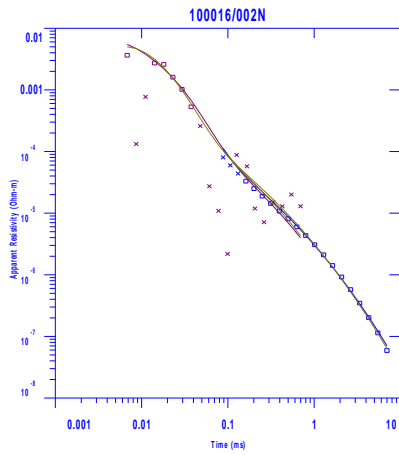
DATASET: SND014X/002N
 NORTH: 8880558 EAST: 610101 ELEV: 1.00

LAYER	RESISTIVITY	THICKNESS	DEPTH	ELEV
1	1.2	0.8	0.8	0.2
2	20.1	5.3	6.1	-5.1
3	7.8	12.8	18.9	-17.9
4	0.4			



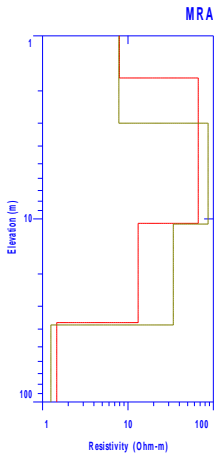
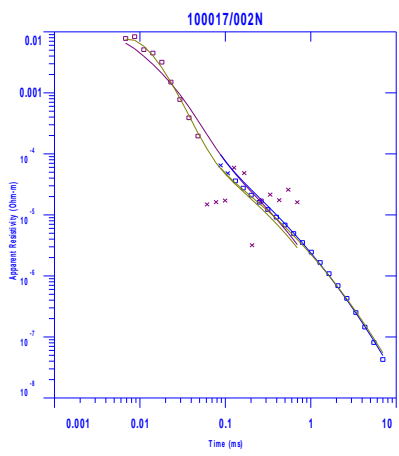
DATASET: SND015X/002N
 NORTH: 8880369 EAST: 610304 ELEV: 1.50

LAYER	RESISTIVITY	THICKNESS	DEPTH	ELEV
1	74.3	1.4	1.4	0.1
2	35.9	7.8	9.2	-7.7
3	11.6	24.1	33.3	-31.8
4	1.0			



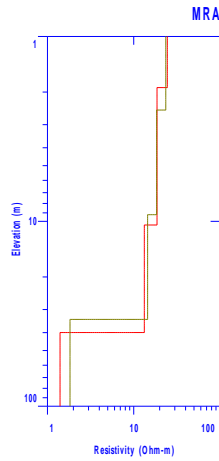
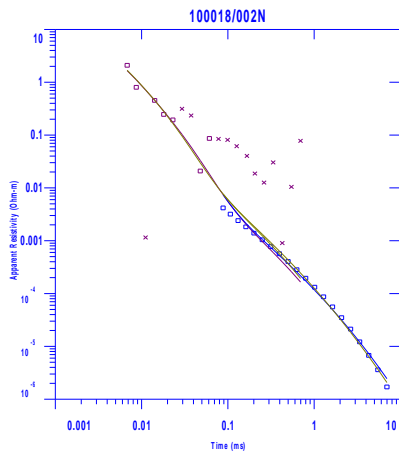
DATASET: SND016X/002N
 NORTH: 8880072 EAST: 610426 ELEV: 2.00

LAYER	RESISTIVITY	THICKNESS	DEPTH	ELEV
1	9.1	1.7	1.7	0.3
2	45.7	7.4	9.1	-7.1
3	11.5	25.6	34.7	-32.7
4	1.1			



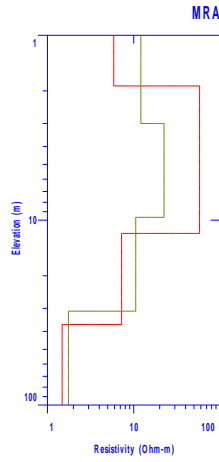
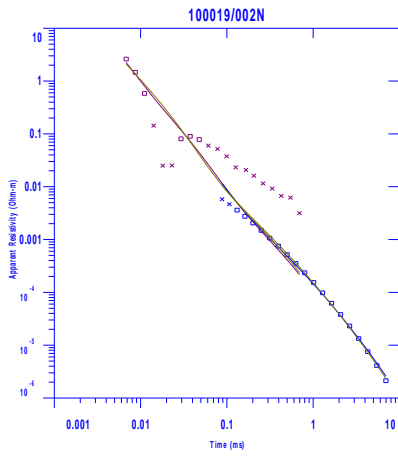
DATASET: SND017X/002N
 NORTH: 8879891 EAST: 610537.5 ELEV: 2.00

LAYER	RESISTIVITY	THICKNESS	DEPTH	ELEV
1	8.0	1.7	1.7	0.3
2	66.5	8.9	10.6	-8.6
3	13.2	26.3	36.8	-34.8
4	1.5			



DATASET: SND018X/002N
 NORTH: 8879738 EAST: 610602.3 ELEV: 2.00

LAYER	RESISTIVITY	THICKNESS	DEPTH	ELEVA
1	24.6	1.9	1.9	0.1
2	18.7	8.6	10.5	-8.5
3	13.3	29.5	39.9	-37.9
4	1.4			

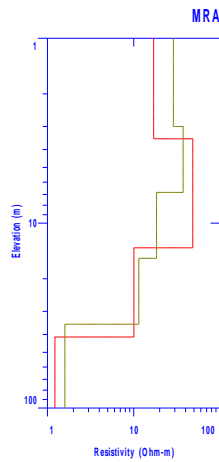
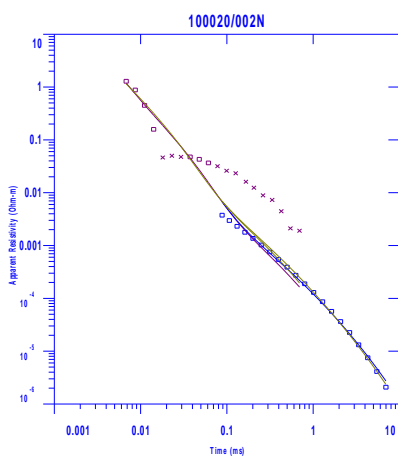


DATASET: SND019X/002N

NORTH: 8879547 EAST: 610698.5 ELEV: 2.00

LAYER RESISTIVITY THICKNESS DEPTH ELEV

LAYER	RESISTIVITY	THICKNESS	DEPTH	ELEV
1	5.9	1.9	1.9	0.1
2	58.0	9.9	11.8	-9.8
3	7.2	24.9	36.7	-34.7
4	1.5			

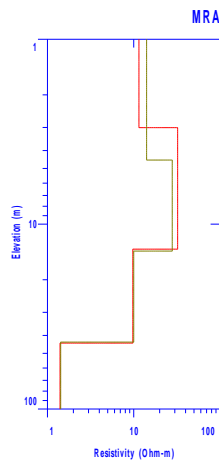
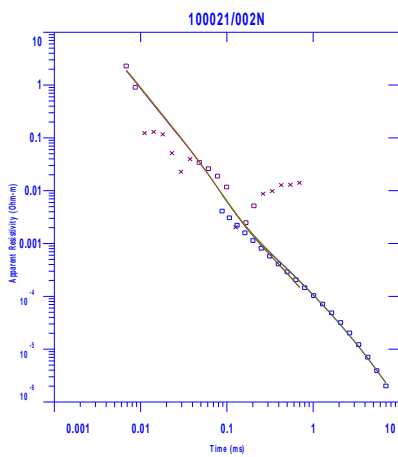


DATASET: SND020X/002N

NORTH: 8879322 EAST: 610843.2 ELEV: 3.50

LAYER RESISTIVITY THICKNESS DEPTH ELEV

LAYER	RESISTIVITY	THICKNESS	DEPTH	ELEV
1	17.0	3.5	3.5	0.0
2	48.5	10.1	13.6	-10.1
3	10.1	27.7	41.3	-37.8
4	1.2			

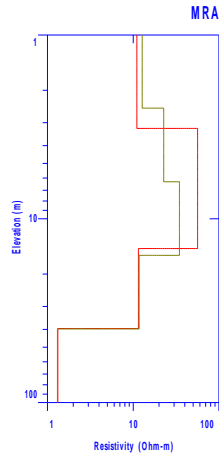
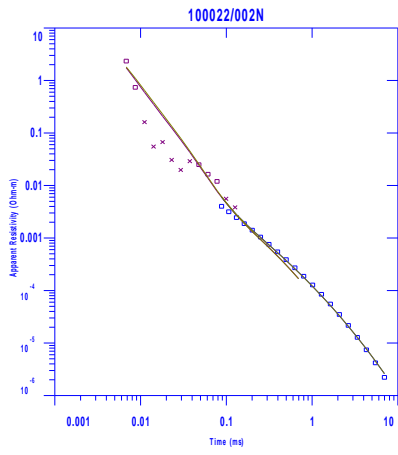


DATASET: SND021X/002N

NORTH: 8879191 EAST: 610969.8 ELEV: 3.00

LAYER RESISTIVITY THICKNESS DEPTH ELEV

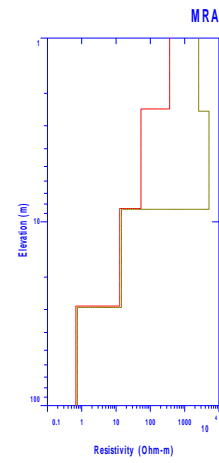
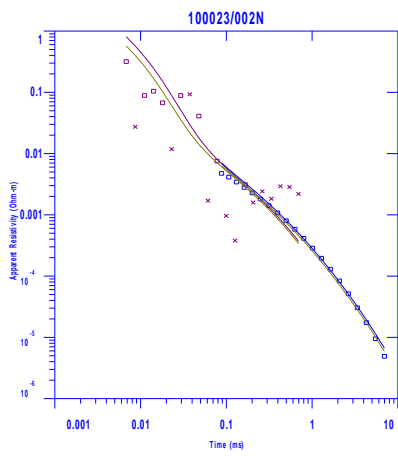
LAYER	RESISTIVITY	THICKNESS	DEPTH	ELEV
1	11.5	3.0	3.0	0.0
2	32.3	10.6	13.7	-10.7
3	9.8	30.4	44.0	-41.0
4	1.4			



DATASET: SND022X/002N

NORTH: 8879073 EAST: 611133 ELEV: 3.50

LAYER	RESISTIVITY	THICKNESS	DEPTH	ELEV
1	11.0	3.2	3.2	0.3
2	56.4	11.3	14.5	-11.0
3	11.5	25.0	39.5	-36.0
4	1.3			

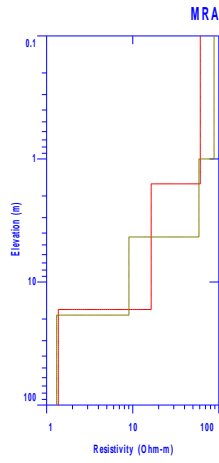
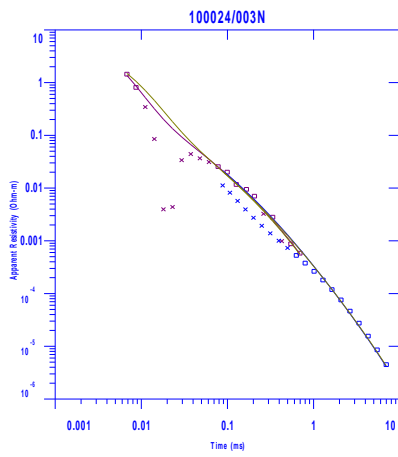


DATASET: SND023X/002N

NORTH: 8878844 EAST: 611126.5 ELEV: 2.50

LAYER	RESISTIVITY	THICKNESS	DEPTH	ELEV
1	365.4	2.4	2.4	0.1
2	53.2	6.0	8.5	-6.0
3	12.8	20.3	28.7	-26.2
4	0.7			

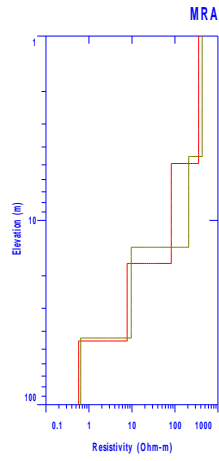
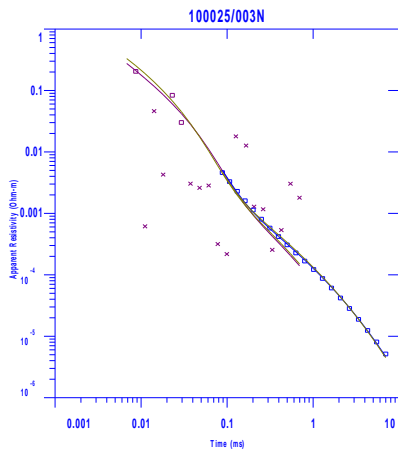
6.3 Line 3



DATASET: SND024X/003

NORTH: 8879273 EAST: 611521.2 ELEV: 1.50

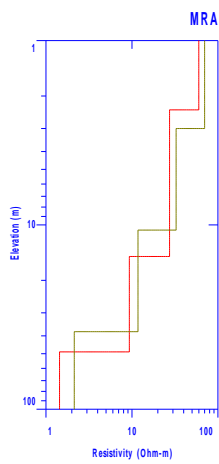
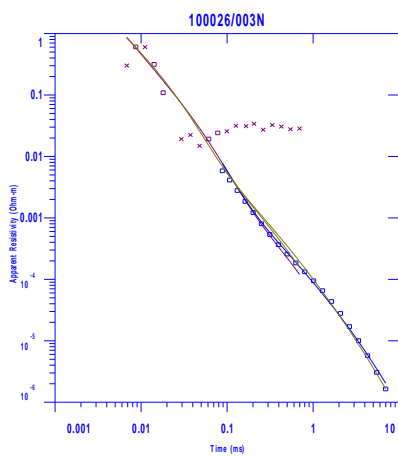
LAYER	RESISTIVITY	THICKNESS	DEPTH	ELEV
1	60.9	1.6	1.6	-0.1
2	16.4	15.2	16.7	-15.2
3	1.4			



DATASET: SND025X/003N

NORTH: 8879506 EAST: 611470 ELEV: 5.00

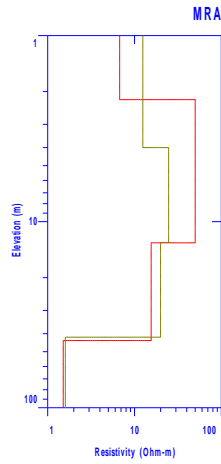
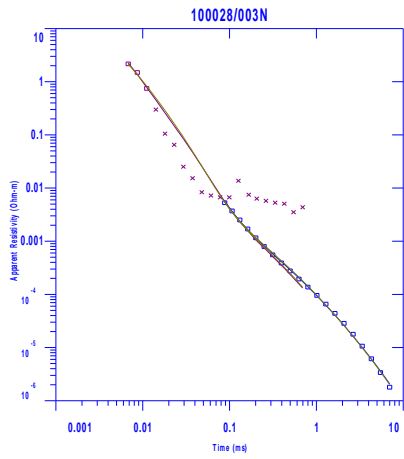
LAYER	RESISTIVITY	THICKNESS	DEPTH	ELEV
1	355.4	4.9	4.9	0.1
2	82.1	12.2	17.1	-12.1
3	7.8	28.0	45.2	-40.2
4	0.6			



DATASET: SND026X/003N

NORTH: 8879658 EAST: 611333.5 ELEV: 2.50

LAYER	RESISTIVITY	THICKNESS	DEPTH	ELEV
1	59.9	2.4	2.4	0.1
2	27.4	12.5	14.8	-12.3
3	9.3	34.0	48.9	-46.4
4	1.4			

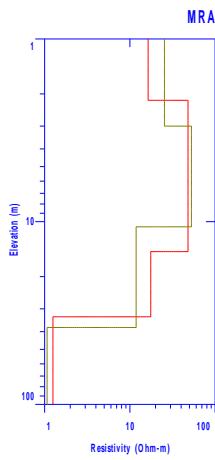
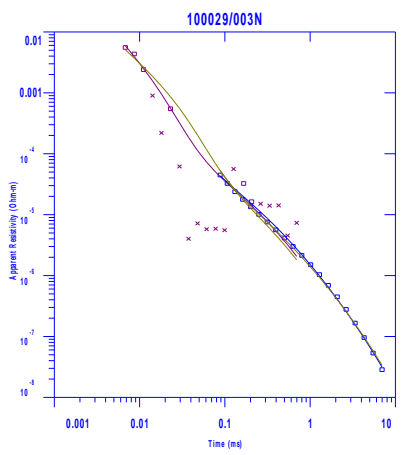


DATASET: SND026X/003N

NORTH: 8879658 EAST: 611333.5 ELEV: 2.50

LAYER RESISTIVITY THICKNESS DEPTH ELEV

LAYER	RESISTIVITY	THICKNESS	DEPTH	ELEV
1	59.9	2.4	2.4	0.1
2	27.4	12.5	14.8	-12.3
3	9.3	34.0	48.9	-46.4
4	1.4			

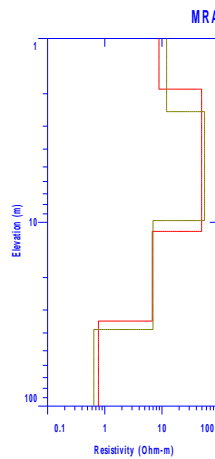
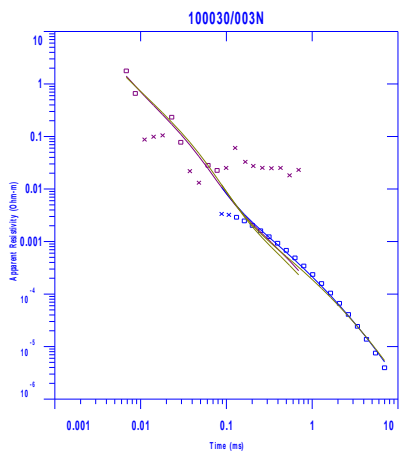


DATASET: SND029X/003N

NORTH: 8880286 EAST: 611003.8 ELEV: 2.50

LAYER RESISTIVITY THICKNESS DEPTH ELEV

LAYER	RESISTIVITY	THICKNESS	DEPTH	ELEV
1	16.4	2.2	2.2	0.3
2	48.1	12.4	14.6	-12.1
3	17.6	18.6	33.2	-30.7
4	1.3			

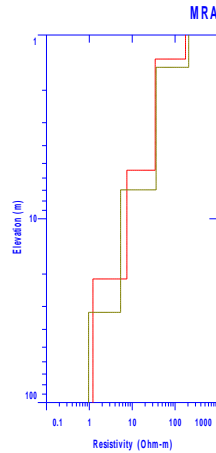
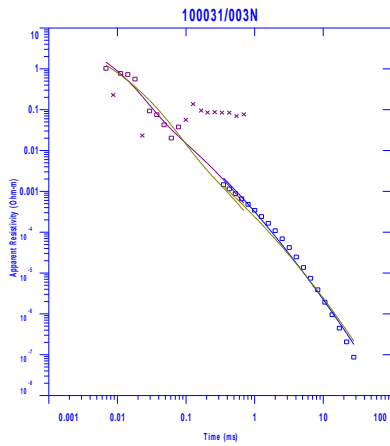


DATASET: SND030X/003N

NORTH: 8880597 EAST: 610741.7 ELEV: 2.00

LAYER RESISTIVITY THICKNESS DEPTH ELEV

LAYER	RESISTIVITY	THICKNESS	DEPTH	ELEV
1	8.9	1.9	1.9	0.1
2	49.5	9.3	11.2	-9.2
3	6.8	23.3	34.5	-32.5
4	0.8			

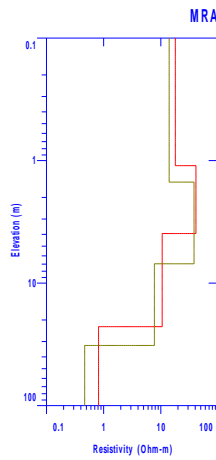
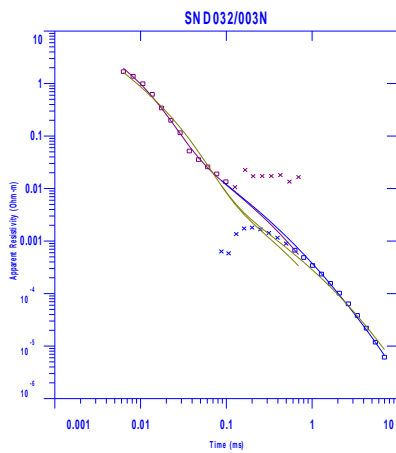


DATASET: SND031X/003N

NORTH: 8880840 EAST: 610746 ELEV: 1.50

LAYER RESISTIVITY THICKNESS DEPTH ELEV

LAYER	RESISTIVITY	THICKNESS	DEPTH	ELEV
1	175.2	1.4	1.4	0.1
2	34.5	4.1	5.4	-3.9
3	7.5	15.8	21.3	-19.8
4	1.2			

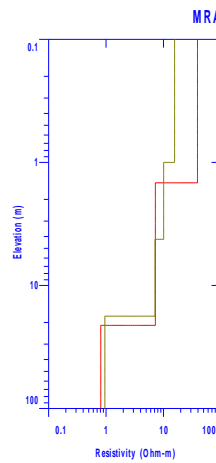
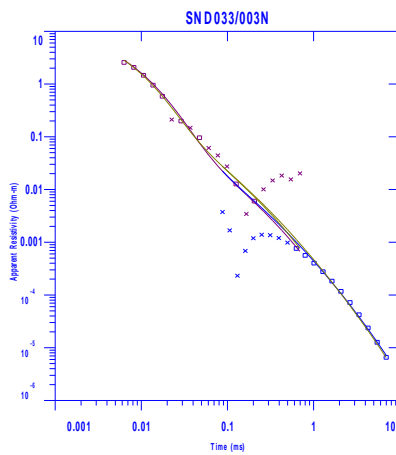


DATASET: SND032X/003N

NORTH: 8880895 EAST: 610241 ELEV: 1.50

LAYER RESISTIVITY THICKNESS DEPTH ELEV

LAYER	RESISTIVITY	THICKNESS	DEPTH	ELEV
1	18.0	1.1	1.1	0.4
2	41.3	2.8	3.9	-2.4
3	10.6	18.8	22.7	-21.2
4	0.8			

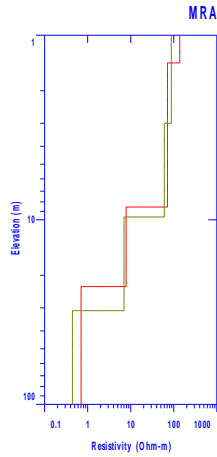
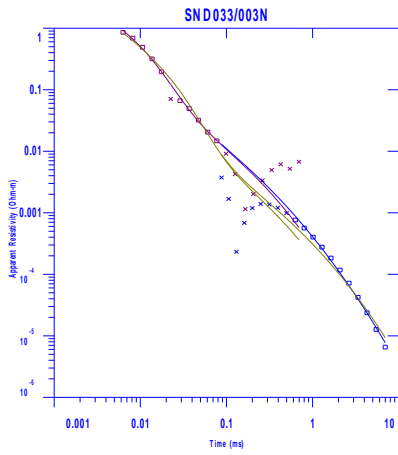


DATASET: SND033X/003N

NORTH: 8881103 EAST: 610453 ELEV: 1.50

LAYER RESISTIVITY THICKNESS DEPTH ELEV

LAYER	RESISTIVITY	THICKNESS	DEPTH	ELEV
1	39.2	1.5	1.5	0.0
2	7.2	19.6	21.1	-19.6
3	0.8			

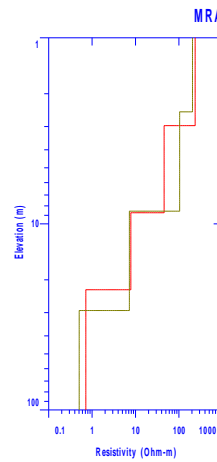
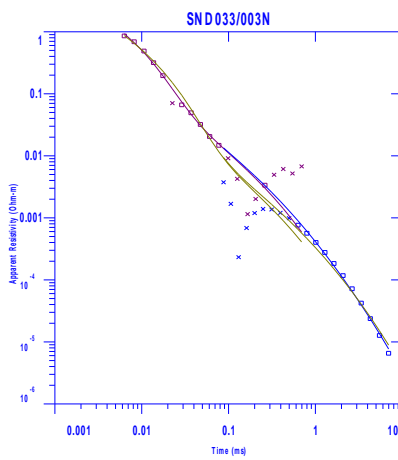


DATASET: SND033XA/003N

NORTH: 8881103 EAST: 610453 ELEV: 1.50

LAYER RESISTIVITY THICKNESS DEPTH ELEV

LAYER	RESISTIVITY	THICKNESS	DEPTH	ELEV
1	137.3	1.4	1.4	0.1
2	71.5	7.1	8.5	-7.0
3	7.8	14.5	23.0	-21.5
4	0.7			



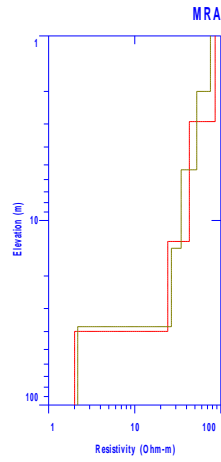
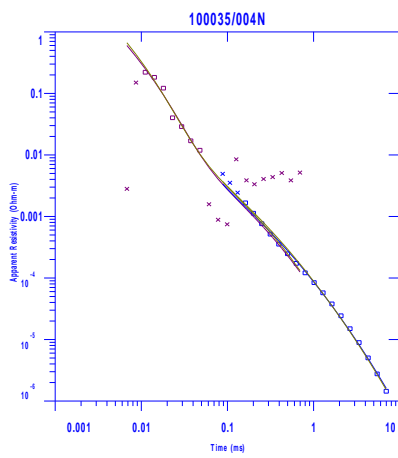
DATASET: SND033XX/003N

NORTH: 8881103 EAST: 610453 ELEV: 1.50

LAYER RESISTIVITY THICKNESS DEPTH ELEV

LAYER	RESISTIVITY	THICKNESS	DEPTH	ELEV
1	236.3	3.0	3.0	-1.5
2	45.6	5.7	8.7	-7.2
3	7.8	13.9	22.6	-21.1
4	0.7			

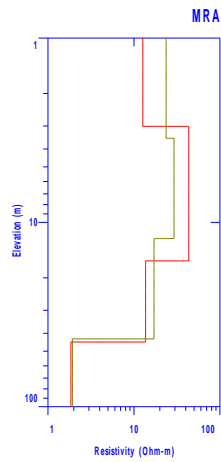
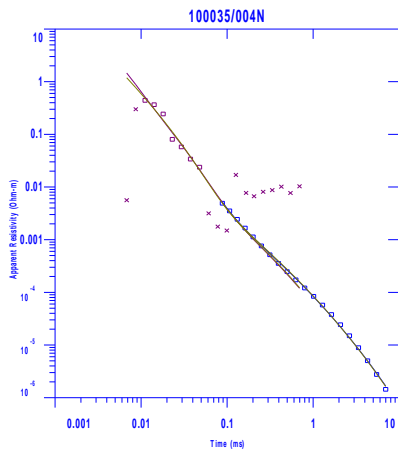
6.4 Line 4



DATASET: SND035X/004N

NORTH: 8879765 EAST: 611738.8 ELEV: 3.00

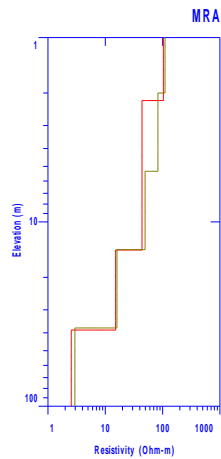
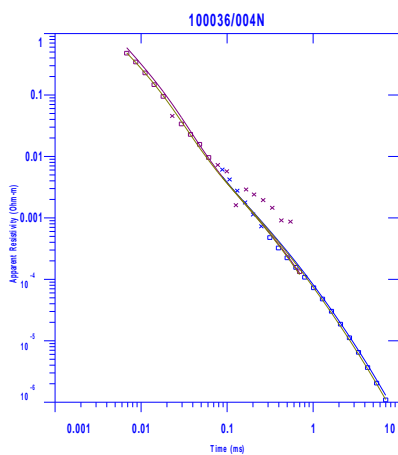
LAYER	RESISTIVITY	THICKNESS	DEPTH	ELEV
1	85.9	2.9	2.9	0.1
2	43.1	10.1	13.0	-10.0
3	24.2	26.9	39.9	-36.9
4	2.0			



DATASET: SND035XX/004N

NORTH: 8879765 EAST: 611738.8 ELEV: 3.00

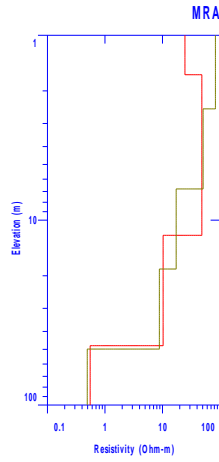
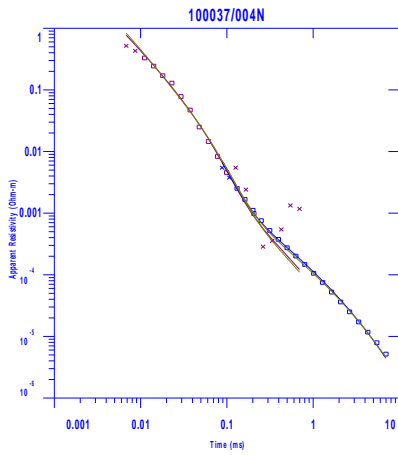
LAYER	RESISTIVITY	THICKNESS	DEPTH	ELEV
1	12.7	3.0	3.0	0.0
2	43.4	13.2	16.2	-13.2
3	13.7	28.4	44.6	-41.6
4	1.8			



DATASET: SND036X/004N

NORTH: 8879983 EAST: 611708.6 ELEV: 2.50

LAYER	RESISTIVITY	THICKNESS	DEPTH	ELEV
1	103.2	2.2	2.2	0.3
2	43.7	12.0	14.2	-11.7
3	15.1	24.4	38.6	-36.1
4	2.6			

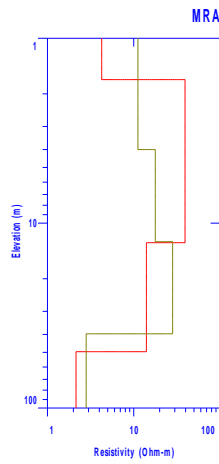
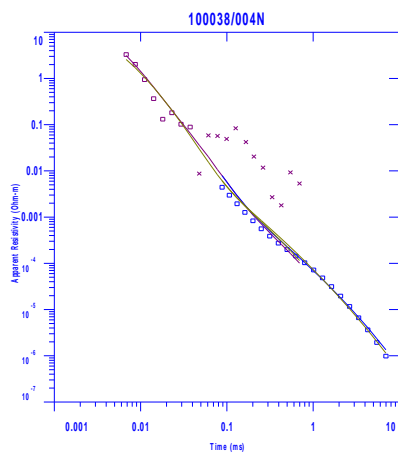


DATASET: SND037X/004N

NORTH: 8880156 EAST: 611589 ELEV: 2.00

LAYER RESISTIVITY THICKNESS DEPTH ELEV

LAYER	RESISTIVITY	THICKNESS	DEPTH	ELEV
1	24.6	1.6	1.6	0.4
2	48.5	10.4	12.1	-10.1
3	10.3	35.7	47.8	-45.8
4	0.6			

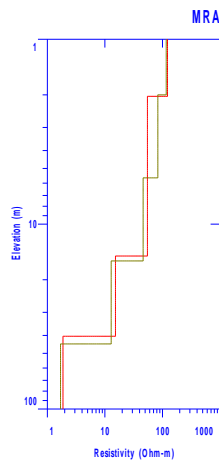
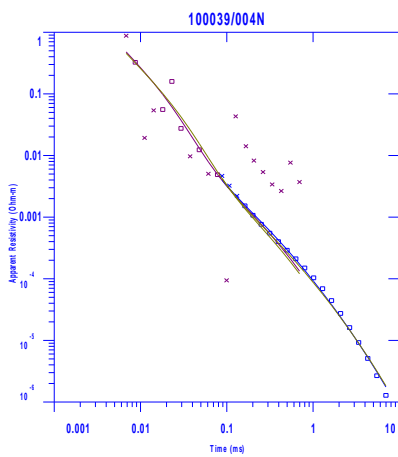


DATASET: SND038X/004N

NORTH: 8880295 EAST: 611401.8 ELEV: 2.00

LAYER RESISTIVITY THICKNESS DEPTH ELEV

LAYER	RESISTIVITY	THICKNESS	DEPTH	ELEV
1	4.3	1.7	1.7	0.3
2	39.4	11.1	12.8	-10.8
3	14.1	36.8	49.6	-47.6
4	2.1			

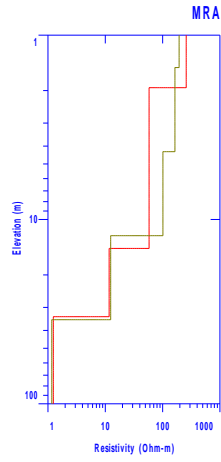
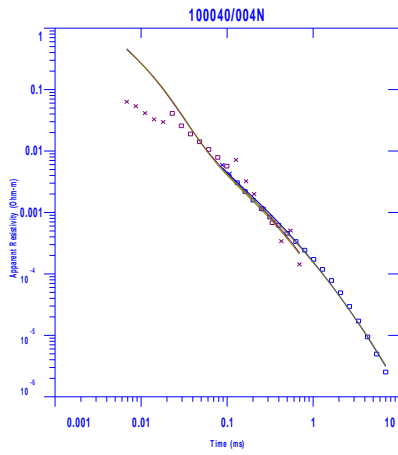


DATASET: SND039/004N

NORTH: 8880519 EAST: 611394.8 ELEV: 2.00

LAYER RESISTIVITY THICKNESS DEPTH ELEV

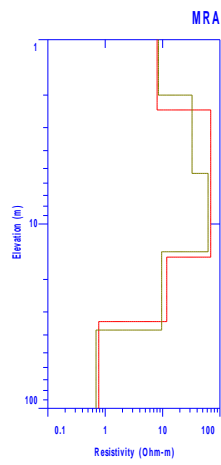
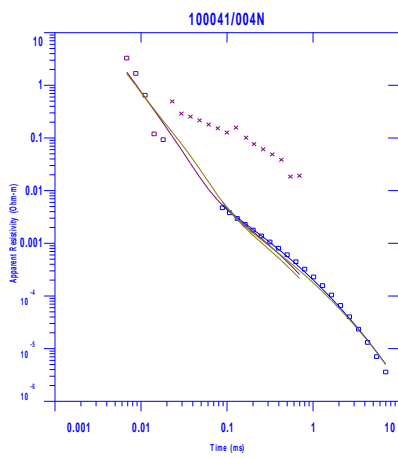
LAYER	RESISTIVITY	THICKNESS	DEPTH	ELEV
1	122.6	2.0	2.0	0.0
2	54.8	12.8	14.9	-12.9
3	15.2	25.5	40.4	-38.4
4	1.9			



DATASET: SND040/004N

NORTH: 8880702 EAST: 611286 n ELEV: 2.00

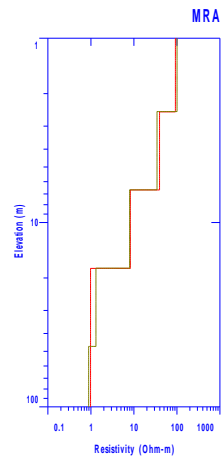
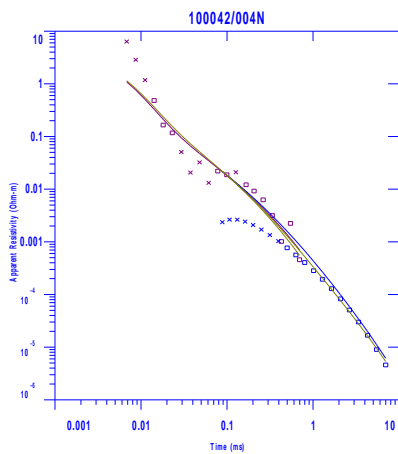
LAYER	RESISTIVITY	THICKNESS	DEPTH	ELEV
1	258.4	1.9	1.9	0.1
2	58.1	12.4	14.4	-12.4
3	11.7	19.3	33.7	-31.7
4	1.2			



DATASET: SND041/004N

NORTH: 8880959 EAST: 611207 ELEV: 2.50

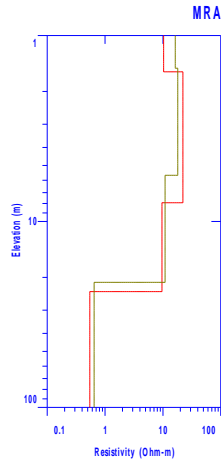
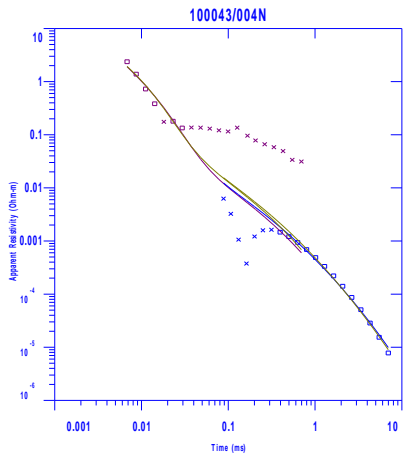
LAYER	RESISTIVITY	THICKNESS	DEPTH	ELEV
1	8.0	2.4	2.4	0.1
2	69.0	12.7	15.1	-12.6
3	11.8	18.7	33.8	-31.3
4	0.8			



DATASET: SND042/004N

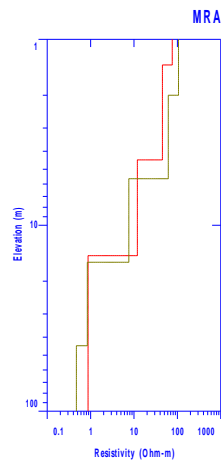
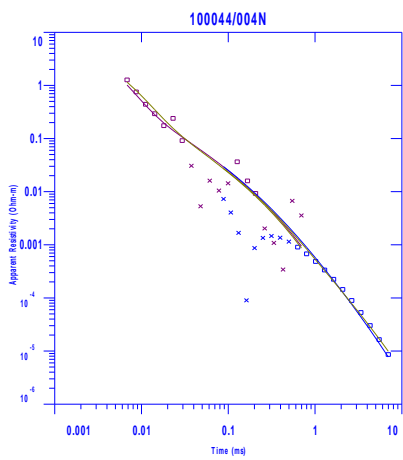
NORTH: 8881094 EAST: 611107 ELEV: 2.50

LAYER	RESISTIVITY	THICKNESS	DEPTH	ELEV
1	91.8	2.5	2.5	0.0
2	39.4	4.1	6.7	-4.2
3	8.3	11.1	17.8	-15.3
4	1.0			



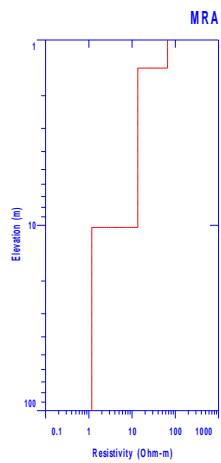
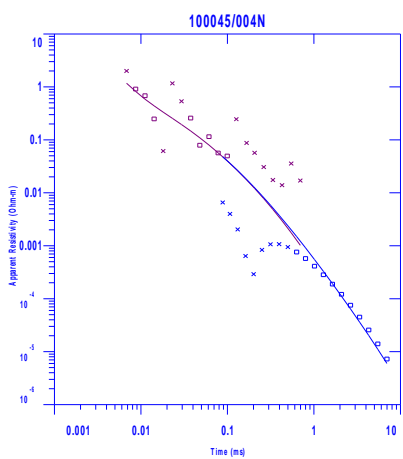
DATASET: SND043/004N
 NORTH: 8881250 EAST: 610898.6 ELEV: 1.50

LAYER	RESISTIVITY	THICKNESS	DEPTH	ELEV
1	10.3	1.6	1.6	-0.1
2	22.1	6.4	7.9	-6.4
3	9.6	15.9	23.8	-22.3
4	0.5			



DATASET: SND044/004N
 NORTH: 8881458 EAST: 610853.7 ELEV: 2.00

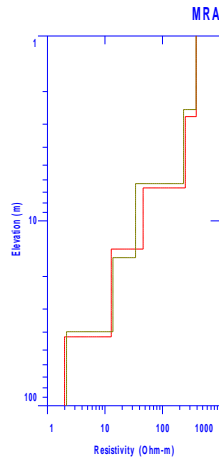
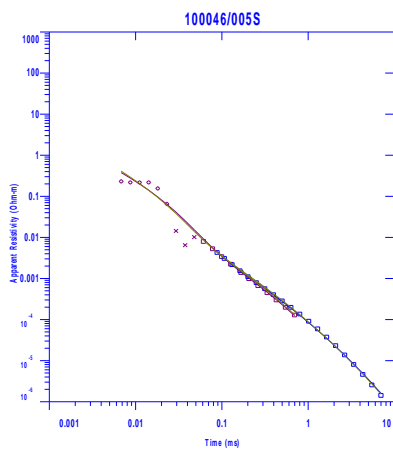
LAYER	RESISTIVITY	THICKNESS	DEPTH	ELEV
1	76.1	1.4	1.4	0.6
2	45.3	3.1	4.5	-2.5
3	12.0	10.1	14.6	-12.6
4	0.9			



DATASET: SND045/004N
 NORTH: 8881575 EAST: 610722.2 ELEV: 1.50

LAYER	RESISTIVITY	THICKNESS	DEPTH	ELEV
1	66.0	1.4	1.4	0.1
2	13.6	8.8	10.3	-8.8
3	1.2			

6.5 Line 5

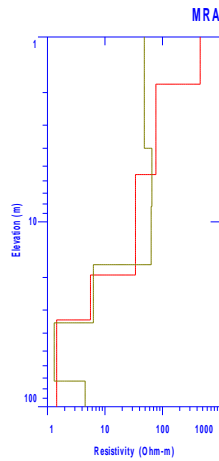
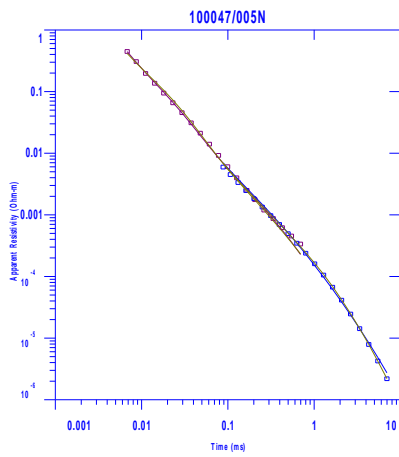


DATASET: SND046Z/005N

NORTH: 8879891 EAST: 612151 ELEV: 7.00

LAYER RESISTIVITY THICKNESS DEPTH ELEV

LAYER	RESISTIVITY	THICKNESS	DEPTH	ELEV
1	386.7	2.7	2.7	4.3
2	249.4	3.9	6.6	0.4
3	46.1	7.6	14.2	-7.2
4	12.9	28.2	42.4	-35.4
5	2.0			

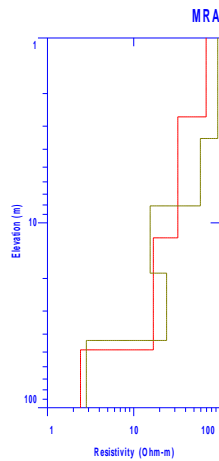
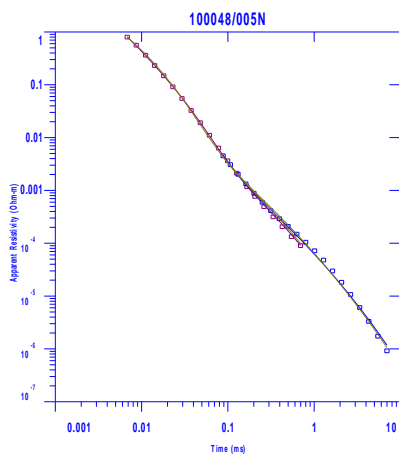


DATASET: SND047Z/005N

NORTH: 8879936 EAST: 612367.31 ELEV: 6.00

LAYER RESISTIVITY THICKNESS DEPTH ELEV

LAYER	RESISTIVITY	THICKNESS	DEPTH	ELEV
1	452.8	1.8	1.8	4.2
2	77.1	3.8	5.6	0.4
3	34.0	13.8	19.4	-13.4
4	5.6	14.5	33.9	-27.9
5	1.5			

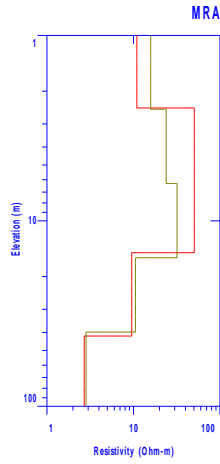
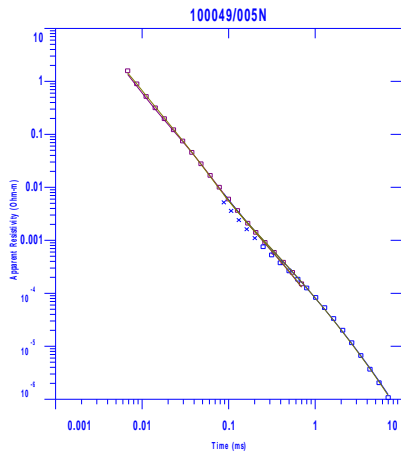


DATASET: SND048Z/005N

NORTH: 8880229 EAST: 612121.9 ELEV: 3.00

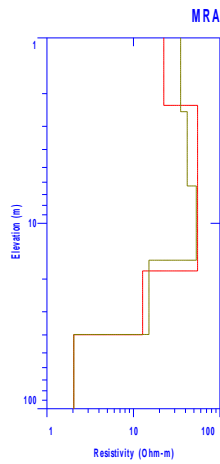
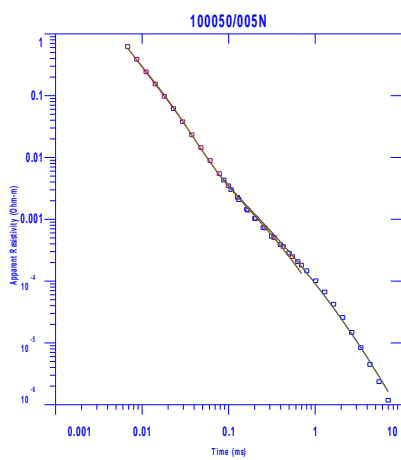
LAYER RESISTIVITY THICKNESS DEPTH ELEV

LAYER	RESISTIVITY	THICKNESS	DEPTH	ELEV
1	69.1	2.7	2.7	0.3
2	32.5	9.4	12.0	-9.0
3	16.9	36.6	48.6	-45.6
4	2.4			



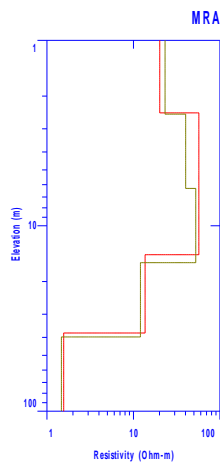
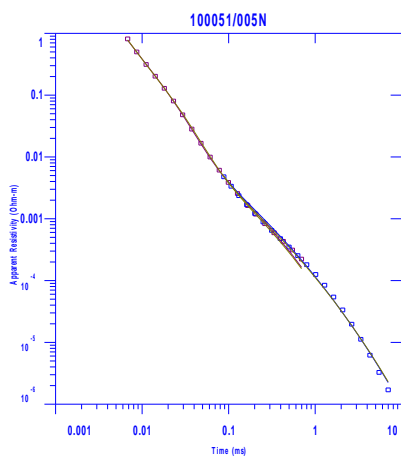
DATASET: SND049Z/005N
 NORTH: 8880526 EAST: 611905.9 ELEV: 2.50

LAYER	RESISTIVITY	THICKNESS	DEPTH	ELEV
1	11.0	2.5	2.5	0.0
2	50.5	12.4	14.9	-12.4
3	9.6	27.0	41.8	-39.3
4	2.7			



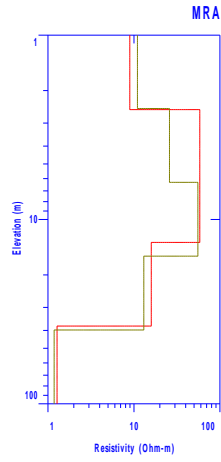
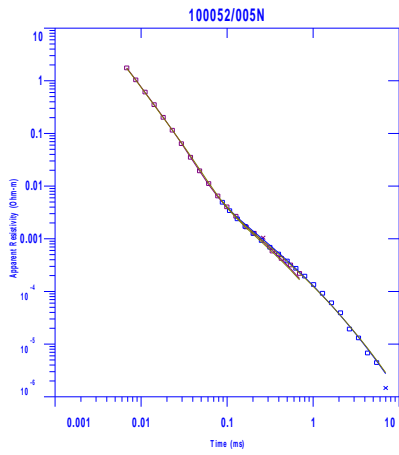
DATASET: SND050Z/005N
 NORTH: 8880644 EAST: 611850.6 ELEV: 2.50

LAYER	RESISTIVITY	THICKNESS	DEPTH	ELEV
1	22.4	2.3	2.3	0.2
2	55.2	15.8	18.1	-15.6
3	12.8	21.9	39.9	-37.4
4	2.0			



DATASET: SND051Z/005N
 NORTH: 8880826 EAST: 611750 ELEV: 2.50

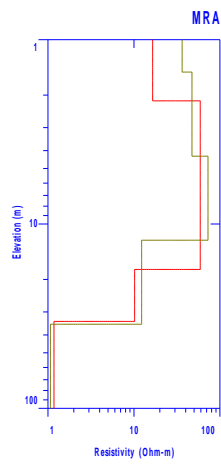
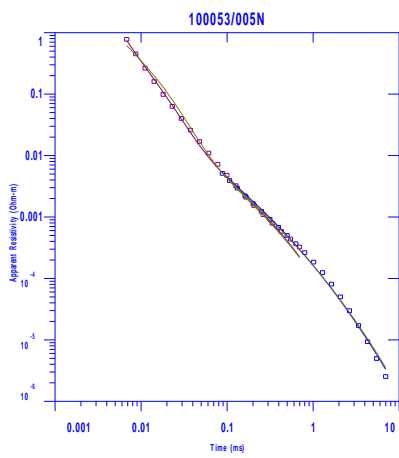
LAYER	RESISTIVITY	THICKNESS	DEPTH	ELEV
1	20.1	2.5	2.5	0.0
2	57.0	11.9	14.3	-11.8
3	13.7	23.5	37.9	-35.4
4	1.6			



DATASET: SND052Z/005N

NORTH: 8880987 EAST: 611674 ELEV: 2.50

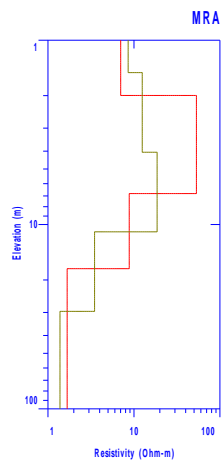
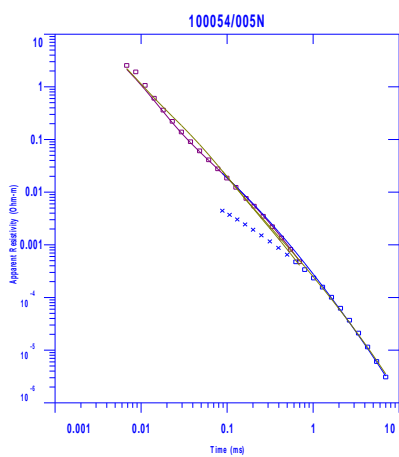
LAYER	RESISTIVITY	THICKNESS	DEPTH	ELEV
1	8.9	2.5	2.5	0.0
2	58.3	10.8	13.3	-10.8
3	15.9	24.6	37.9	-35.4
4	1.3			



DATASET: SND053Z/005N

NORTH: 8881157 EAST: 611574.8 ELEV: 2.00

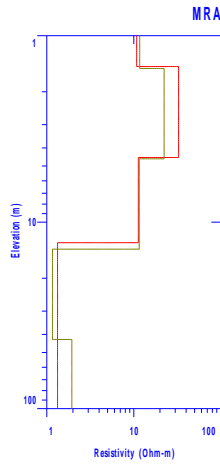
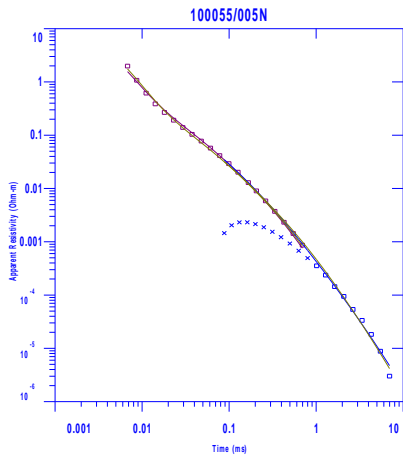
LAYER	RESISTIVITY	THICKNESS	DEPTH	ELEV
1	16.5	2.1	2.1	-0.1
2	59.1	15.5	17.7	-15.7
3	10.2	16.1	33.8	-31.8
4	1.2			



DATASET: SND054Z/005N

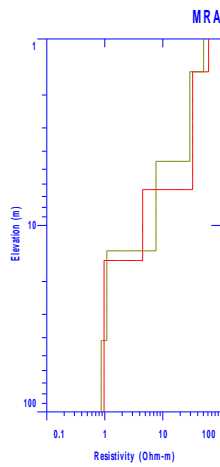
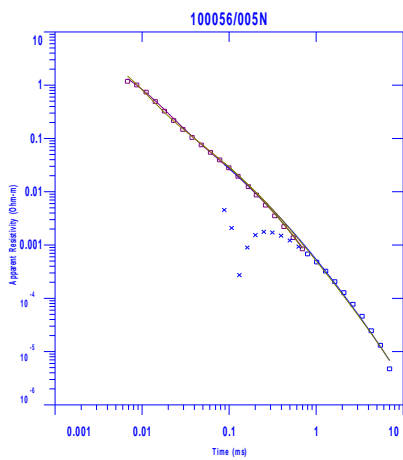
NORTH: 8881339 EAST: 611500.6 ELEV: 2.00

LAYER	RESISTIVITY	THICKNESS	DEPTH	ELEV
1	7.0	2.0	2.0	0.0
2	53.2	4.8	6.8	-4.8
3	8.8	10.6	17.4	-15.4
4	1.7			



DATASET: SND055Z/005N
 NORTH: 8881571 EAST: 611401.3 ELEV: 1.50

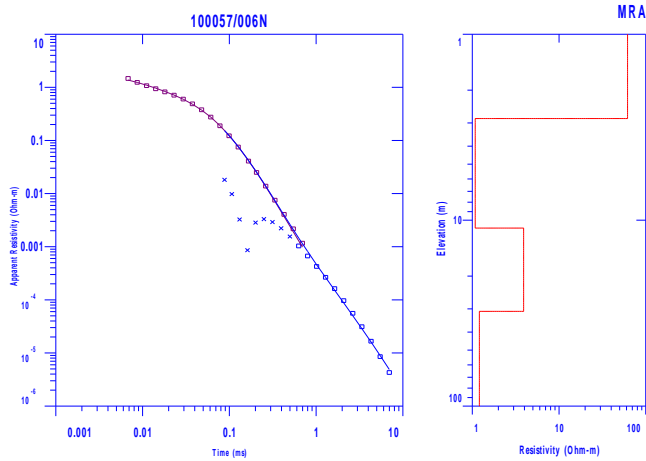
LAYER	RESISTIVITY	THICKNESS	DEPTH	ELEV
1	10.8	1.5	1.5	0.0
2	32.7	3.0	4.5	-3.0
3	11.3	8.4	12.9	-11.4
4	1.3			



DATASET: SND056Z/005N
 NORTH: 8881767 EAST: 611225.4 ELEV: 1.50

LAYER	RESISTIVITY	THICKNESS	DEPTH	ELEV
1	61.5	1.5	1.5	0.0
2	32.8	4.9	6.4	-4.9
3	4.5	9.0	15.4	-13.9
4	1.0			

6.6 Line 6

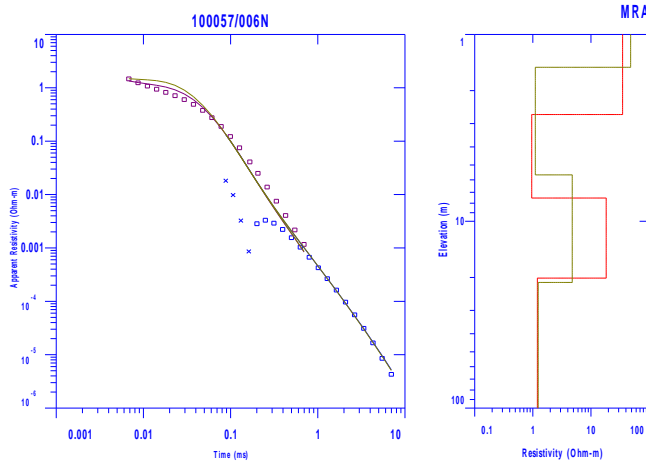


DATASET: SND057/006N

NORTH: 8880348 EAST: 612737 ELEV: 3.00

LAYER RESISTIVITY THICKNESS DEPTH ELEV

Layer	Resistivity	Thickness	Depth	Elev
1	61.6	2.8	2.8	0.2
2	1.1	8.2	11.0	-8.0
3	3.9	19.9	30.9	-27.9
4	1.2			

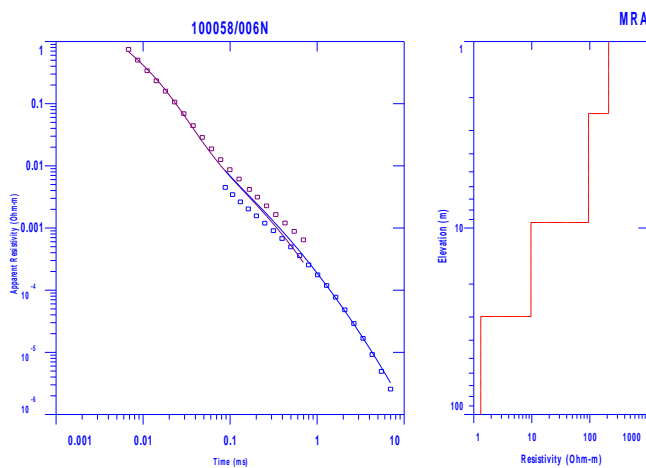


DATASET: SND057X/006N

NORTH: 8880348 EAST: 612736.8 ELEV: 3.00

LAYER RESISTIVITY THICKNESS DEPTH ELEV

Layer	Resistivity	Thickness	Depth	Elev
1	35.1	2.7	2.7	0.3
2	1.0	4.8	7.5	-4.5
3	18.3	12.6	20.2	-17.2
4	1.2			

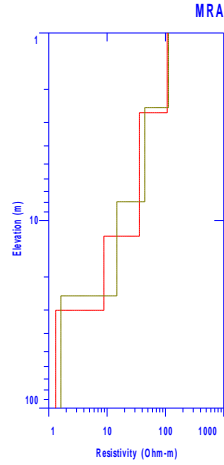
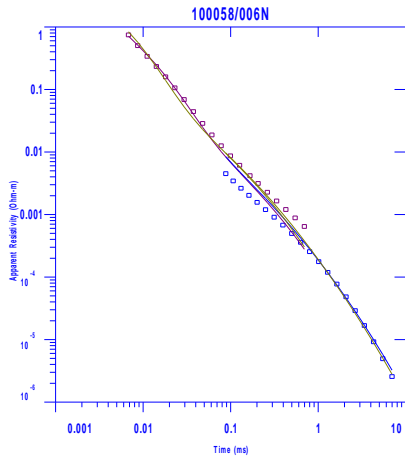


DATASET: SND058X/006N

NORTH: 8880532 EAST: 612633.8 ELEV: 3.00

LAYER RESISTIVITY THICKNESS DEPTH ELEV

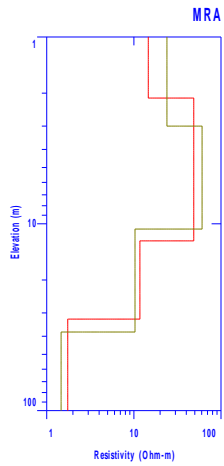
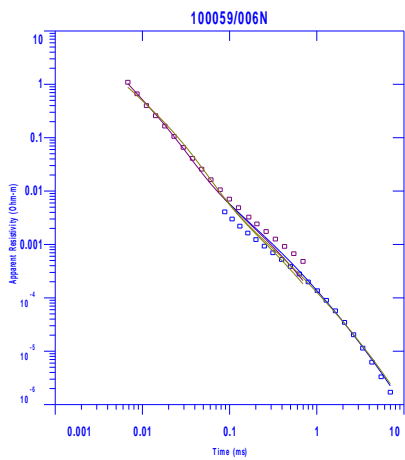
Layer	Resistivity	Thickness	Depth	Elev
1	211.3	2.4	2.4	0.6
2	55.2	6.9	9.3	-6.3
3	9.7	20.5	29.8	-26.8
4	1.3			



DATASET: SND058XX/006N

NORTH: 8880532 EAST: 612633.8 ELEV: 3.00

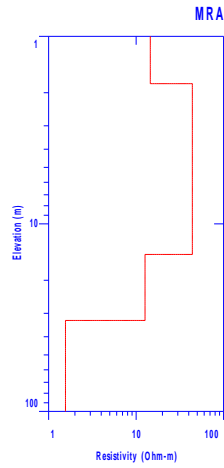
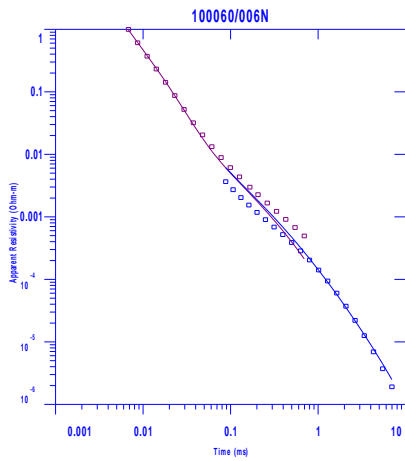
LAYER	RESISTIVITY	THICKNESS	DEPTH	ELEV
1	107.4	2.7	2.7	0.3
2	35.9	9.5	12.1	-9.1
3	8.8	18.0	30.1	-27.1
4	1.3			



DATASET: SND059X/006N

NORTH: 8880748 EAST: 612528.3 ELEV: 2.50

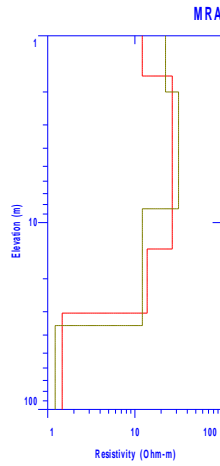
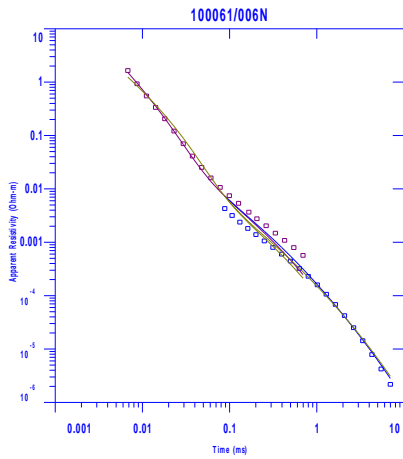
LAYER	RESISTIVITY	THICKNESS	DEPTH	ELEV
1	14.7	2.1	2.1	0.4
2	48.7	10.2	12.3	-9.8
3	11.7	20.0	32.4	-29.9
4	1.7			



DATASET: SND060X/006N

NORTH: 8880917 EAST: 612435 ELEV: 2.00

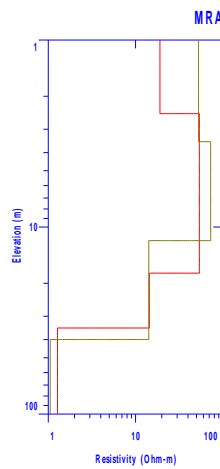
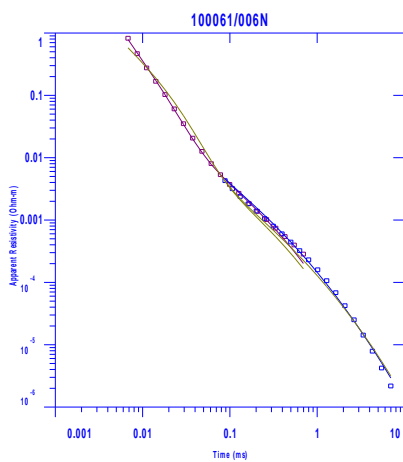
LAYER	RESISTIVITY	THICKNESS	DEPTH	ELEV
1	14.5	1.8	1.8	0.2
2	43.9	12.8	14.6	-12.6
3	12.6	18.2	32.7	-30.7
4	1.6			



DATASET: SND061X/006N

NORTH: 8881127 EAST: 612329.4 ELEV: 2.00

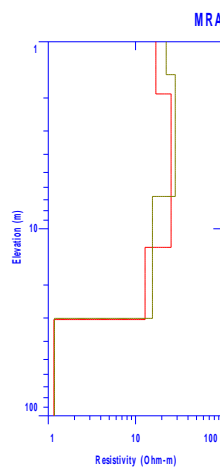
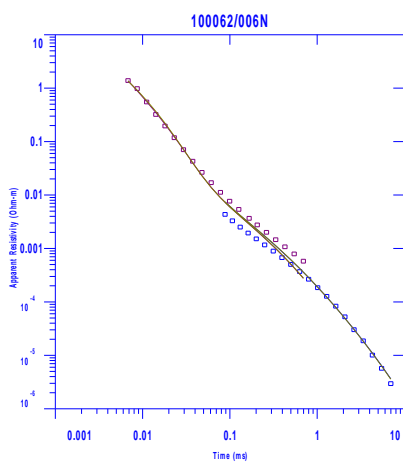
LAYER	RESISTIVITY	THICKNESS	DEPTH	ELEV
1	12.2	1.6	1.6	0.4
2	26.8	12.2	13.9	-11.9
3	13.8	16.7	30.5	-28.5
4	1.5			



DATASET: SND061XX/006N

NORTH: 8881127 EAST: 612329.4 ELEV: 2.50

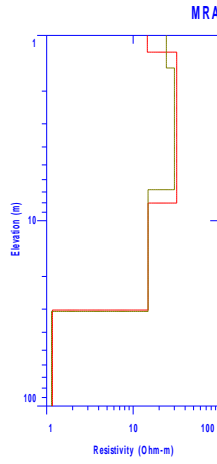
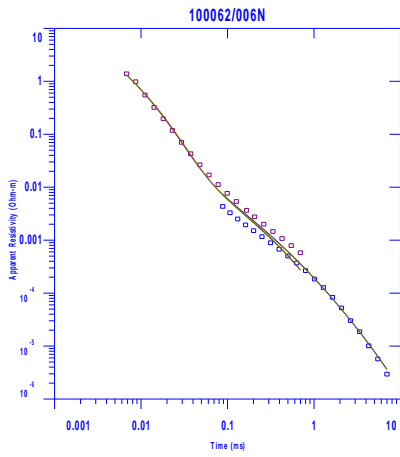
LAYER	RESISTIVITY	THICKNESS	DEPTH	ELEV
1	19.1	2.5	2.5	0.0
2	53.9	15.2	17.6	-15.1
3	14.4	17.0	34.7	-32.2
4	1.3			



DATASET: SND062X/006N

NORTH: 8881246 EAST: 612250.6 ELEV: 2.00

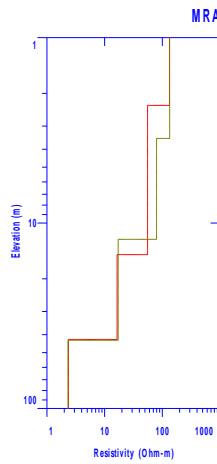
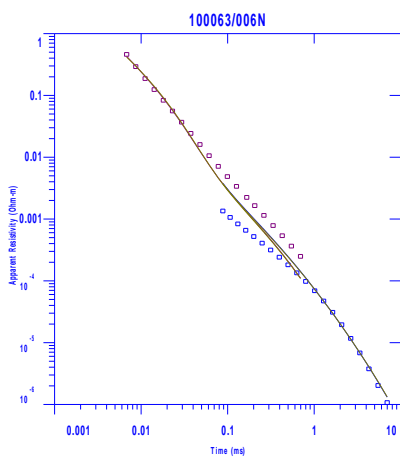
LAYER	RESISTIVITY	THICKNESS	DEPTH	ELEV
1	17.1	1.9	1.9	0.1
2	25.6	10.7	12.6	-10.6
3	12.9	18.0	30.6	-28.6
4	1.2			



DATASET: SND062XX/006N

NORTH: 8881246 EAST: 612250.6 ELEV: 1.50

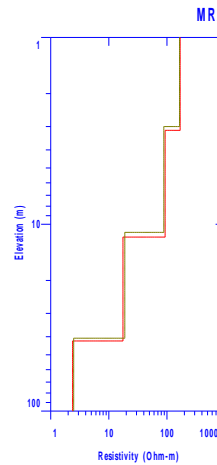
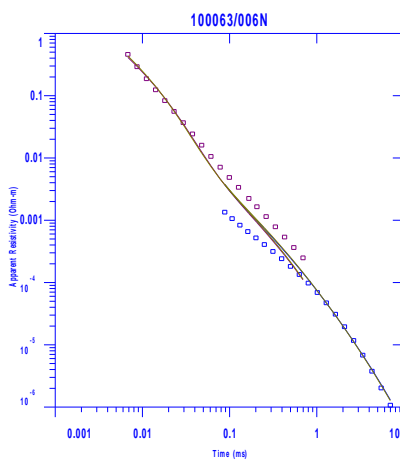
LAYER	RESISTIVITY	THICKNESS	DEPTH	ELEV
1	14.6	1.2	1.2	0.3
2	31.9	6.8	8.0	-6.5
3	14.9	22.3	30.4	-28.9
4	1.2			



DATASET: SND063X/006N

NORTH: 8881468 EAST: 612147 ELEV: 2.50

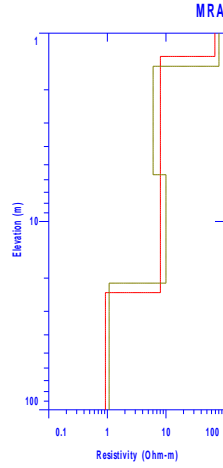
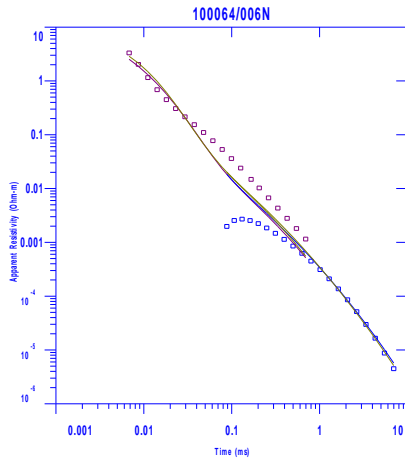
LAYER	RESISTIVITY	THICKNESS	DEPTH	ELEV
1	133.4	2.3	2.3	0.2
2	55.7	12.5	14.8	-12.3
3	16.5	27.6	42.4	-39.9
4	2.4			



DATASET: SND063XX/006N

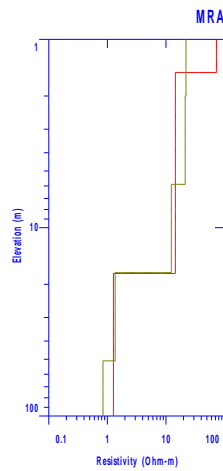
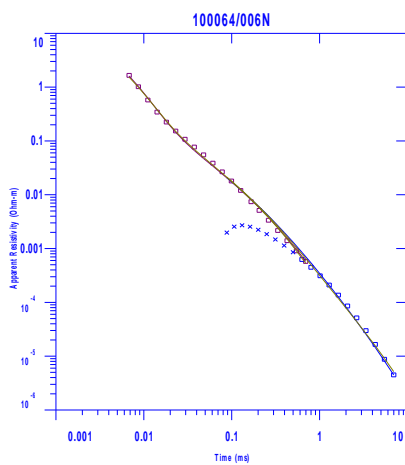
NORTH: 8881468 EAST: 612147 ELEV: 3.00

LAYER	RESISTIVITY	THICKNESS	DEPTH	ELEV
1	169.2	3.1	3.1	-0.1
2	93.2	8.6	11.7	-8.7
3	17.5	30.4	42.1	-39.1
4	2.4			



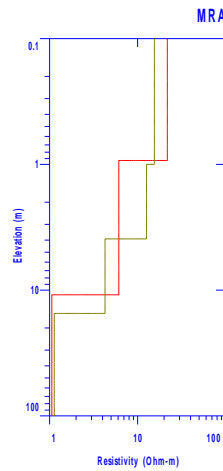
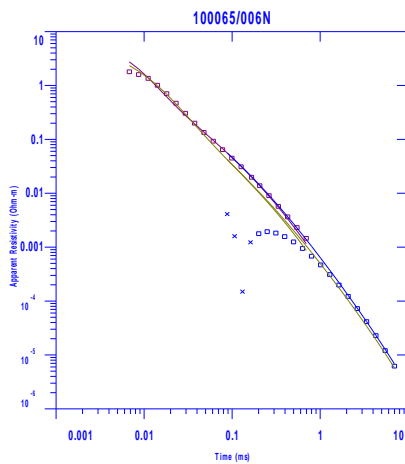
DATASET: SND064X/006N
 NORTH: 8881664 EAST: 612034.50 ELEV: 1.50

LAYER	RESISTIVITY	THICKNESS	DEPTH	ELEV
1	68.4	1.3	1.3	0.2
2	8.0	22.5	23.9	-22.4
3	0.9			



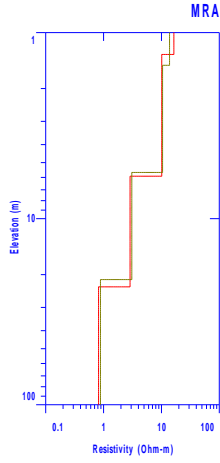
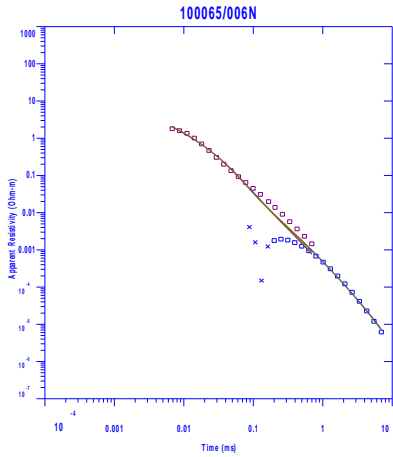
DATASET: SND064XX/006N
 NORTH: 8881664 EAST: 612034.5 ELEV: 1.50

LAYER	RESISTIVITY	THICKNESS	DEPTH	ELEV
1	72.9	1.5	1.5	0.0
2	14.5	16.0	17.5	-16.0
3	1.3			



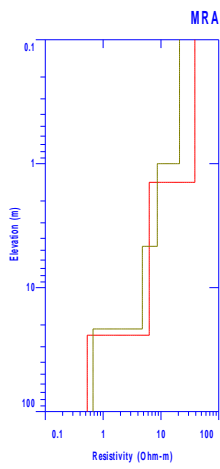
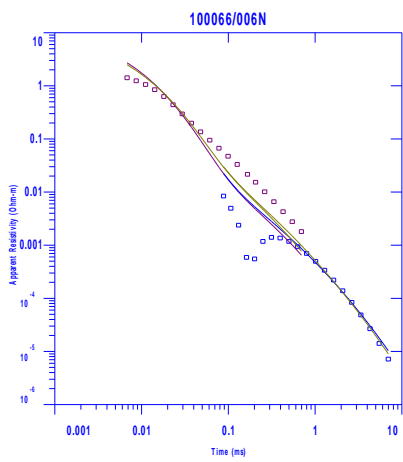
DATASET: SND065X/006N
 NORTH: 8881843 EAST: 611969.8 ELEV: 1.00

LAYER	RESISTIVITY	THICKNESS	DEPTH	ELEV
1	21.8	0.9	0.9	0.1
2	6.1	10.0	10.9	-9.9
3	1.1			



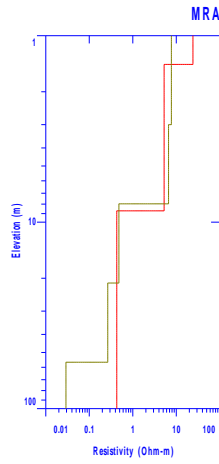
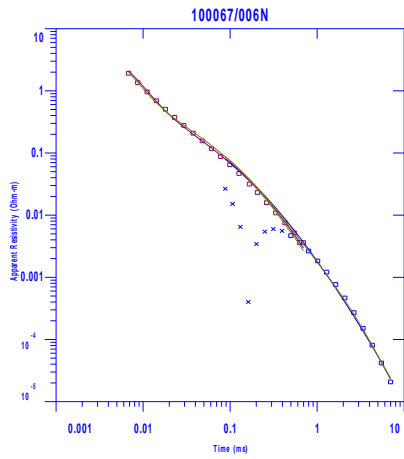
DATASET: SND065XX/006N
 NORTH: 8881843 EAST: 611969.8 ELEV: 1.50

LAYER	RESISTIVITY	THICKNESS	DEPTH	ELEV
1	16.4	1.3	1.3	0.2
2	10.1	4.6	5.9	-4.4
3	2.9	17.3	23.3	-21.8
4	0.8			



DATASET: SND066X/006N
 NORTH: 8882399 EAST: 611727 ELEV: 1.50

LAYER	RESISTIVITY	THICKNESS	DEPTH	ELEV
1	38.5	1.4	1.4	0.1
2	6.3	22.8	24.2	-22.7
3	0.5			

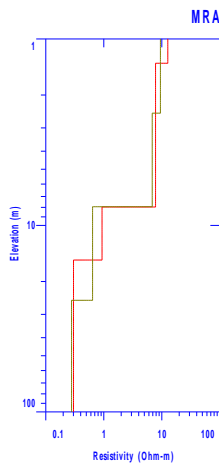
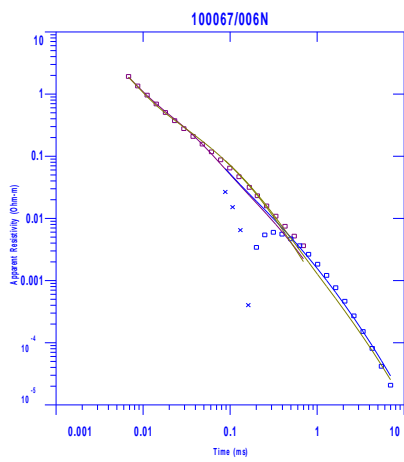


DATASET: SND066XX/006N

NORTH: 8882399 EAST: 611727 ELEV: 2.00

LAYER RESISTIVITY THICKNESS DEPTH ELEV

LAYER	RESISTIVITY	THICKNESS	DEPTH	ELEV
1	33.4	1.8	1.8	0.2
2	12.5	3.4	5.2	-3.2
3	4.9	19.4	24.6	-22.6
4	0.5			



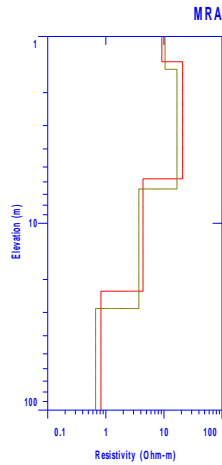
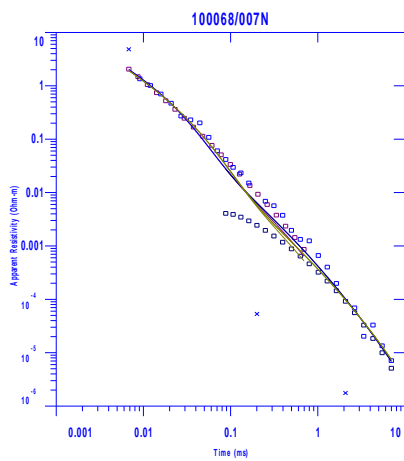
DATASET: SND067X/006N

NORTH: 8882587 EAST: 611453.6 ELEV: 1.50

AYER RESISTIVITY THICKNESS DEPTH ELEV

LAYER	RESISTIVITY	THICKNESS	DEPTH	ELEV
1	24.2	1.4	1.4	0.1
2	5.3	7.3	8.7	-7.2
3	0.4			

6.7 Line 7

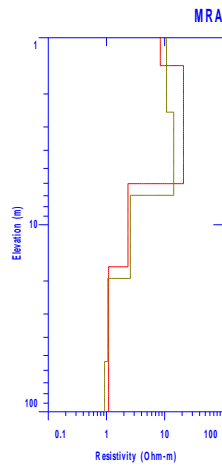
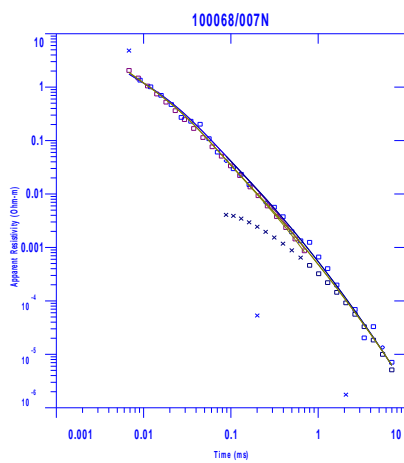


DATASET: SND068X/007N

NORTH: 8880574 EAST: 613381.4 ELEV: 1.50

LAYER RESISTIVITY THICKNESS DEPTH ELEV

LAYER	RESISTIVITY	THICKNESS	DEPTH	ELEV
1	9.2	1.4	1.4	0.1
2	21.0	4.4	5.8	-4.3
3	4.4	17.3	23.1	-21.6
4	0.8			

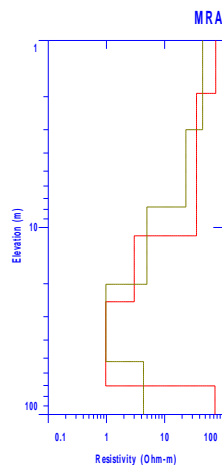
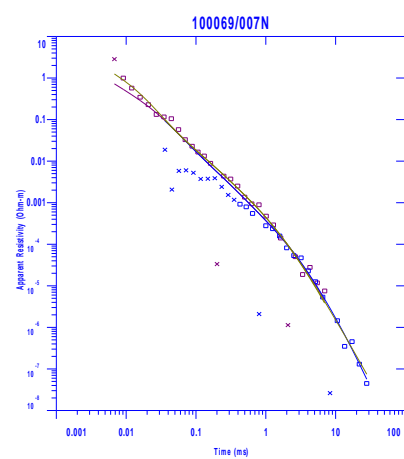


DATASET: SND068XX/007N

NORTH: 8880574 EAST: 613381.4 ELEV: 1.50

LAYER RESISTIVITY THICKNESS DEPTH ELEV

LAYER	RESISTIVITY	THICKNESS	DEPTH	ELEV
1	8.4	1.4	1.4	0.1
2	21.1	4.6	6.0	-4.5
3	2.3	10.8	16.8	-15.3
4	1.1			

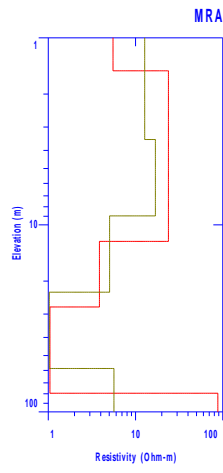
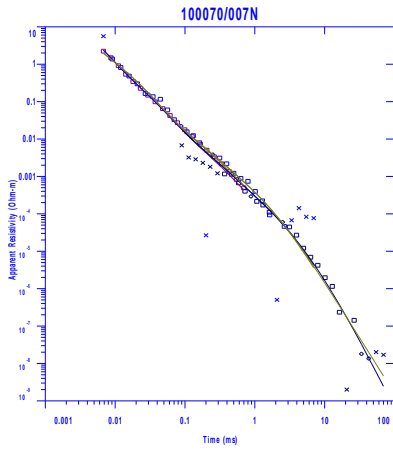


DATASET: SND069X/007N

NORTH: 8880779 EAST: 613235.2 ELEV: 2.00

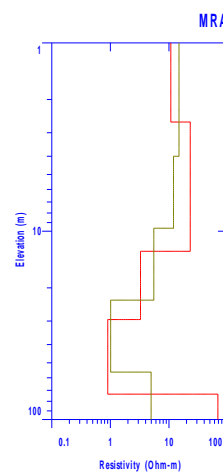
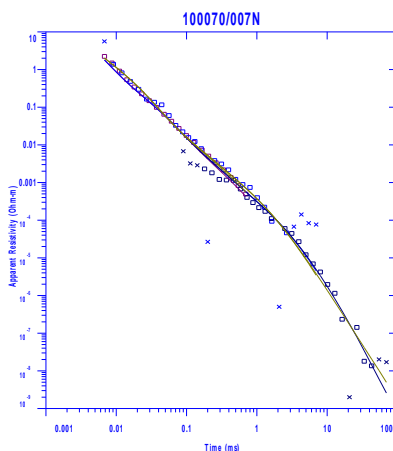
LAYER RESISTIVITY THICKNESS DEPTH ELEV

LAYER	RESISTIVITY	THICKNESS	DEPTH	ELEV
1	75.5	1.9	1.9	0.1
2	35.4	9.2	11.1	-9.1
3	3.0	13.9	25.0	-23.0
4	1.0	45.3	70.3	-68.3
5	73.3			



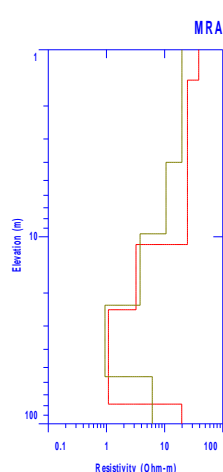
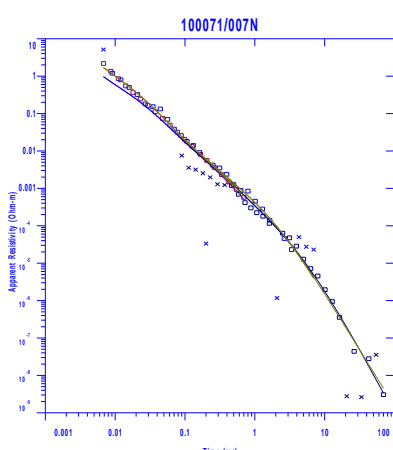
DATASET: SND070X/007N
 NORTH: 8880973 EAST: 613109.6 ELEV: 1.50

LAYER	RESISTIVITY	THICKNESS	DEPTH	ELEV
1	5.5	1.5	1.5	0.0
2	23.9	10.8	12.3	-10.8
3	3.9	15.2	27.5	-26.0
4	1.0	52.0	79.5	-78.0
5	87.9			



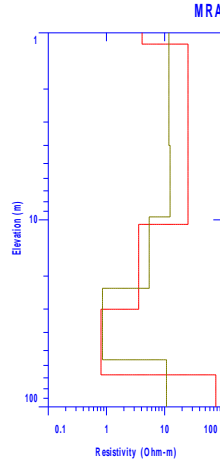
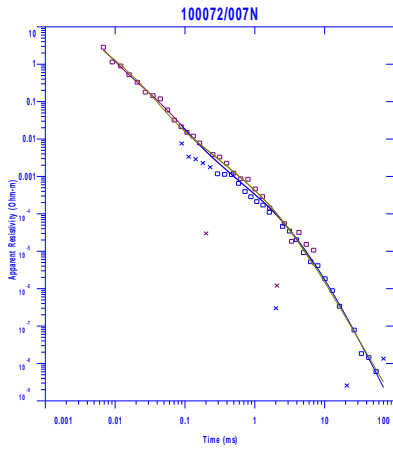
DATASET: SND070XX/007N
 NORTH: 8880973 EAST: 613109.6 ELEV: 2.00

LAYER	RESISTIVITY	THICKNESS	DEPTH	ELEV
1	10.8	2.6	2.6	-0.6
2	23.1	10.2	12.8	10.8
3	3.3	16.7	29.5	-27.5
4	0.9	43.9	73.4	-71.4
5	68.5			



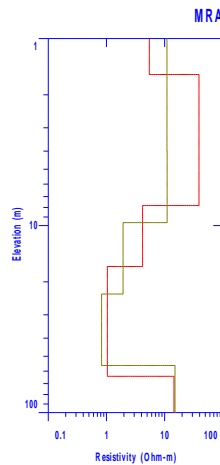
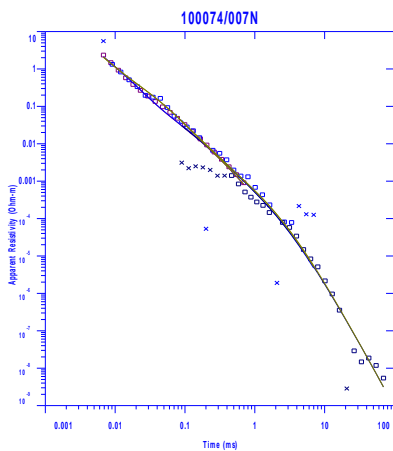
DATASET: SND071X/007N
 NORTH: 8881161 EAST: 613002 ELEV: 1.50

LAYER	RESISTIVITY	THICKNESS	DEPTH	ELEV
1	38.6	1.5	1.5	0.0
2	24.7	9.5	11.0	-9.5
3	3.2	13.6	24.6	-23.1
4	1.1	54.0	78.5	-77.0
5	19.7			



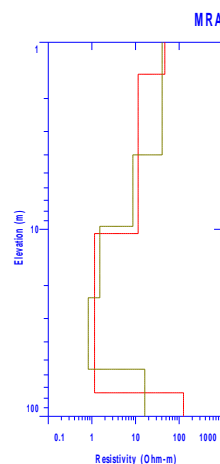
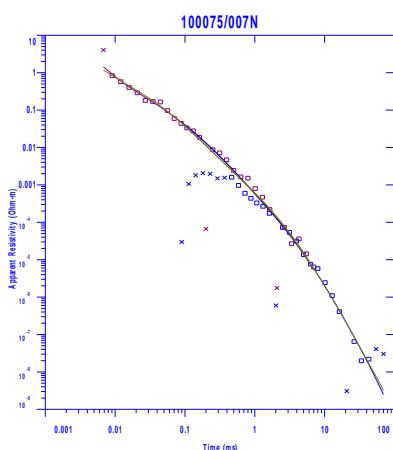
DATASET: SND072X/007N
 NORTH: 8881356 EAST: 612893.9 ELEV: 1.50

LAYER	RESISTIVITY	THICKNESS	DEPTH	ELEV
1	4.1	1.1	1.1	0.4
2	25.3	9.4	10.6	-9.1
3	3.6	19.5	30.1	-28.6
4	0.8	37.4	67.4	-65.9
5	75.8			



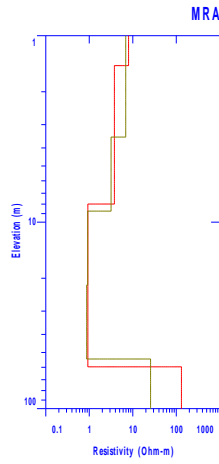
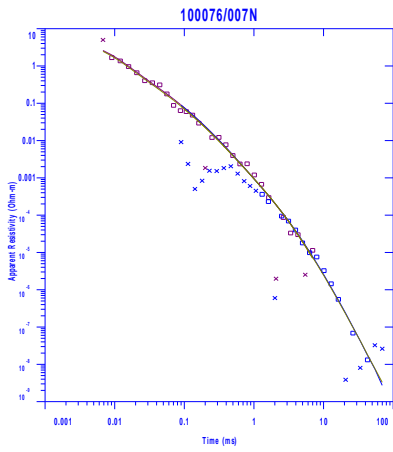
DATASET: SND074X/007N
 NORTH: 8881683 EAST: 612665.6 ELEV: 1.50

LAYER	RESISTIVITY	THICKNESS	DEPTH	ELEV
1	5.5	1.6	1.6	-0.1
2	39.1	6.3	7.8	-6.3
3	4.2	8.7	16.6	-15.1
4	1.0	47.4	64.0	-62.5
5	14.5			



DATASET: SND075X/007N
 NORTH: 8881917 EAST: 612614 ELEV: 1.50

LAYER	RESISTIVITY	THICKNESS	DEPTH	ELEV
1	47.1	1.5	1.5	0.0
2	11.5	9.1	10.5	-9.0
3	1.1	64.3	74.9	-73.4
4	125.9			

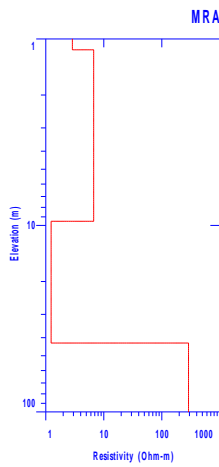
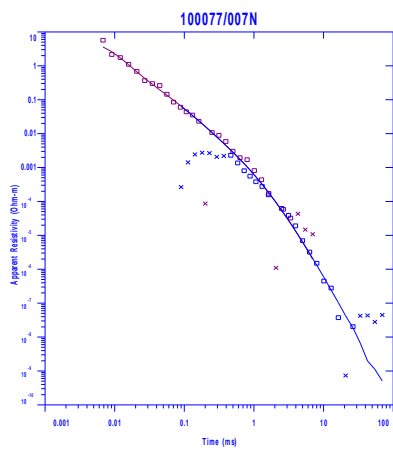


DATASET: SND076X/007N

NORTH: 8882216 EAST: 612449.8 ELEV: 1.50

LAYER RESISTIVITY THICKNESS DEPTH ELEV

LAYER	RESISTIVITY	THICKNESS	DEPTH	ELEV
1	8.0	1.4	1.4	0.1
2	3.8	6.5	8.0	-6.5
3	0.9	51.7	59.7	-58.2
4	131.6			

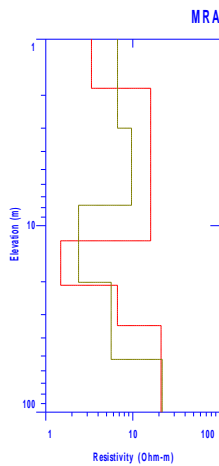
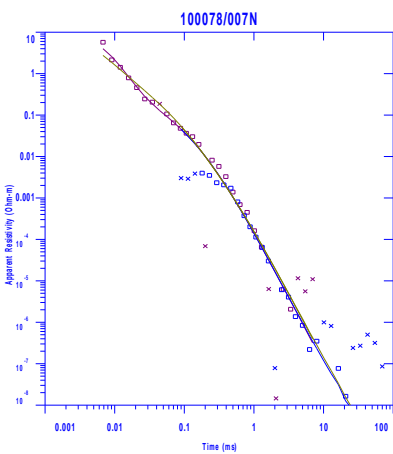


DATASET: SND077X/007N

NORTH: 8883379 EAST: 611883 ELEV: 1.50

LAYER RESISTIVITY THICKNESS DEPTH ELEV

LAYER	RESISTIVITY	THICKNESS	DEPTH	ELEV
1	2.9	1.1	1.1	0.4
2	6.7	8.4	9.5	-8.0
3	1.2	33.2	42.7	-41.2
4	289.0			

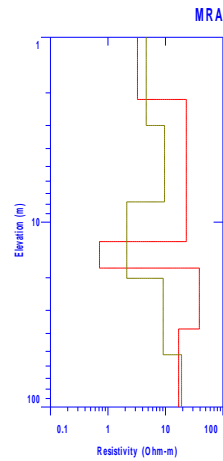
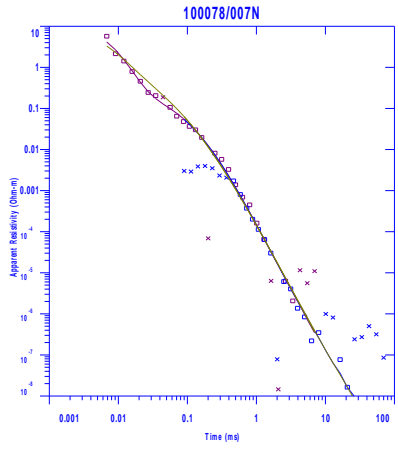


DATASET: SND078X/007N

NORTH: 8883538 EAST: 611550.3 ELEV: 2.00

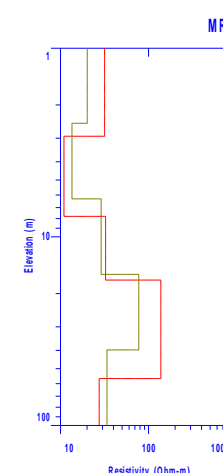
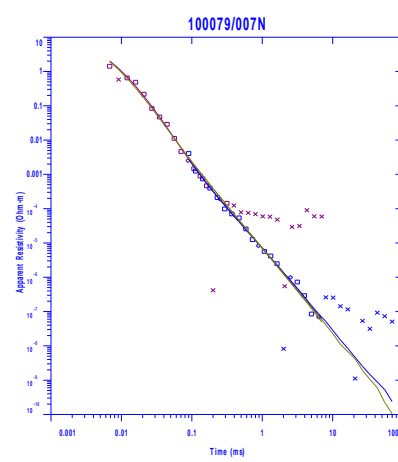
LAYER RESISTIVITY THICKNESS DEPTH ELEV

LAYER	RESISTIVITY	THICKNESS	DEPTH	ELEV
1	3.3	1.8	1.8	0.2
2	16.1	10.2	12.1	-10.1
3	1.5	8.8	20.9	-18.9
4	6.7	13.5	34.3	-32.3
5	21.2			



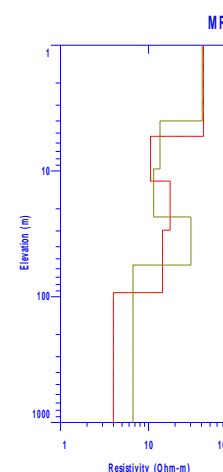
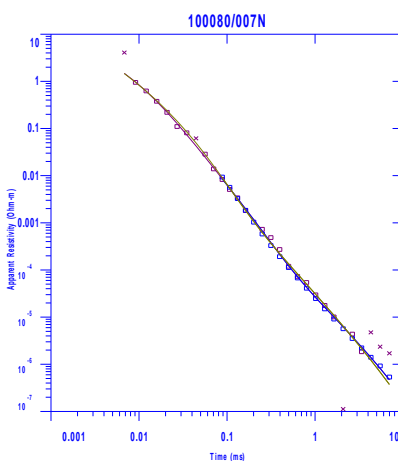
DATASET: SND078XX/007N
 NORTH: 8883538 EAST: 611550.3 ELEV: 2.50

LAYER	RESISTIVITY	THICKNESS	DEPTH	ELEV
1	3.3	2.2	2.2	0.3
2	23.1	10.6	12.7	-10.2
3	0.7	5.0	17.7	-15.2
4	38.9	20.1	37.8	-35.3
5	17.0			



DATASET: SND079/007N
 NORTH: 8883792 EAST: 611683 ELEV: 10.00

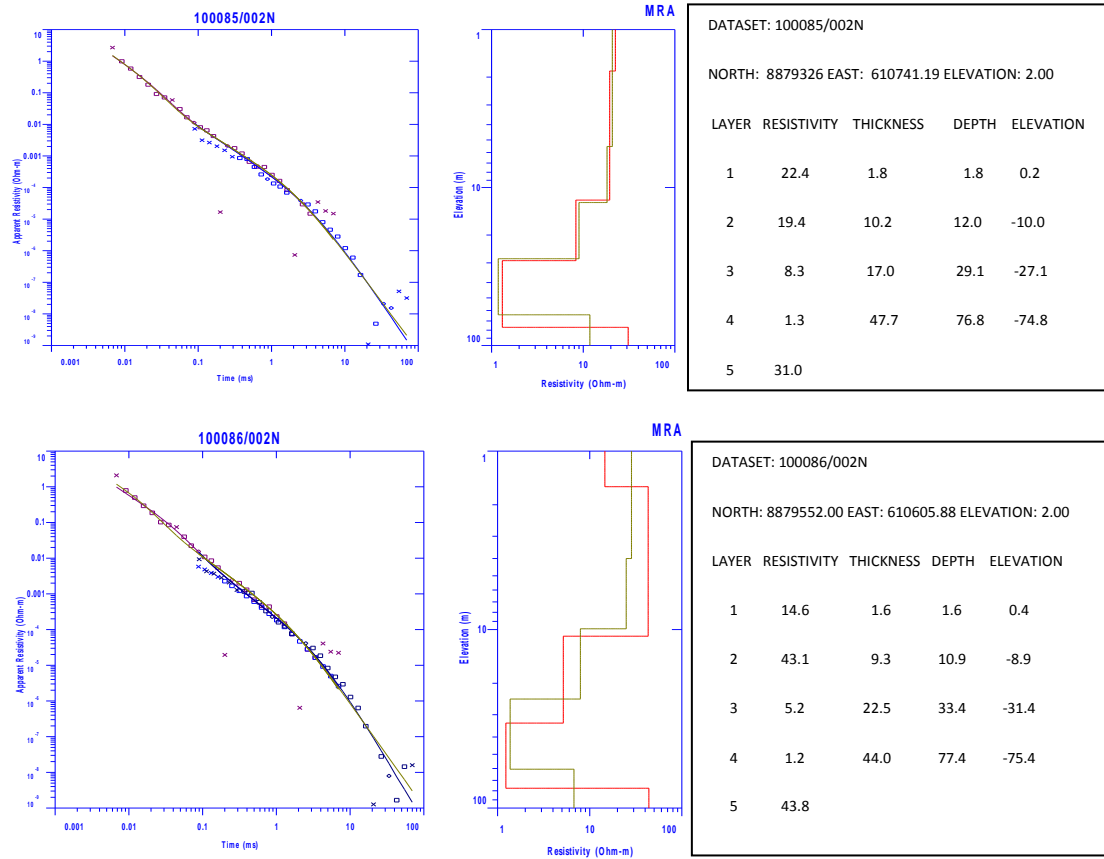
LAYER	RESISTIVITY	THICKNESS	DEPTH	ELEV
1	31.6	2.9	2.9	7.1
2	10.9	4.9	7.8	2.2
3	32.5	9.2	17.0	-7.0
4	137.9	39.4	56.4	-46.4
5	27.5			



DATASET: SND080/007N
 NORTH: 8883972 EAST: 611633.3 ELEV: 25.00

LAYER	RESISTIVITY	THICKNESS	DEPTH	ELEV
1	42.0	5.3	5.3	19.7
2	10.5	6.7	12.1	12.9
3	17.6	17.6	29.6	-4.6
4	14.4	63.2	92.8	-67.8
5	4.0			

6.8 Random soundings



Appendix 2

6.9 Master file

No	Sounding	Easting	Northing	Elev. (m)	AQF res.Ωm	AQF Thk	depth to AQF	MZ Res. Ωm	MZ Thk.	depth to MZ	Saltwater res. Ωm	depth to SI	Elev to ACQ	Elev to MZ	Elev to SI	Thk Vadose	Vadose res Ωm	BU Depth	BU Res Ωm
1	SND001/001N	610749	8878397	2.5	48.1	7.7	2.1	6.2	20	9.9	0.9	29.8	0.4	-7.4	-27.3	2.1	130.7	*	*
2	SND002/001N	610586.7	8878627	2.5	40.7	6.8	2.5	11	24.4	9.3	1.3	3.7	0	-6.8	-1.2	2.5	51.6	*	*
3	SND003/001N	610509.1	8878729	2.5	20.7	7.3	2.4	10.5	25.2	9.7	1	34.9	0.1	-7.2	-32.4	2.4	50.4	*	*
4	SND004/001N	610385.4	8878931	2.5	50.8	7.8	2.4	21.1	24.3	10.2	1.3	34.5	0.1	-7.7	-32	2.4	31.6	*	*
5	SND005/001N	610297.4	8879128	2	24.7	4.2	1.7	11.3	15.5	5.8	0.7	21.3	0.3	-3.8	-19.3	1.7	4.6	*	*
6	SND006/001N	610170.3	8879376	2	28.3	7.5	2.1	8.7	25.7	7.5	1.3	35.3	-0.1	-5.5	-33.3	2.1	52.1	*	*
7	SND007/001N	610066.3	8879623	2	30.8	8.2	2.3	10.6	30.4	10.5	1.6	40.8	-0.3	-8.5	-38.8	2.3	46.6	*	*
8	SND008/001N	609996.6	8879831	2.5	27.7	6.5	2.8	11.1	16.6	9.3	1.5	25.9	-0.3	-6.8	-23.4	2.8	15.8	*	*
9	SND009/001N	609829.2	8879955	2	34.3	6.1	1.8	11	16.9	7.9	1	24.8	0.2	-5.9	-22.8	1.8	62.1	*	*
10	SND010/001N	609422.7	8880399	1.5	64.3	5.3	1.5	10	15.1	6.8	0.8	21.9	0	-5.3	-20.4	1.5	79.2	*	*
11	SND011/001N	609443	8880552	1.5	72.3	5.7	1	8.9	13.5	6.7	0.9	20.2	0.5	-5.2	-18.7	1	87.7	*	*
12	SND012/002N	609853.4	8880911	1	40.4	2.9	0.8	6.5	14.2	3.7	1.2	17.9	0.2	-2.7	-16.9	0.8	98	*	*
13	SND013/002N	610026.4	8880772	1.5	29.3	4.7	1.2	11.7	14.3	5.8	0.9	20.2	0.3	-4.3	-18.7	1.2	12.9	*	*
14	SND014/002N	610101.5	8880558	1	20.1	5.3	0.8	7.8	12.8	6.1	0.4	18.9	0.2	-5.1	-17.9	0.8	1.2	*	*
15	SND015/002N	610304	8880369	1.5	35.9	7.8	1.4	11.6	24.1	9.2	1	33.3	0.1	-7.7	-31.8	1.4	74.3	*	*
16	SND016/002N	610426.1	8880073	2	45.7	7.4	1.7	11.5	25.6	9.1	1.1	34.7	0.3	-7.1	-32.7	1.7	9.1	*	*
17	SND017/002N	610537.5	8879891	2	66.5	8.9	1.7	13.2	26.3	10.6	1.5	36.8	0.3	-8.6	-34.8	1.7	8	*	*
18	SND018/002N	610602	8879737	2	18.7	8.6	1.9	13.3	18.3	10.5	1.4	39.9	0.1	-8.5	-37.9	1.9	24.6	*	*
19	SND019/002N	610698.5	8879547	2	58	9.9	1.9	7.2	24.9	11.8	1.5	36.7	0.1	-9.8	-34.7	1.9	5.9	*	*
20	SND020/002N	610843.2	8879322	3.5	48.5	10.1	3.5	10.1	27.7	13.6	1.2	41.3	0	-10.1	-37.8	3.5	17	*	*
21	SND021/002N	610969.9	8879191	3	32.3	9.8	3	9.8	30.4	13.7	1.4	44	0	-10.7	-41	3	11.5	*	*
22	SND022/002N	611033	8879073	3.5	56.4	11.3	3.2	11.5	25	14.5	1.3	39.5	0.3	-11	-36	3.2	11	*	*

23	SND023/002N	611126	8878844	2.5	53	6	2.4	12.8	20.3	8.5	0.7	28.7	0.1	-6	-26.2	2.4	365.4	*	*
24	SND024/003N	611521.2	8879373	1.5	*	*	*	16.4	15.2	1.6	1.4	15.2	*	-0.1	-13.7	1.6	60.9	*	*
25	SND025/003N	611424	8879506	5	82.1	12.2	4.9	7.8	28	17.1	0.6	45	0.1	-12.1	-40	4.9	355.6	*	*
26	SND026/003N	611333.6	8879658	2.5	27.4	12.5	2.4	9.3	34	14.8	1.4	48.9	0.1	-12.3	-46.4	2.4	59.9	*	*
27	SND028/003N	611126	8880010	2.5	50	10.8	2.2	15.5	30.6	13	1.5	43.6	0.3	-10.5	-41.1	2.2	6.7	*	*
28	SND029/003N	611003	8880286	2.5	48.1	12.4	2.2	17.6	18.6	14.6	1.3	33.2	0.3	-12.1	-30.7	2.2	16.4	*	*
29	SND030/003N	610741	8880596	2	49.5	9.3	1.9	6.8	23.3	11.2	0.8	34.5	0.1	-9.2	-32.5	1.9	8.9	*	*
30	SND031/003N	610746	8880840	1.5	34.5	4.1	1.4	7.5	15.8	5.4	1.2	21.3	0.1	-3.9	-19.8	1.4	175	*	*
31	SND032/003N	610541	8880895	1.5	41.3	2.8	1.1	10.6	18.8	3.9	0.8	22.7	0.4	-2.4	-21.2	1.1	18	*	*
32	SND033/003N	610453	8881103	1.5	*	*	*	7.2	19.6	1.5	0.8	21.1	*	0	-19.6	1.5	39.2	*	*
33	SND035/004N	611738.8	8879765	3	43.4	13.2	3	13.7	28.4	16.2	1.8	44.6	0	-13.2	-41.6	3	12.7	*	*
34	SND036/004N	611708.6	8879983	2.5	43.7	12	2.2	15.1	24.4	14.2	2.6	38.6	0.3	-11.7	-36.1	2.2	103	*	*
35	SND037/004N	611589	8880156	2	48.5	10.4	1.6	10.3	35.7	12.1	0.6	47.8	0.4	-10.1	-45.8	1.6	24.6	*	*
36	SND038/004N	611501.9	8880295	2	39.4	11.1	1.7	14.5	36.8	12.8	2.1	49.6	0.3	-10.8	-47.6	1.7	4.3	*	*
37	SND039/004N	611394.8	8880519	2	54.8	12.8	2	15.2	25.5	14.9	1.9	40.4	0	-12.9	-38.4	2	122.6	*	*
38	SND040/004N	611286.1	8880702	2	58.1	12.4	1.9	11.7	19.3	14.4	1.2	33.7	0.1	-12.4	-31.7	1.9	258.4	*	*
39	SND041/004N	611207.4	8880959	2.5	69	12.7	2.4	11.8	18.7	15.1	0.8	33.8	0.1	-12.6	-31.3	2.4	8	*	*
40	SND042/004N	611107.1	8881094	2.5	39.4	4.1	2.5	8.3	11.1	6.7	1	17.8	0	-4.2	-15.3	2.5	91.8	*	*
41	SND043/004N	610898.6	8881250	1.5	32	6.4	1.6	9.6	15.9	7.9	0.5	23.8	-0.1	-6.4	-22.3	1.6	10.3	*	*
42	SND044/004N	610853.7	8881458	2	45.3	3.1	1.4	12	10.1	4.5	0.9	14.6	0.6	-2.5	-12.6	1.4	76.1	*	*
43	SND045/004N	610722.2	8881575	1.5	*	*	*	13.6	8.8	1.4	1.2	10.3	*	0.1	-8.8	1.4	66	*	*
44	SND046/005N	612151.1	8879891	7	46.1	7.6	6.6	12.9	28.7	13.6	2	42.4	0.4	-6.6	-35.4	6.6	386	*	*
45	SND047/005N	612367.3	8879936	6	34	13.8	5.6	5.6	14.5	19.4	1.5	33.9	0.4	-13.4	-27.9	5.6	452	*	*
46	SND048/005N	612121.9	8880229	3	32.5	9.4	2.7	16.9	36.6	12	2.4	48.6	0.3	-9	-45.6	2.7	69.1	*	*
47	SND049/005N	611905.9	8880526	2.5	50.5	12.4	2.5	9.6	27	14.9	2.7	41.8	0	-12.4	-39.3	2.5	11	*	*
48	SND050/005N	611850.6	8880644	2.5	55.2	15.8	2.3	12.8	21.9	18.1	2	39.9	0.2	-15.6	-37.4	2.3	22.4	*	*
49	SND051/005N	611750.4	8880826	2.5	58	11.9	2.5	13.7	23.4	14.3	1.6	37.9	0	-11.8	-35.4	2.5	20.1	*	*
50	SND052/005N	611674	8880987	2.5	58.3	10.8	2.5	15.9	24.6	13.3	1.3	37.9	0	-10.8	-35.4	2.5	8.9	*	*
51	SND053/005N	611574.8	8881157	2	59.1	15.5	2.1	10.2	16.1	17.7	1.2	33.8	-0.1	-15.7	-31.8	2.1	16.5	*	*

52	SND054/005N	611500	8881336	2	53.2	4.8	2	8.8	10.6	6.8	1.7	17.4	0	-4.8	-15.4	2	7	*	*
53	SND055/005N	611401	8881571	1.5	32.7	3	1.5	11.3	8.4	4.5	1.3	12.9	0	-3	-11.4	1.5	10.8	*	*
54	SND056/005N	611225.4	8881767	1.5	32.8	4.9	1.5	4.5	9	6.4	1	15.7	0	-4.9	-14.2	1.5	61.5	*	*
55	SND057/006N	612736.8	8880348	3	*	*	*	18.3	12.6	7.5	1.2	20.2	*	-4.5	-17.2	2.7	35.1	*	*
56	SND058/006N	612633.8	8880532	3	55.2	6.9	2.4	9.7	20.5	9.3	1.3	29.8	0.6	-6.3	-26.8	2.4	107.4	*	*
57	SND059/005N	612528.3	8880748	2.5	48.7	10.2	2.1	11.7	20	12.3	1.7	32.4	0.4	-9.8	-29.9	2.1	14.7	*	*
58	SND060/006N	612435.1	8880917	2	43.9	12.8	1.8	12.6	18.2	14.6	1.6	32.7	0.2	-12.6	-30.7	1.8	14.5	*	*
59	SND061/006N	612329.4	8881127	2	26.8	12.2	1.6	13.8	16.7	13.9	1.5	30.5	0.4	-11.9	-28.5	1.6	12.2	*	*
60	SND062/006N	612250.6	8881246	2	25.6	10.7	1.9	12.9	18	12.6	1.2	34	0.1	-10.6	-32	1.9	17.1	*	*
61	SND063/006N	612147	8881468	2.5	55.7	12.5	2.3	16.5	27.6	14.8	2.4	42.4	0.2	-12.3	-39.9	2.3	133.4	*	*
62	SND064/006N	612034.5	8881664	1.5	*	*	*	14.5	16	1.5	1.3	17.5	*	0	-16	1.5	72.9	*	*
63	SND065/006N	611769.8	8881843	1	*	*	*	6.1	10	0.9	1.1	10.9	*	0.1	-9.9	0.9	21.8	*	*
64	SND066/006N	611527.1	8882399	1.5	*	*	*	6.3	22.8	1.4	0.5	24.2	*	0.1	-22.7	1.4	38.5	*	*
65	SND067/006N	611453.6	8882587	1.5	*	*	*	5.3	7.3	1.4	0.4	8.7	*	0.1	-7.2	1.4	24.3	*	*
66	SND068/007N	613381.4	8880574	1.5	21	4.6	1.1	3.3	10.8	6	1.1	16.8	0.4	-4.5	-15.3	1.4	8.4	*	*
67	SND069/007N	613235.2	8880779	2	35.4	9.2	1.9	3	13.9	11.1	1	25	0.1	-9.1	-23	1.9	75.5	70.3	73.3
68	SND070/007N	613109.6	8880973	1.5	23.9	10.8	1.5	3.9	15.2	12.3	1	27.5	0	-10.8	-26	1.5	5.5	79.5	87.9
69	SND071/007N	613002.3	8881161	1.5	24.7	9.5	1.5	3.2	13.6	11	1.1	24.6	0	-9.5	-23.1	1.5	38.6	78.5	19.7
70	SND072/007N	612893.9	8881356	1.5	25.3	9.4	1.1	3.6	19.4	10.6	0.8	30.1	0.4	-9.1	-28.6	1.1	4.1	67.4	75.8
71	SND074/007N	612665.6	8881683	1.5	39.1	6.3	1.6	4.2	8.7	7.8	1	16.6	-0.1	-6.3	-15.1	1.6	5.5	64	14.5
72	SND075/007N	612614	8881917	1.5	*	*	*	11.5	9.1	1.5	1.1	10.5	*	0	-9	1.5	47.1	74.9	125.9
73	SND076/007N	612449.8	8882216	1.5	*	*	*	3.8	6.5	1.4	0.9	8	*	0.1	-6.5	1.4	8	59.7	131
74	SND077/007N	611883	8883379	1.5	*	*	*	6.7	8.4	1.1	1.2	9.5	*	0.4	-8	1.1	2.9	42.7	289
75	SND078/007N	611750.3	8883538	2	*	*	*	16.1	10.2	1.8	1.5	12.1	*	0.2	-10.1	1.8	3.3	34.3	21.2

Note: Elev. => elevation; AQF => Freshwater aquifer; res => Resistivity; Thk => Thickness; MZ => Mixing zone; SI => Saltwater Intrusion; BU => Basement unit